

Hierarchical Modeling of Solid Oxide Cells: From micro-kinetics to 3-D stacks

Zur Erlangung des akademischen Grades

Doktor der Ingenieurwissenschaften

der Fakultät für Chemieingenieurwesen und Verfahrenstechnik

Karlsruher Institut für Technologie (KIT)

genehmigte

Dissertation

von

Aayan Banerjee, M.S.

geb. in Kolkata, Indien

Tag der mündlichen Prüfung: 05.10.2018

Hauptreferent: Prof. Dr. rer. nat. habil. Olaf Deutschmann

Korreferent: Prof. Dr.-Ing. habil. Roland Dittmeyer

Acknowledgements

This work would not have been possible without my advisor, Prof. Olaf Deutschmann. I would like to express my humblest gratitude to you for not only giving me the opportunity but perhaps more importantly, the freedom and at times unconditional support to pursue my research goals. It is safe to say that during these three and a half years under your aegis, I have truly found my love and passion for science.

My sincere thanks to my co-advisor, Prof. Roland Dittmeyer. Thank you for all the thought-provoking conversation about science and research. I have always left our meetings with my interest piqued and my brain stimulated.

Next in line are Drs. Steffen Tischer and Julian Dailly. Steffen and Julian, thank you for always being available to talk about work, science and literally anything else under the sun. These past years in the office would have been a lot duller without our in-depth discussions about life, the universe and everything.

I would like to thank all my friends and family for the love, support and comradery. I would especially like to thank all the friends I have made during my stay in Germany. Henning and Siva, thank you for the companionship and the enjoyable lunches. Marion, thank you for taking me to my first “Das Fest” and for just being cool. Andreas, thank you for all the entertaining conversations about football. Thank you, Felix, for being a chilled-out office mate. Ursula and Yvonne, thank you for always being patient (especially with my German) and for simply being kind. Thank you, Yuqing, for all the proof-reading and the bug fixes and for being so dedicated. Marie, Jean-Baptiste, Daniel, Justus, Jiyoung, Karla, Michael, Alvaro and Alex, thank you for always listening to me whine and complain with a laugh. Frank, thank you for all the wonderful evenings spent playing board games, and Dungeons and Dragons. And finally, thank you, Claudia, for just being there.

The financial support from the Helmholtz Research School – Energy Related Catalysis is also gratefully acknowledged.

Abstract

The development of a multi-physics continuum model to investigate the operation of solid oxide cells converting chemical to electrical energy and vice-versa has been detailed in this study. Solid oxide cells are complex devices involving a myriad of physical and chemical phenomena on multiple scales: from single particles to stacks of multiple cells. Consequently, to identify the bottleneck in performance and lifetime, a multi-scale hierarchical approach is necessary to couple detailed reaction chemistry at the nanometer scale with bulk transport at the micrometer scale for a single cell and millimeter-meter scale for a cell stack. The model establishes a consistent mathematical framework to describe the physics over all these scales by solving the governing equations of mass, momentum, charge and energy conservation and treating heterogeneous reactions on the electrode surface and electrochemical reactions at the electronic-ionic phase interfaces as volumetric source terms. The various features of the model are demonstrated using two examples. First, the production of syngas (H_2+CO) via co-electrolysis of H_2O and CO_2 in a solid oxide button cell, single repeating unit and cell stack is investigated to unravel the repercussion of scaling up on performance, capital cost and lifetime. To obtain realistic reaction kinetic fit parameters, the model reproduced polarization, temperature and outlet gas composition measurements made by Fu et al. on single Ni-GDC|YSZ|LSM-YSZ cells [*ECS Transactions* **35**, 2949-2956 (2011)]. Subsequently, the calibrated model was used to generate 3-D contour plots to map the performance of a single repeating unit of a F-design stack from Forschungszentrum Jülich [*Fuel Cells* **7**, 204-210 (2007)] producing two distinct output $\text{H}_2:\text{CO}$ ratios suitable for Fischer-Tropsch synthesis and hydroformylation. A parametric analysis revealed optimal operating regimes for the repeating unit and underscored the importance of residence time, operating voltage and temperature on efficiency and syngas yield. When scaled up from cells to commercial-scale stacks, running at highest efficiency minimized temperature gradients across the stack but the low current densities led to higher capital costs and larger electrolyzer areas required to produce commercial quantities of syngas. Simulating stack operation over a series of operating regimes also revealed the stack transients to be governed by heat transport in lieu of the faster mass and charge transport. Having established the analytical and optimization capabilities of the model, the second example served to enhance the universality of the

model by obtaining kinetic parameters intrinsic to a material and independent of electrode microstructure. To that end, the model simulated a solid oxide half-cell comprising of a porous LSM-YSZ composite air electrode sintered to a dense YSZ electrolyte to investigate the oxygen reduction/evolution reaction and thereby acquire kinetics intrinsic to the LSM-YSZ composite. The electrochemical reduction of O₂ was modeled using three candidate elementary kinetic mechanisms. Each mechanism included parallel surface and bulk pathways for O₂ reduction and were driven by three different electric phase potentials. The mechanisms were compared against three sets of electrochemical impedance spectra and polarization curves measured by Barbucci et al. [*J. Appl. Electrochem*, **39**, 513–521 (2009)], Cronin et al. [*J. Electrochem. Soc.*, **159**(4), B385–B393 (2012)] and Nielsen and Hjelm [*Electrochimica Acta*, **115**, 31–45 (2014)] over a wide range of operating temperatures (873 K to 1173 K), inlet O₂ concentrations (5% to 100%) and overpotentials (-1V to +1V). Two of the three mechanisms could quantitatively reproduce the three sets of experiments without reparametrizing the kinetics. Yet on analyzing their kinetic and thermodynamic parameters, the mechanism postulating the chemisorption of gas-phase O₂ on LSM to form the superoxo-like adsorbate O₂⁻ was determined to be the most realistic. These two examples help highlight a modeling tool suitable for solid oxide cell and stack design, monitoring and control.

Zusammenfassung

In dieser Arbeit wurde ein physikalisches Mehrskalen-Kontinuum-Modell zur Untersuchung von Feststoffoxidzellen (*Solide Oxide Cells*, SOCs), welche chemische in elektrische Energie oder umgekehrt umwandeln können, entwickelt und detailliert untersucht. Zur Beschreibung von Feststoffoxidzellen sind eine Vielzahl unterschiedlicher chemischer und physikalischer Prozesse in verschiedenen Größenordnungen zu berücksichtigen: von einzelnen Partikeln bis zur Kombination von mehreren Zellen zu sog. *Stacks* („Stapel“). Um die Leistungs- und Lebensdauerbeschränkungen solcher Zellen aufzudecken, wird eine hierarchische Multiskalen-Herangehensweise benötigt, die die chemischen Reaktionen im Nanometer-Bereich, die Transportphänomene im Mikrometer-Bereich für eine einzelne Zelle bzw. im Millimeter-bis-Meter-Bereich für einen *Stack* koppelt. Das angewandte Modell bildet einen konsistenten mathematischen Rahmen, um die physikalischen Prozesse in all diesen Größenordnungen zu beschreiben. Dabei werden die fundamentalen Gleichungen für den Massen-, Impuls-, Ladungs- und Energieerhalt gelöst, wobei die heterogenen Reaktionen auf der Elektrodenoberfläche und die elektrochemischen Reaktionen in den elektronisch-ionischen Grenzflächen als volumetrische Quellenterme behandelt werden. Die Eigenschaften des Modells werden an zwei Beispielen demonstriert. Zuerst wird die Produktion von Wassergas ($H_2 + CO$) via Co-Elektrolyse von H_2O und CO_2 in einer Feststoffoxid-Knopfzelle, einer einzelnen *Repeating Unit* („Wiederholungseinheit“) und einem Stack untersucht, um die Auswirkungen der Hochskalierung auf Leistung, Kapitalkosten und Lebensdauer aufzudecken. Um realistische kinetische Parameter zu erhalten, wurde das Modell an Messdaten für die Polarisierung, die Temperatur und die Gaszusammensetzung am Ausgang angepasst, welche von Fu et al. in einer Einzel- Ni-GDC|YSZ|LSM-YSZ-Zelle gemessen wurden [*ECS Transactions* **35**, 2949-2956 (2011)]. Außerdem wurde das so kalibrierte Modell verwendet, um 3D-Kontour-Plots zu erstellen, welche die Leistung einer einzelnen Zelle eines F-Design-Stacks des Forschungszentrums Jülich [*Fuel Cells* **7**, 204-210 (2007)] abbilden. Dabei wurden am Ausgang zwei verschiedene H_2/CO -Verhältnisse gewählt, welche kommerziell für die Hydroformylierung und die Fischer-Tropsch-Synthese zum Einsatz kommen. Eine parametrische Analyse zeigte die optimalen Betriebsbedingungen für eine *Repeating Unit* auf, wodurch die Bedeutung von Aufenthaltsdauer, Spannung und

Temperatur für die Effizienz und die Wassergas-Ausbeute unterstreichen wird. Im Falle einer Hochskalierung von einzelnen Zellen zu kommerziell eingesetzten *Stacks* führte der Betrieb bei höchster Effizienz zu den geringsten Temperaturgradienten innerhalb des Gerätes. Jedoch die geringen Stromdichten führten zu höheren Kapitalkosten und größeren Elektrolytator-Flächen für eine industrielle Wassergas-Produktion. Die Simulation eines *Stacks* für verschiedene Betriebspunkte zeigte auf, dass der *Stack* im Bereich des schnellen Massen- und Ladungstransports vom Wärmetransport limitiert wird. Nachdem die analytischen und die Optimierungsmöglichkeiten eruiert wurden, dient das zweite Beispiel dazu, die Universalität des Modells zu verbessern. Dafür wurden kinetische Parameter bestimmt, welche intrinsisch für ein Material und damit unabhängig von der Mikrostruktur der Elektrode sind. Zuletzt wurde das Modell für eine Simulation einer Feststoffoxid-Halbzelle genutzt, welche aus einer porösen LSM-YSZ-(Sauerstoff)-Elektrode, die auf einen dichten YSZ-Elektrolyten gesintert wurde, besteht. Dabei wurde die Kinetik der Sauerstoffreduktionsreaktion untersucht, wobei eine intrinsische Kinetik für die YSM-LSZ-Elektrode erhalten wurde. Für die Modellierung der elektrochemischen Reduktion von O_2 wurden drei verschiedene Mechanismen verwendet. Jeder Mechanismus beinhaltet hierbei den parallelen Transport von Sauerstoff-Spezies über die Partikeloberfläche und durch das Teilchen hindurch, wobei drei verschiedene elektrische Potentiale die Reduktion antrieben. Die Mechanismen wurden mit drei Sets von elektrochemischen Impedanz-Spektren und Polarisationskurven verglichen, welche von Barbucci et al. [*J. Appl. Electrochem*, **39**, 513–521 (2009)], Cronin et al. [*J. Electrochem. Soc.*, **159**(4), B385–B393 (2012)] und Nielsen und Hjelm [*Electrochimica Acta*, **115**, 31–45 (2014)] über einen weiten Bereich von Betriebstemperaturen (873 K bis 1173 K), Einlass- O_2 -Konzentrationen (5% bis 100%) und Überpotentialen (-1 V bis +1 V) aufgenommen wurden. Zwei der drei Mechanismen konnten quantitativ diese drei experimentellen Sets ohne neue Parametrisierung der Kinetik wiedergeben. Durch Analyse der thermodynamischen Parameter und der Kinetik konnte jener Mechanismus, der die Chemisorption eines gasförmigen O_2 -Moleküls unter Bildung einer Super-Oxo- O_2^- -Spezies auf der LSM-Oberfläche postuliert, als der am besten der Realität entsprechende identifiziert werden. Diese zwei Beispiele heben somit hervor, dass diese Modellierung für SOC- bzw. Stack-Design, -Überwachung und -Steuerung ein geeignetes Werkzeug darstellt.

Contents

Acknowledgements.....	i
Abstract.....	ii
Zusammenfassung.....	iv
Nomenclature.....	viii
Chapter 1 Introduction.....	1
1.1 Co-electrolysis of CO ₂ and H ₂ O.....	3
1.2 Oxygen reduction/evolution reaction.....	5
1.3 Objectives of the present work.....	7
Chapter 2 Modeling Methodology.....	9
2.1 Mass and Momentum Conservation.....	13
2.1.1 Bulk gas phase.....	13
2.1.2 Porous media.....	14
2.1.3 Boundary Conditions.....	17
2.2 Charge Conservation.....	17
2.2.1 Distributed Charge Transfer.....	17
2.2.2 Boundary Conditions.....	18
2.2.3 Interfacial Charge Transfer.....	19
2.3 Energy Conservation.....	22
2.3.1 Bulk gas phase.....	22
2.3.2 Solid phase of a single Planar Repeating Unit.....	23
2.3.3 Solid phase of a stack of Planar Repeating Units.....	26
2.3.4 Boundary Conditions.....	26
2.4 Effective Transport Properties.....	27
Chapter 3 High Temperature Co-electrolysis – From Cells to Stacks.....	30
3.1 Additional model details.....	31
3.1.1 Electrochemistry.....	31
3.1.2 Heterogeneous chemistry.....	33
3.1.3 Performance Metrics.....	34
3.2 Computational Procedure.....	35
3.3 Results and Discussion.....	37
3.3.1 Comparison of model and experiment.....	37
3.3.2 Performance analysis of F-design RU.....	43
3.3.3 Performance analysis of F-design stacks.....	51

3.3.4	Transient operation of F-design stacks	55
Chapter 4	Elementary Kinetics of the Oxygen Reduction/Evolution Reaction on LSM-YSZ Composite Electrodes	58
4.1	Micro-kinetic modeling of electrochemistry	58
4.1.1	ORR mechanisms.....	59
4.1.2	ORR kinetics	62
4.1.3	ORR thermodynamics.....	68
4.2	Computational Procedure.....	69
4.3	Results and Discussion	70
4.3.1	Comparison of mechanisms against experimental data	70
4.3.2	Sensitivity Analysis	78
Chapter 5	Summary and Outlook	87
Appendix	92
References	94

Nomenclature

Latin

a_C	carbon activity factor
A	specific area [m^{-1}] or pre-exponential factor for reaction rate constant
B	permeability [m^2]
c	volumetric concentration [mol m^{-3}] or surface concentration [mol m^{-2}]
C	capacitance per unit area [F m^{-2}]
C_p	specific heat capacity at constant pressure [$\text{J kg}^{-1} \text{K}^{-1}$]
d	diameter [m]
D	diffusion coefficient [$\text{m}^2 \text{s}^{-1}$]
D^*	tracer self-diffusion coefficient [$\text{m}^2 \text{s}^{-1}$]
$D^{*,0}$	tracer self-diffusion coefficient in pure oxygen [$\text{m}^2 \text{s}^{-1}$]
E	lumped electric potential difference [V]
E_a	Activation energy
E_{CO_2}	Activation energy for CO_2 electrochemical reduction [J mol^{-1}]
$E_{\text{H}_2\text{O}}$	Activation energy for H_2O electrochemical reduction [J mol^{-1}]
E_{O_2}	Activation energy for O_2 electrochemical reduction [J mol^{-1}]
F	Faraday constant [C mol^{-1}]
$F_{\text{ede} \rightarrow \text{ic}}$	view factor for thermal radiation from electrode to interconnect
G^0	standard molar Gibbs free energy [J mol^{-1}]
G_z	Graetz number
h	elements of matrix H
h_{conv}	heat transfer coefficient due to convection [$\text{W m}^{-2} \text{K}^{-1}$]
h_{surr}	heat transfer coefficient of the surroundings due to convection [$\text{W m}^{-2} \text{K}^{-1}$]
H	matrix to evaluate diffusion coefficients used in Dusty Gas Model or molar enthalpy [J mol^{-1}]
i	current density [A m^{-2}]
J	molar flux [$\text{mol m}^{-2} \text{s}^{-1}$]
k_b	backward reaction rate constant
k_f	forward reaction rate constant

K	total number of species
l	lattice constant
L	length [m]
\dot{m}	mass flow rate per unit area [$\text{kg m}^{-2} \text{s}^{-1}$]
\dot{m}_{syn}	total syngas produced by a single planar cell in a day [kg day^{-1}]
n_e	number of electrons
Nu	Nusselt number
O_{O}^{\times}	lattice oxygen
p	pressure [Pa]
Pr	Prandtl number
\dot{Q}	heat flux [W m^{-2}]
\dot{Q}_i	net heat flux due to current [W m^{-2}]
r	reaction rate [$\text{mol m}^{-2} \text{s}^{-1}$]
R	universal gas constant [$\text{J mol}^{-1} \text{K}^{-1}$]
R_b	backward reaction
R_{contact}	contact resistance [Ωm^2]
R_f	forward reaction
R_p	polarization resistance [Ωm^2]
R_{rad}	thermal resistance to radiation [m^{-2}]
Re	Reynolds number
S	molar entropy [$\text{J mol}^{-1} \text{K}^{-1}$]
\dot{s}_k	production rate of species k due to reactions [$\text{mol m}^{-2} \text{s}^{-1}$]
Sc	Schmidt number
t	time [s] or thickness [m]
T	temperature [K]
T_{surr}	temperature of the surroundings [K]
u	velocity [m s^{-1}]
V_m	molar volume of lattice
$V_{\text{O}}^{\ddot{\cdot}}$	lattice oxygen vacancy
vol	volume per unit length [m^2]
w	width [m]
w_{fac}	weighting factor

W	molecular weight [kg mol^{-1}]
X	species mole fraction
y	spatial coordinate [m]
Y	species mass fraction
z	spatial coordinate [m]
\square	vacant site

Greek

β	charge transfer coefficient
γ	percolation probability
γ_{syn}	syngas yield
Γ	density of available active sites [mol m^{-2}]
δ	Kronecker delta
δ_s	mean distance for surface diffusion
Δ	difference of quantities
ϵ	porosity
ϵ_{rad}	thermal radiation emissivity
ζ	number of adsorption sites
η	overpotential [V] or thermal efficiency
θ	surface coverage
κ	temperature coefficient for pre-exponential factor
λ	thermal conductivity [$\text{W m}^{-1} \text{K}^{-1}$]
μ	viscosity [$\text{kg m}^{-1} \text{s}^{-1}$]
ν	stoichiometric coefficient or vibrational frequency
ν_f	volume fraction
ξ	surface coverage coefficient for activation energy
ρ	density [kg m^{-3}]
σ	charge conductivity [S m^{-2}]
σ_{SB}	Stefan-Boltzmann constant [$\text{W m}^{-2} \text{K}^{-4}$]
τ_{const}	time constant [s]
τ_{fac}	tortuosity factor
ϕ	local phase potential [V]

∇ gradient of vector

Subscripts

2PB	two-phase boundary
3PB	three-phase boundary
a	anodic
ae	air electrode
ae/elyt	interface between the air electrode and the electrolyte
act	activation
b	bulk phase of a material
c	cathodic
ch	channel
cell	cell
CO ₂	CO ₂ reaction pathway
CT	charge transfer
diff	diffusion
DL	electric double layer at the interface between electronic and ionic phases
el	electronic phase
el/io	interface between electronic and ionic phases
ede	electrode
elyt	electrolyte
echem	electrochemical reactions
fe	fuel electrode
fe/elyt	interface between the fuel electrode and the electrolyte
g	gas phase
gas/ede	interface between the gas phase and the electrode surface
hchem	heterogeneous surface reactions
<i>i</i>	reaction index or inlet
ic	interconnect
io	ionic phase
h	hydraulic
H ₂ O	H ₂ O reaction pathway

<i>j</i>	species index
<i>k</i>	species index
Kn	Knudsen
<i>l</i>	species index
<i>m</i>	electric phase index
o	outlet
ohm	ohmic
p	particle
pore	pore
plate	interconnect plate
<i>q</i>	stack component index
r	reaction
RU	repeating unit
rad	radiation
rev	reversible
rib	interconnect rib
s	solid phase or surface

Superscripts

DGM	pertaining to the Dusty Gas Model
e	effective property
el	electronic phase
eq	equilibrium
io	ionic phase
V	volumetric quantity
'	pertaining to reactants
"	pertaining to products

Chapter 1

Introduction

Solid Oxide Cells (SOC) offer an efficient, decentralized and clean alternative to conventional power and chemical generation processes. SOCs are the high temperature counterparts of the more well-known low temperature polymer electrolyte membrane (PEM) cells and are theoretically more energy and power dense than both PEM cells and Li-ion batteries. They can either be run in “fuel cell” mode i.e. Solid Oxide Fuel Cell (SOFC) or in “electrolysis” mode i.e. Solid Oxide Electrolysis Cell (SOEC). In a SOFC, the fuel, typically H_2 , flows over the anode and an oxidant, typically air, flows over the cathode. The two electrodes are separated by a dense O^{2-} ion-conducting electrolyte which is impervious to gas flow. The oxygen in the air consume electrons supplied by the cathode thereby rendering it positive. The O^{2-} ion so created, are conducted across the electrolyte to the anode where they oxidize H_2 to form steam and release electrons thereby rendering the anode negative. The electrons so released are collected by current collectors or interconnects and passed through an external circuit. The exact opposite sequence of events characterizes a SOEC. The electrons supplied by an external source to the now negative cathode reduce an incoming flow of steam into H_2 and O^{2-} . The O^{2-} ions are transmitted through the electrolyte to the positive anode where they oxidize to form O_2 gas and release electrons back to the external circuit. Ergo. the reducing electrode (cathode) and oxidizing electrode (anode) along with their polarity are flipped when going from SOFC to SOEC mode as illustrated in Fig. 1.1. Thus, to avoid confusion, the two electrodes are henceforth referred to in the entire manuscript as the fuel electrode denoting the electrode where H_2 is consumed or produced and the air electrode where O_2 is consumed or produced. As seen in the figure, the fuel electrode is always negative, and the air electrode is always positive.

The underlying transport phenomena taking place in the co-flow planar cell shown in the figure include gas transport in the channels, gas diffusion through the porous electrode microstructures, and electron and ion transport through the interconnected clusters of electron and ion- conducting phases in the electrodes. The various modes of transport are

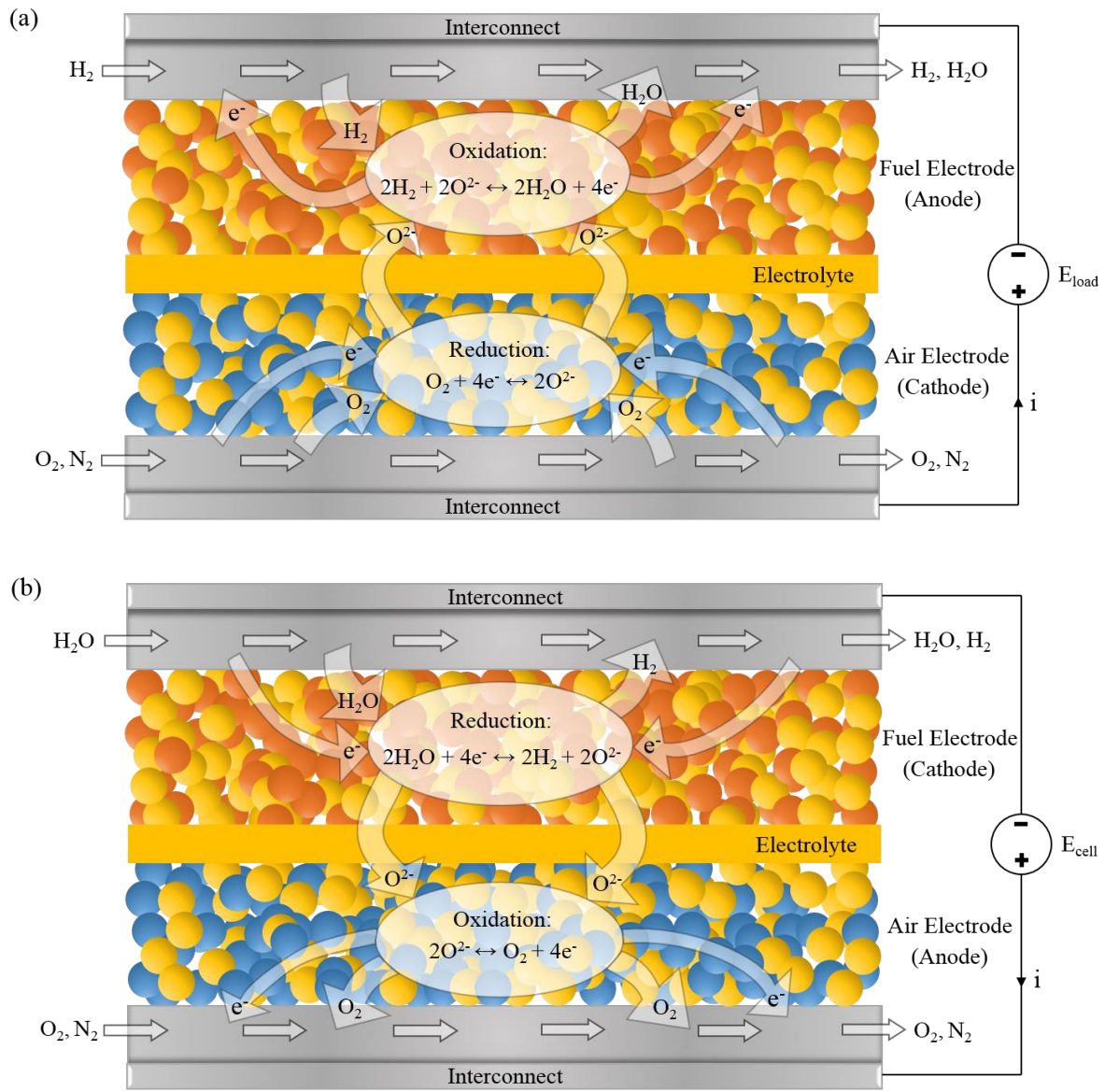


Figure 1.1. A schematic showing the different components and the underlying processes of (a) Solid Oxide Fuel Cell operating on H₂ and air and (b) Solid Oxide Electrolysis Cell operating on steam and air.

subsequently coupled to heterogeneous surface reactions in the fuel electrode, for example in direct internal reforming (DIR) cells running on methane, and electrochemical reactions. These physico-chemical processes form an intricate web with any one of them being responsible for limiting the performance of the cell. Thus, a computational model capable of untangling this intricate web is highly useful as both a tool for analysis and diagnostics as well as a predictive tool for design with a focus on improving the performance, reliability and lifetime of the device.

In the present work, the ongoing efforts of developing such a modeling tool are described. The features, capabilities and pitfalls of the model are illustrated using two very different example studies. The first deals with the modeling of a solid oxide co-electrolysis cell and stack of cells. This example illustrates the hierarchical nature of the modeling approach taken and analyzes the outcomes and ramifications of scaling up from lab-scale button cells to commercial stacks. The second example investigates the O₂ reduction/evolution reaction in a half-cell or symmetrical cell to isolate the effects of the random porous electrode microstructure, and uncover kinetics intrinsic to the material, thereby moving us a step closer to truly universal predictive models. The motivation behind picking these two modeling cases is expounded further in the following sub-sections.

1.1 Co-electrolysis of CO₂ and H₂O¹

Unlike PEM cells, SOECs can be used for the co-electrolysis of steam and carbon dioxide. The higher operating temperature allows for the use of cheaper, more stable and less active, non-noble metal catalysts, thereby preventing CO-poisoning [1]. Additionally, higher temperatures lead to higher reaction rates thereby reducing the electrical energy demand since a notable amount of reaction energy is supplied by heat [2].

Subsequently, the industrial implementation of SOECs is very promising, as waste heat from other processes can be used to heat the cells leading to an increase in both thermal and cost efficiency. Here, co-electrolysis of steam and carbon dioxide is of special interest. The two reactants, typically waste products in an industrial plant, are turned into “syngas” (CO+H₂), a valuable and very commonly used reagent in the chemical industry.

Syngas is used to produce synthetic fuels or other liquid hydrocarbons via Fischer-Tropsch synthesis or for methanol synthesis and hydroformylation [3]. In today’s industry, it is mainly produced in large scale plants by either catalytic steam reforming (STR), auto-thermal reforming (ATR) or catalytic partial oxidation (CPOX) of hydrocarbons, typically methane [3,4]. While there have been considerable efforts to improve these processes to produce hydrogen for cars and other fuel cell applications [5–7], all of them rely on natural gas or other fossil fuels as a resource. In addition, these processes require a relatively big

¹ Parts of this section have been taken from A. Banerjee, Y. Wang, J. Diercks and O. Deutschmann, Hierarchical Modeling of Solid Oxide Cells and Stacks producing Syngas via H₂O/CO₂ Co-electrolysis for Industrial Applications, Appl. Energy 230 (2018) 996-1013.

scale to be capital cost effective and the produced H₂:CO ratio cannot be easily adjusted, leading to different processes and plants being required to produce syngas for different applications [8]. In contrast to these conventional methods, co-electrolyzers consume carbon-dioxide instead of fossil fuels, can produce an adjustable H₂:CO ratio [9], and can be conveniently decentralized and varied in scale by the stacking of unit cells.

As renewable energy sources are increasingly integrated in electricity grids, the demand for flexible electricity storage to buffer the more volatile power production of wind and solar plants grows. Utilizing solid oxide cells for co-electrolysis offers a flexible solution to store the excess electricity as an industrially valuable product whilst using industrial waste as a reactant. The prospect of chemically converting carbon dioxide, a “greenhouse gas”, into polymers, hydrocarbons and base chemicals without relying on fossil fuels is highly promising, especially when renewable energy is used to operate the cell.

In light of this, the performance of SOECs as single cells and cell stacks for co-electrolysis has been experimentally investigated by several groups [10–13]. Chen et al. tested different oxygen electrodes in a 10-cell stack and showed the feasibility of long term operation [10] while Reytier et al. presented a high performance stack design using 10 and 25 cells [11]. Cinti et al. utilized both model and experiment to uncover that chemical as well as electrochemical reactions contribute to the obtained syngas ratio and that it can be easily adjusted by the inlet H₂O/CO₂ ratio as well as thermodynamic operating conditions [12]. However, Nguyen et al. have found degradation in co-electrolysis to be a little higher than in steam electrolysis in long term tests of over 8000 hours [13].

Since the various physico-chemical phenomena taking place inside a solid oxide co-electrolysis cell join together to form a complex interconnected network, several modeling studies have also been performed to help better understand these devices and uncover the processes limiting their performance [2,14–19]. Xie et al. and Li et al. developed models to understand the reaction and transport processes of a SOEC during co-electrolysis leading to insights on surface species and coverage, coking processes and adsorption/desorption rates [14,15]. Aicart et al. found the anode activation overpotential, i.e. the oxygen evolution reaction, to be the main contributor to the cell voltage increase [16] while Kazempoor et al. elucidated the importance of contact resistance, activation polarization and the influence of the water-gas shift reaction on the electrolyzer performance [17]. Ni

developed a 2-D thermal model to investigate the heat/mass transfer dependencies for planar cells [18] while Luo et al. used a 2-D thermal model to analyze and improve the efficiency and conversion of tubular cells [2,19].

However, to achieve commercial yields of product gases, single cells need to be stacked into larger units. Given the size of an industrially used SOEC stack, the behavior of each cell is dependent on its position in the stack because of temperature gradients resulting from heat exchange with the surroundings. Since an increase in temperature improves reaction kinetics, gas transport through the porous electrodes, and oxygen ion transport through the solid electrolyte, it might not be sufficient to model an isolated unit cell or repeating unit under isothermal or adiabatic conditions as reported in [2,18–20] to analyze stack performance.

Due to co-electrolysis in ceramic cells being a relatively new field of study, the research focus has primarily been on improving materials and cell design, with very few publications focusing on the integration of the process into larger systems. Fu et al. performed an economic assessment of a co-electrolyzer to produce syngas for a commercial Fischer-Tropsch plant using process modeling and sensitivity analysis [21]. A systems-level model has also been used to combine a co-electrolysis plant and a Fischer-Tropsch plant in an industrial environment to calculate system efficiency and analyze production costs [22]. However, to the author's best knowledge, the effect of transitioning from lab-scale unit cells to commercial scale stacks on cost, performance and reliability has not yet been investigated.

1.2 Oxygen reduction/evolution reaction²

One of the major stumbling blocks towards commercialization of SOCs is the optimal design of air electrodes and selection of materials that readily catalyze the oxygen reduction/evolution reaction (ORR) [23]. In fact, polarization resistance due to slow ORR kinetics is widely acknowledged to be the dominant source of losses especially in the low-intermediate temperature range of operation for SOCs [24,25] as well as for solid oxide co-electrolysis cells [13,16,26]. Acceptor-doped transition metal oxides with high electron

² Parts of this section are taken with permission from [49] A. Banerjee, O. Deutschmann, Elementary kinetics of the oxygen reduction reaction on LSM-YSZ composite cathodes, *J. Catal.* 346 (2017) 30-49.

conductivities serve as attractive low cost alternatives to noble metals for use as air electrodes owing to their superior oxygen exchange coefficients [27,28]. Lanthanum strontium manganite (LSM) is one such material. Although newer materials have been developed with superior catalytic activity towards O_2 reduction, LSM remains technologically relevant due to its excellent blend of catalytic activity, thermal and mechanical stability, and compatibility with yttria-stabilized zirconia (YSZ), a traditional SOFC electrolyte [24]. However, owing to its poor ionic conductivity, the active area for catalytic reaction is insufficient in single phase LSM electrodes. A potential solution is the introduction of an ionic YSZ phase resulting in a porous LSM-YSZ composite. The state of the art LSM-YSZ composite air electrodes perform significantly better than the single phase LSM air electrodes due to a much larger utilization region [29–31].

A vital component in improving the design and performance of LSM-YSZ composite air electrodes is a deeper understanding of the underlying ORR mechanism. To that end, electrochemical impedance spectroscopy (EIS) has emerged as a powerful measurement technique to spell out the fundamental processes occurring in an electrode. Numerous experimental studies employing EIS, as reviewed comprehensively by Adler [24], have been performed to try and gain deeper insights into the reaction pathways and rate-limiting steps for oxygen reduction on SOFC air electrodes. However, the measured spectra are complex, influenced by many factors and thus difficult to interpret, especially for composite electrodes [32].

From a modeling standpoint, various quantum chemical and molecular dynamics studies have been conducted on non-stoichiometric oxides in general [33–35], and LSM in particular [36–38], to try and uncover oxygen reduction kinetics from first principles. While these studies are crucial to determining the stability and energy of different transition states and reaction intermediates, the microscopic particle simulations are unable to simulate macroscopic measures of performance like impedance spectra and polarization curves. This limitation of the quantum chemical approach is overcome by continuum models that serve as a bridge between microscale molecular simulations and macroscale impedance measurements. Multi-physics based continuum models, employing elementary kinetics informed by density functional theory (DFT), have already been used to simulate impedance spectra and polarization curves for a few fuel and air electrodes [39–42]. Yet, owing to the complexity and randomness of the porous microstructure, none of these

mechanisms have been demonstrated to be ‘intrinsic’, i.e. capable of reproducing large sets of experimental data from distinct and independent sources for a given reaction system and for a given material. This fact precludes SOC models from being a universal predictive design tool, since the kinetic models are only valid for the set of experiments against which they were calibrated.

The use of elementary kinetics is also not without its own challenges. Kinetic rate constants comprising of pre-exponential factors and activation energies for all elementary steps must be specified, alongside thermodynamic parameters like enthalpies and entropies of all reacting species, to ensure a thermodynamically consistent mechanism. Therefore, it is important to select reaction systems which have a sizeable repository of kinetic and thermodynamic data published in the literature, as candidates for detailed mechanistic models. Since, LSM-YSZ composites are a staple of the SOFC community, O₂ reduction on LSM-YSZ composites has been investigated for well over ten years [24]. It is a well-characterized reaction system (both numerically and experimentally) and is ideally suited to elementary kinetic modeling.

1.3 Objectives of the present work

The first objective of the present work is to develop a comprehensive and consistent model with sufficient flexibility to handle the different length and time scales of the physics involved in a solid oxide cell. As the modeling domains scale up from lab-scale half or symmetrical cells used for material characterization (μm - mm length scales) to commercial stacks (cm - m length scales), a hierarchical modeling approach is paramount to ensure information from physics occurring at the nm - μm length scales is not lost. The modeling methodology described in Chapter 2 illustrates such a modeling approach and the results presented in Chapter 3 demonstrate the capabilities of the hierarchical cell and stack model using solid oxide co-electrolysis as an example case.

Once such a model has been established, the second objective is to make strides towards the development of a SOC model that can be used as a universal tool for cell and stack design, reliability and lifetime estimates as well as real-time monitoring and maintenance of the solid oxide cell and stack. A very important step in attaining this objective is the development of an electrochemical reaction kinetic expression decoupled from transport effects and intrinsic to the material. As mentioned earlier in section 1.2, SOC models are

frequently restricted to being diagnostic and analytical tools since the electrochemical reaction kinetic models typically need to be re-parameterized when trying to reproduce experimental data from two cells comprising of the same materials and configuration. This is due to the significant influence of the electrode microstructure on kinetics as underlined in Fig. 1.2. The figure depicts the substantially different EIS curves measured under air and an operating temperature of 973.15K for the same LSM-YSZ half-cell sintered under the same conditions by three different research groups [43–45]. The difference in the EIS responses is solely due to the random microstructure resulting from the sintering process. This randomness of the microstructure is one of the reasons for the lack of intrinsic kinetic expressions mentioned earlier in section 1.2 as the kinetic fit parameters likely contain contribution due to gas or charge transport through the microstructure. Since the model developed in this work can separate the effects of transport from kinetics, the pursuit of an intrinsic kinetic model for the O_2 reduction/ evolution reaction on LSM-YSZ composite air electrodes is detailed in Chapter 4.

Lastly, the relative success or failure of the presented work in accomplishing the objectives set here is discussed in Chapter 5 along with a summary of the key results, conclusions and recommendations for future work.

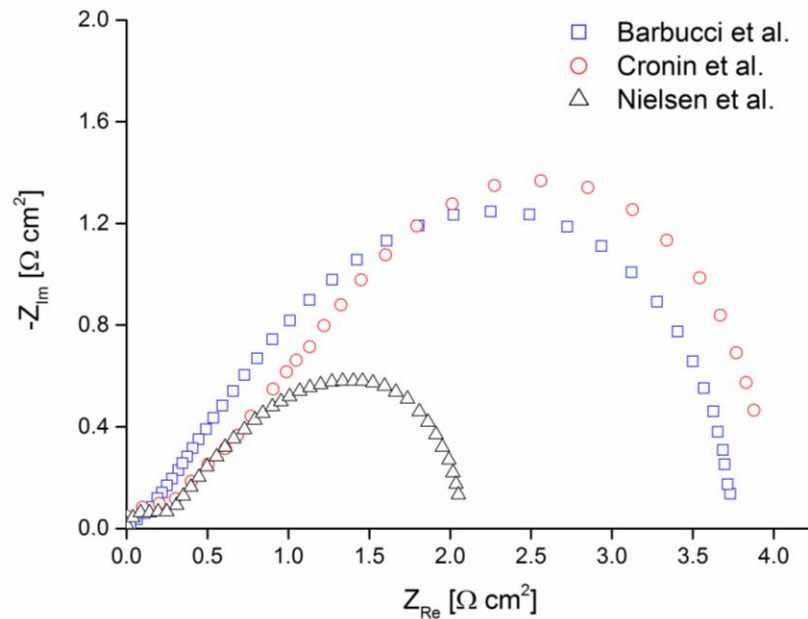


Figure 1.2. Nyquist plots for LSM-YSZ half-cells from different literature sources [43–45] illustrating the effect of the random electrode microstructure resulting from the electrode sintering process.

Chapter 2

Modeling Methodology³

A description of the general set of governing equations used to model a solid oxide cell in different configurations namely button cell, half-cell, planar cell or repeating unit (RU)⁴, and a stack of cells or repeating units is presented in this chapter. The assumptions and methodology specific to the two cases presented in Chapters 3 and 4 are discussed in their respective chapters. For example, the details of co-electrolysis of H₂O and CO₂ and ORR electrochemistry are reported in Chapters 3 and 4 respectively.

Before setting up the system of governing equations, the different SOC configurations are briefly summarized. A button cell is a single SOC used to characterize the cell performance. The gas flow to a button cell is perpendicular to the cell and can be approximated one-dimensionally along the cell thickness. Current collection is accomplished by metallic (e.g. gold or platinum) grids [46]. A half-cell is essentially a button cell where either the fuel or air electrode has been replaced by an ideal counter electrode since the focus of interest is the other working electrode. For example, in Chapter 4, the experiments simulated are performed on half-cells with the working electrode being the air electrode and the fuel electrode replaced by an ideal counter electrode. As the name implies, in a planar cell or RU the gas flow is parallel to the surface of the cell as the gas is now bounded by the electrode surface on one side and metallic interconnects on the other three sides [47]. The planar flow results in a 2-D effect as the diffusion through the membrane-electrode assembly (MEA) i.e. the electrodes and electrolyte, is transverse to the gas flow. The metallic interconnects help facilitate current collection as well as act as a separator between neighboring repeating units when the cells are placed on top of each other to form a stack.

³ Parts of this section are taken with permission from [49] A. Banerjee, O. Deutschmann, Elementary kinetics of the oxygen reduction reaction on LSM-YSZ composite cathodes, *J. Catal.* 346 (2017) 30-49 and from A. Banerjee, Y. Wang, J. Diercks and O. Deutschmann, Hierarchical Modeling of Solid Oxide Cells and Stacks producing Syngas via H₂O/CO₂ Co-electrolysis for Industrial Applications, *Appl. Energy* 230 (2018) 996-1013.

⁴ A repeating unit is essentially a planar unit cell comprising of a single air and fuel channel flanked by interconnect plates on all four sides. A planar cell comprises of multiple repeating units.

The introduction of interconnects however, creates an additional resistance to the flow of electrons due to imperfect contact at the electrode-interconnect interfaces and modifies the thermo-fluidic transport in the cell.

Whether flowing axially or radially, the physics describing the path of the reactant gas molecules after percolating into the porous electrodes is identical for all configurations. Driven through the porous matrix of ion and electron conducting electrode particles by ordinary and Knudsen diffusion in conjunction with Darcy flow, the reactant gas molecules participate in thermochemical reactions on the electrode surface and combine with electrons and O^{2-} ions at the electrode-electrolyte interfaces to form the desired products. Schematic representations of the modeling domain showing the hierarchical approach used to simulate solid oxide co-electrolyzers in Chapter 3 and the half-cell used to investigate the ORR kinetics in Chapter 4 are shown in Figs. 2.1 and 2.2. The figures illustrate the physics involved and the course charted by the gas molecules.

In formulating the mathematical model, the following assumptions were made

1. The sintered porous electrodes are approximated as a homogeneous continuum of spherical particles with random percolating clusters of charge conducting particles interspersed with spherical pores.
2. The thin metallic grids in button cells have no impact on bulk gas transport and offer no resistance to charge transport, i.e. they are ideal current collectors.
3. The inlet flow rate to the button cells is sufficiently high to ensure perfect mixing, i.e. there are no spatial concentration gradients.
4. The plug flow model describes the flow in the RU gas channels.
5. The inlet and outlet gas manifolds of the stack are not modeled.
6. Species and charge transport are one dimensional along the thickness of the electrodes.
7. The dense electrolyte is a pure ionic conductor, i.e. there is no electronic leakage across it.
8. The voltage applied to the RU has no axial gradients since the interconnects have minimal electronic resistance.

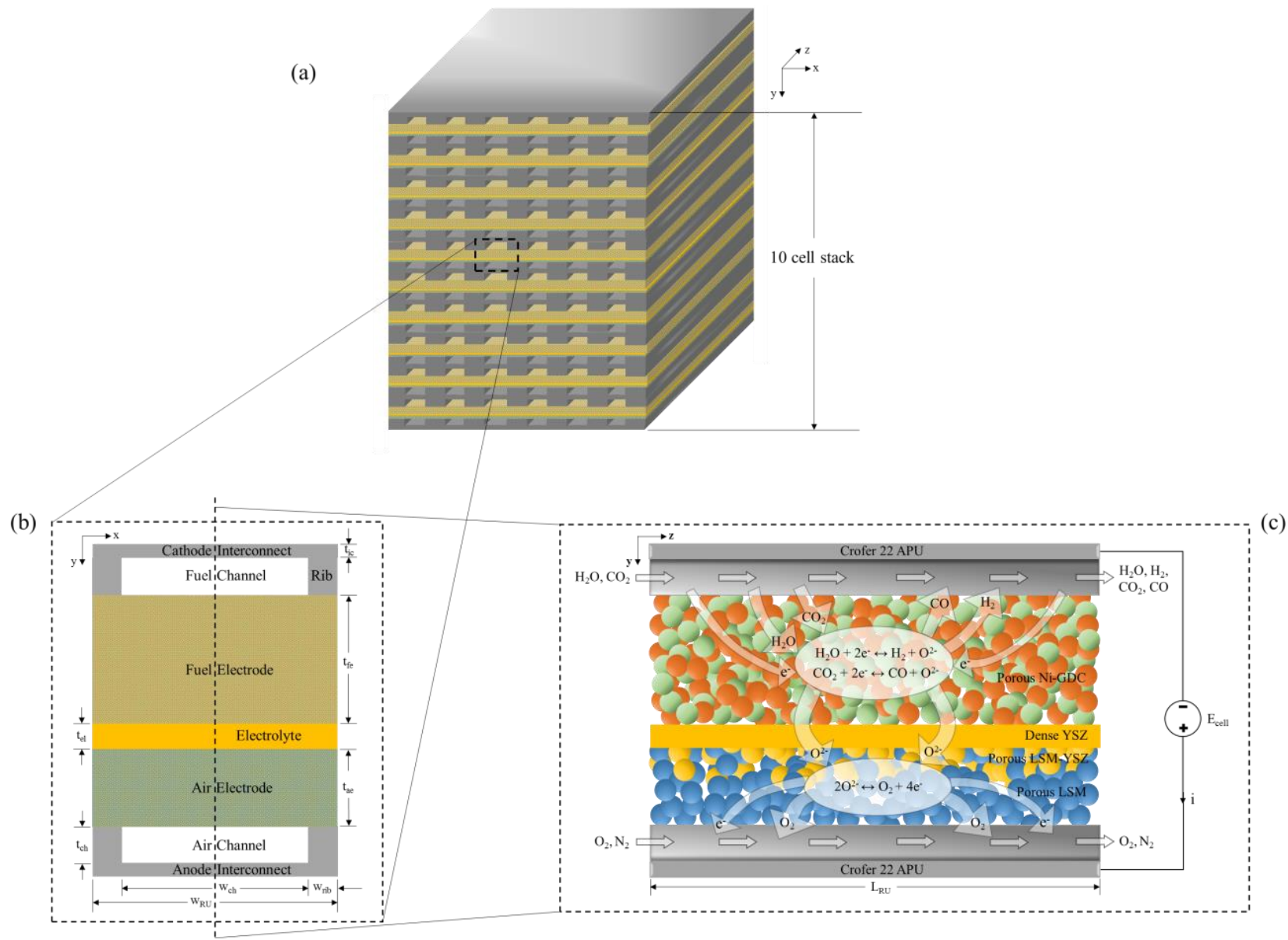


Figure 2.1. (a) Schematic of the modeling domain of an example 10 cell stack for co-electrolysis of steam and carbon dioxide. (b) Front-view of a single repeating unit of the stack showing the various components. (c) Cut-away view along the xy-plane of the repeating unit illustrating the different physico-chemical processes.

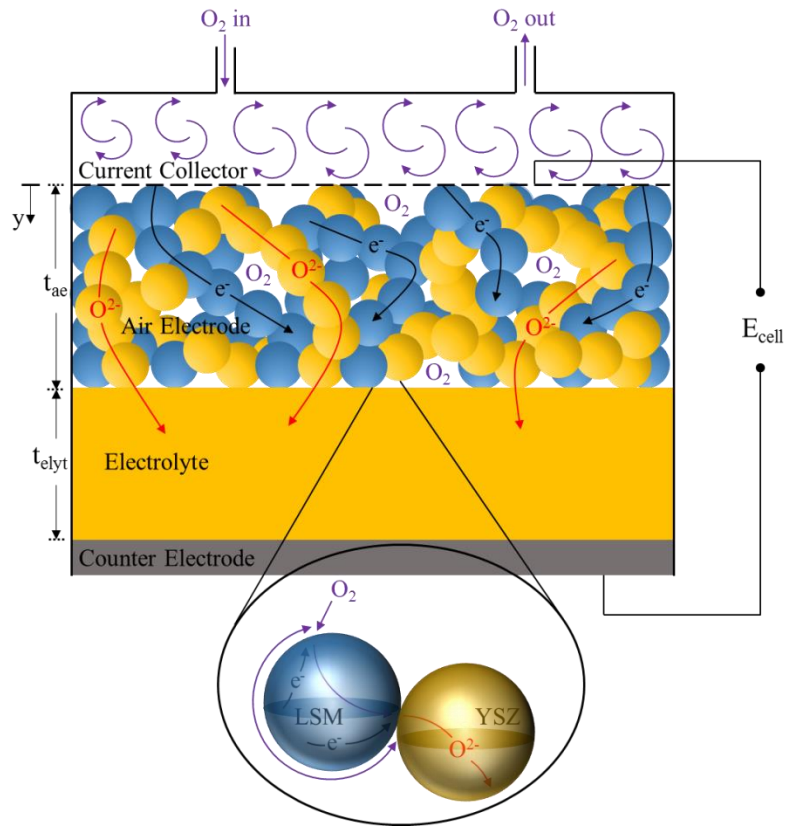


Figure 2.2. Schematic of the modeling domain illustrating the various transport phenomena and oxygen reaction pathways through the LSM and YSZ particles.

9. Electronic and ionic conduction in the porous composite electrodes are modeled using Ohm's law and the diffusive fluxes due to charge carrier concentration gradients are neglected.
10. For half-cells, the counter electrode is ideal and the potential drops across the current collector-working electrode and electrolyte-counter electrode interfaces are neglected, i.e. the cell voltage, E_{cell} , is equal to the sum of the potential drops across the working electrode and electrolyte.
11. The electrodes and interconnects are assumed to be gray and opaque.
12. Local temperature gradients in the solid components of a stack are negligible, i.e. all the solid components including the electrodes, electrolyte and interconnects are lumped into one solid phase when constituting the energy conservation equation for the stack.

The system of differential algebraic equations arising as a result of these assumptions is based on a framework detailed in prior publications on button cells [48,49], single planar

unit cells [20,50,51] and stacks [52]. In the following subsections, the principal elements of the model are discussed.

2.1 Mass and Momentum Conservation

2.1.1 Bulk gas phase

In the absence of concentration gradients due to perfect mixing, a steady-state lumped continuously-stirred tank reactor (CSTR) model is used to calculate the mass fraction of a species k , Y_k , in the gas compartment of a button cell as a function of the inlet species mass fraction $Y_{k,i}$ and the inlet mass flow rate \dot{m}_i ,

$$Y_k = \frac{\dot{m}_i Y_{k,i} - J_k W_k}{\dot{m}_i - \sum_{k=1}^{K_g} J_k W_k} \quad (2.1)$$

Here, W_k is the molecular weight of k , J_k is the molar flux of k coming from the electrode and K_g is the total number of gas-phase species. A CSTR model has been previously shown to capture low frequency contributions to the impedance spectra due to gas conversion [53], though in the high-flow limit as considered here, such contributions are neglected.

In a planar RU, a transient plug flow model enforces species continuity in the gas channels,

$$\frac{\partial(\rho_g Y_k)}{\partial t} = -\frac{\partial(\rho_g u Y_k)}{\partial z} + \frac{1}{t_{ch}} J_k W_k, \quad k = 1, \dots, K_g \quad (2.2)$$

Here, Y_k is the mass fraction of k , ∂z is the finite volume element length along the flow direction, and t_{ch} is the channel thickness. The local mean velocity u is evaluated from the momentum equation by assuming constant pressure in the gas channels,

$$\frac{\partial(\rho_g u)}{\partial t} = -\frac{\partial(\rho_g u u)}{\partial z} + u \sum_{k=1}^{K_g} \frac{1}{t_{ch}} J_k W_k \quad (2.3)$$

and, the local gas density ρ_g is obtained from the ideal-gas equation of state,

$$\rho_g = \frac{p}{RT} \frac{1}{\sum_{k=1}^{K_g} Y_k / W_k} \quad (2.4)$$

where, R is the universal gas constant and T is the local temperature.

To check whether the plug flow model is reasonable to describe the species transport within the RU gas channels, Raja et al. defined a range of validity based on the product of the

characteristic Reynolds and Schmidt numbers [54]. For example, over the range of conditions investigated in Chapter 3, the flow in the long and thin gas channels ($L_{ch} \gg d_{ch}$) is laminar ($6 \leq Re \leq 20$) and the Schmidt number (Sc) is $\sim 0.1-1$. Therefore, the product of the Reynolds and Schmidt numbers are of the order of $10^{-1}-10^0$. The lower and upper bounds of the range of validity are given by the ratios d_{ch}/L_{ch} and L_{ch}/d_{ch} and are 10^{-2} and 10^1 respectively for the RU geometries studied. Thus, $d_{ch}/L_{ch} < ReSc < L_{ch}/d_{ch}$ indicating that the flow is fully developed with concentration gradients one dimensional along the stream-wise direction.

2.1.2 Porous media

Mass transport through the pore phase of the porous electrodes is modeled using the transient reaction diffusion equation to evaluate species densities ρ_k .

In the pore phase of the electrodes,

$$\frac{\partial(\epsilon\rho_k)}{\partial t} = -\frac{\partial(J_k W_k)}{\partial y} + \dot{s}_k W_k A_{gas/ede}^V, \quad k = 1, \dots, K_g \quad (2.5)$$

and,

$$\frac{\partial(\epsilon\rho_g)}{\partial t} = -\sum_{k=1}^{K_g} \frac{\partial(J_k W_k)}{\partial y} + \sum_{k=1}^{K_g} \dot{s}_k W_k A_{gas/ede}^V \quad (2.6)$$

Here, ϵ is the porosity of the porous media, ∂y is the finite volume length along the thickness, \dot{s}_k is the molar production rate of k due to heterogeneous reactions on the electrode surface, and $A_{gas/ede}^V$ is the specific surface area of the electrode.

The species molar flux J_k present in all the governing equations for mass transport in the gas phase is evaluated using the Dusty-Gas model (DGM),

$$J_k = -\left[\sum_{l=1}^{K_g} D_{kl}^{DGM} \nabla[X_l] + \left(\sum_{l=1}^{K_g} \frac{D_{kl}^{DGM}[X_l]}{D_{l,Kn}^e} \right) \frac{B_g}{\mu} \nabla p \right] \quad (2.7)$$

The contributions due to diffusion and advection are given by the first and second terms respectively. A pressure gradient ∇p arising because of density fluctuations due to species addition/depletion leads to an advective flux driven by a Darcy velocity in the porous media. The permeability or resistance B_g of the porous media to Darcy flow is given by the

Carman–Kozeny relationship for a bed of densely-packed spherical particles [55],

$$B_g = \frac{\epsilon^3 d_p^2}{72\tau_{fac}(1 - \epsilon)^2} \quad (2.8)$$

where, d_p is the particle diameter.

D_{kl}^{DGM} in Eq. 2.7 are DGM diffusion coefficients which are obtained by inverting a matrix H whose elements h_{kl} are given by

$$h_{kl} = \left[\frac{1}{D_{k,Kn}^e} + \sum_{j \neq k} \frac{X_j}{D_{kj}^e} \right] \delta_{kl} + (\delta_{kl} - 1) \frac{X_k}{D_{kl}^e} \quad (2.9)$$

Here, $D_{k,Kn}^e$ is the effective Knudsen diffusion coefficient, D_{kl}^e is the effective binary diffusivity between species k and l , X_k is the mole fraction of k , and δ_{kl} is the Kronecker delta. $D_{k,Kn}^e$ considers diffusive transport due to collisions of the gas molecules with the pore walls and is a function of the mass of the molecule and the pore diameter d_{pore} ,

$$D_{k,Kn}^e = \frac{\epsilon}{\tau_{fac}} \frac{d_{pore}}{3} \sqrt{\frac{8RT}{\pi W_k}} \quad (2.10)$$

whereas, diffusion due to inter-molecular collisions are given by D_{kl}^e [56],

$$D_{kl}^e = \frac{\epsilon}{\tau_{fac}} D_{kl} \quad (2.11)$$

The binary diffusivities D_{kl} and the mixture viscosity μ are evaluated using standard expressions derived from kinetic theory [57].

DGM owes its name to the fact that it treats the pore walls as uniformly distributed ‘dust particles’ and considers the ‘dust particles’ to be a pseudo-species in the dusty gas mixture. DGM combines the Stefan-Maxwell formulation for multi-component ordinary diffusion with Knudsen diffusion through addition of momentum transfer and utilizes the Chapman-Enskog kinetic theory to combine transport fluxes due to diffusion and advection. DGM is superior to the commonly used advective-Fick model (AFM) since DGM incorporates the experimentally observed Graham’s law of diffusion while AFM assumes equimolar counter diffusion [58]. Therefore, when dealing with multiple gas-phase species and low pore diameters, as is the case with porous SOC electrodes, DGM presents itself as the most suitable choice.

Equations 2.8, 2.10 and 2.11 require the evaluation of a factor τ_{fac} to account for the long

winding nature of the diffusion path L_{diff}^e present in a randomly percolating pore cluster of a porous medium as opposed to the straight diffusion paths L_{diff} present in the bulk gas phase. The factor, commonly called the tortuosity factor, is defined according to [56],

$$\tau_{\text{fac}} = \left(\frac{L_{\text{diff}}^e}{L_{\text{diff}}} \right)^2 \quad (2.12)$$

For a bed of randomly-packed spheres, τ_{fac} can be evaluated analytically as a function of the porosity of the medium [59],

$$\tau_{\text{fac}} = \left(1.23 \frac{(1 - \epsilon)^{4/3}}{\epsilon} \right)^2 \quad (2.13)$$

However, Eq. 2.13 tends to underestimate τ_{fac} . While, experimental τ_{fac} values measured by X-ray tomography and FIB-SEM techniques range from 1.8-2.8 for electrode porosities of 0.45-0.5 [60–62], the corresponding analytical values from Eq. 2.13 are in the range of 0.95-1.5. This result underscores one of the limitations of approximating the sintered electrode microstructure as a bed of spherical particles. To tackle this problem, Zhu and Kee [50] have previously used a much lower value of $\epsilon=0.35$ to qualitatively reproduce measurements for a Ni-8YSZ electrode with $\epsilon=0.54$. The same approach is followed here.

On the electrode surfaces, a mass balance gives the coverages θ_k of the adsorbed reaction intermediates k ,

$$\frac{\partial \theta_k}{\partial t} = \frac{\zeta_k \dot{s}_k}{\Gamma_s} \quad (2.14)$$

where ζ_k is the number of adsorption sites required by k and Γ_s is the density of available active sites on the surface (or surface site density). For common electrode materials like Ni and YSZ, $\Gamma_s = 2.66 \times 10^{-9} \text{ mol cm}^{-2}$ [20] and $1.25 \times 10^{-9} \text{ mol cm}^{-2}$ [41]. The surface site density of LSM is evaluated based on a unit cell cut along the (100) plane of the perovskite crystal having a lattice constant of 3.7975 \AA . The (100) plane, which is the most stable among the low-index surfaces [14], has four active Mn sites at the corners shared among four adjacent unit cells leading to a total site density of $6.934 \times 10^{14} \text{ cm}^{-2}$ (i.e. $1.15 \times 10^{-9} \text{ mol cm}^{-2}$).

The formulation of the reaction source term \dot{s}_k in Eqs. 2.6 and 2.14 is specific to the reaction systems studied and is thus defined separately in Chapters 3 and 4.

2.1.3 Boundary Conditions

The solution of spatial gradients in Eqs. 2.2, 2.3, 2.5 and 2.6 mandate appropriate fixed value or constant flux conditions at the axis boundaries of the modeling domain. For the species and momentum conservation equations in the channel, the inlet is set to a specified gas composition and flow velocity respectively. To solve the species transport equations in the porous electrodes, the species composition at the channel-electrode interface is set to the species composition in the channel bulk. At the electrode-electrolyte interface, the species flux is set to zero for all species not participating in charge transfer reactions. For the electrochemically active species, the species flux is calculated from the current density i ,

$$J_k = \frac{\nu_k W_k i}{n_e F} \quad (2.15)$$

where, ν_k is the stoichiometric coefficient of species k in the charge transfer reaction (negative for reactants and positive for products), n_e is the number of electrons transferred and F is the Faraday constant.

2.2 Charge Conservation

2.2.1 Distributed Charge Transfer

The analogous form of the volume-averaged species continuity equation for charge conservation is the so-called ‘distributed charge transfer model’, which conserves charge individually for the ionic and electronic phases, in each finite volume of the MEA. A flux of charge, or current density, driven by gradients in charge concentration, or electric potential, enters a finite volume where charge is either lost or gained by the bulk volume due to charge accumulation and consumed or produced due to electrochemical reactions. The remaining flux of charge exits the volume. Since it is typically assumed that charge accumulation takes place only in the electric double layers (DL) at the interface of the two phases, no net charge is gained by the MEA bulk [63]. Thus, for the electronic phase

$$i_{el} = \frac{\partial}{\partial y} \left(\sigma_{el}^e \frac{\partial \phi_{el}}{\partial y} \right) = i_F^V + i_{DL}^V \quad (2.16)$$

and, for the ionic phase

$$i_{io} = \frac{\partial}{\partial y} \left(\sigma_{io}^e \frac{\partial \phi_{io}}{\partial y} \right) = -(i_F^V + i_{DL}^V) \quad (2.17)$$

Here, $\sigma_{\text{el}}^{\text{e}}$ and $\sigma_{\text{io}}^{\text{e}}$ are the effective electronic and ionic conductivities, ϕ_{el} and ϕ_{io} are the local electronic and ionic bulk phase potentials and i_{F}^{V} and i_{DL}^{V} are the volumetric faradaic and capacitive current source terms respectively.

A simple Helmholtz model is used to calculate the volumetric current source term due to charge accumulation at the electric double layer between the electronic and ionic phases [64],

$$i_{\text{DL}}^{\text{V}} = A_{\text{el/io}}^{\text{V}} \frac{\partial}{\partial t} \left(C_{\text{DL}}^{\text{el/io}} \Delta\phi \right) \quad (2.18)$$

where $C_{\text{DL}}^{\text{el/io}}$ is the interfacial DL capacitance and $\Delta\phi$ is the difference between the electronic and ionic bulk phase potentials at the interface, i.e. $\Delta\phi = \phi_{\text{el}} - \phi_{\text{io}}$. $C_{\text{DL}}^{\text{el/io}}$ is temperature dependent and for the case of commonly used composite electrodes such as Ni-YSZ and LSM-YSZ, set to electrochemical DL capacitance data obtained by Hendriks et al. for YSZ [65].

The faradaic current source term accounts for the volumetric charge produced or consumed due to electrochemical reactions and its formulation depends on the electrochemical reaction system. It is defined in Chapter 4 when describing the ORR electrochemistry.

With i_{el} and i_{io} evaluated, the net current density i is calculated simply as $i = i_{\text{el}} + i_{\text{io}}$. As per common convention, i is considered positive when it is drawn from the cell, i.e. SOFC mode and negative when supplied to the cell, i.e. SOEC mode.

2.2.2 Boundary Conditions

Equations 2.16 and 2.17, like Eqs. 2.2, 2.3, 2.5 and 2.6, are boundary value problems. For the electronic phase, the electron flux disappears at the electrode-electrolyte interface and conversely, for the ionic phase, the ion flux disappears at the current collector-electrode interface. Furthermore, the electronic phase potential is set to E_{cell} at the current collector-air electrode interface and zero at the current collector-fuel electrode interface. For a half-cell, the electronic phase potential at the current collector-working electrode interface is set to E_{cell} or $-E_{\text{cell}}$ depending on whether the working electrode is the air electrode or the fuel electrode while the ionic phase potential at an equipotential surface in the electrolyte bulk, i.e. the reference electrode potential [66], is set to zero. Bessler et al. posited that the

electrolyte equipotential surface can be found in the vicinity of the electrolyte center [67] whilst Goodwin et al. assumed it is located at the interface between the working electrode and the electrolyte [41]. In this work, the location of the equipotential surface is approximated from the experimental ohmic drop. For thin electrolytes ($\sim 125\text{-}150\ \mu\text{m}$), the surface is found to be at the electrolyte-counter electrode interface, whereas for thick electrolytes ($\sim 2\ \text{mm}$), the surface is determined to be $\sim 350\ \mu\text{m}$ from the working electrode-electrolyte interface.

2.2.3 Interfacial Charge Transfer

Due to the presence of the dense electrolyte, it is obvious that electrochemical reactions do not occur over the entire MEA. In fact, for cells made up of metal electrodes (pure electronic conductors) sintered to a purely ion conducting electrolyte (e.g. Pt|YSZ|Pt), electrochemical reactions occur only at the electrode-electrolyte interface since charge transfer is driven by the difference between the potentials of the ionic and electronic phases. Though modern day cells use composite electrodes containing both ionic and electronic phases, the ‘utilization region’ of the electrode where electrochemical reactions occur, is typically restricted to within $\sim 10\text{-}20\ \mu\text{m}$ on either side of the electrolyte [49,68,69]. As a result, the current density through the MEA, outside of this utilization region, is constant.

For cells with thick electrodes, e.g. the fuel electrode-supported F-design planar cells from Forschungszentrum Jülich with a fuel electrode thickness of 1-1.5 mm [70], the utilization region is only a small fraction of the total thickness. Thus, it may be reasonable to assume that charge-transfer occurs within an infinitesimally small region around the electrode-electrolyte interface. As a result, the spatially resolved charge conservation equation can be reduced to a potential balance at the interface and the electrochemical reactions occurring throughout the utilization volume of the composite electrodes may be lumped into fluxes at the electrode-electrolyte interface. This lumped and computationally cheap formulation is commonly called the ‘interfacial charge transfer model’. Zhu and Kee [71] have previously reported a very close agreement between the interfacial and distributed charge transfer models for a cell with a fuel electrode thickness of $400\ \mu\text{m}$ and an air electrode thickness of $50\ \mu\text{m}$.

The interfacial potential balance comprises of the reversible potential within the cell E_{rev} ,

the potential E_{cell} drawn or supplied to the cell depending on whether the cell is in fuel cell or electrolysis mode, and all the irreversible potential sinks, or overpotentials, due to ohmic and activation losses that manifest when the cell is polarized. Since gas transport through the electrodes is modeled explicitly, the species activities required in the Nernst equation are evaluated at the electrode-electrolyte interface. Thus, the potential sink due to concentration losses is not included in the potential balance,

$$E_{\text{cell}} = E_{\text{rev}} + \eta_{\text{act,fe}} + \eta_{\text{act,ae}} + \eta_{\text{ohm}} \quad (2.19)$$

Here, the subscripts fe and ae denote the fuel electrode and air electrode respectively.

E_{rev} , which is the maximum potential that can be drawn out from a cell in fuel cell mode, is a function of the operating cell temperature, pressure and gas composition as described by the Nernst equation,

$$E_{\text{rev}} = \frac{\Delta G_r^0}{n_{e,r}F} + \frac{RT}{n_{e,r}F} \ln \left(\frac{\prod_{k \in R_b} p_k^{v_k''}}{\prod_{k \in R_f} p_k^{v_k'}} \right) \quad (2.20)$$

Here, ΔG_r^0 is the Gibbs free energy of the electrochemical reaction and v_k' and v_k'' are the stoichiometric coefficients of the reactants and products respectively. The partial pressure of each species k reacting either in the forward reaction R_f or in the backward reaction R_b is denoted by p_k . The partial pressures are evaluated at the electrode-electrolyte interface.

The ohmic overpotential η_{ohm} is the irreversible loss of potential caused due to the intrinsic resistivity of a charge conductor in accordance with Ohm's law. Its origins are microscopic and is caused due to the bulk flow of electrons through a conductor due to a potential difference across its ends. The electrons drift towards the positive potential and collide with the atoms of the conductor along the way causing them to take a more tortuous path instead of a straight one. In a solid oxide cell,

$$\eta_{\text{ohm}} = \left(\frac{t_{\text{fe}}}{\sigma_{\text{fe}}^e} + \frac{t_{\text{elyt}}}{\sigma_{\text{elyt}}} + \frac{t_{\text{ae}}}{\sigma_{\text{ae}}^e} + R_{\text{contact}} \right) i \quad (2.21)$$

Here, i is the current density flowing through the conductor, t_{fe} , t_{elyt} and t_{ae} are the thicknesses of the fuel electrode, electrolyte and air electrode respectively and σ_{elyt} is the intrinsic conductivity, i.e. inverse of resistivity, of the dense electrolyte. The two remaining conductivities, σ_{fe}^e and σ_{ae}^e are the effective conductivities of the composite fuel and air electrodes. They are a function of the electrode microstructure and the intrinsic

conductivities of their bulk ionic and electronic phases. The method for evaluating these properties are discussed further in section 2.4 of this chapter. The last contribution to the ohmic overpotential, as specified in Eq. 2.21, is due to the contact resistance R_{contact} . For button cells, this term is negligible since current collection is nearly perfect. However, in planar repeating units and stacks, current collection via interconnect ribs is more of a challenge and this term can become quite significant without the use of contact layers and optimal rib widths to help facilitate the conduction of charge from the electrodes to the interconnects [72–74].

The activation overpotential η_{act} , as the name suggests, is the potential spent to activate the electrochemical reactions when they are driven forward or backward from equilibrium. As mentioned earlier in this subsection, charge transfer is driven by the potential difference between the electrode and electrolyte at their interface, i.e. $\phi_{\text{fe}} - \phi_{\text{elyt}}$ and $\phi_{\text{ae}} - \phi_{\text{elyt}}$. Therefore, $\eta_{\text{act,fe}} = (\phi_{\text{fe}} - \phi_{\text{elyt}}) - (\phi_{\text{fe}}^{\text{eq}} - \phi_{\text{elyt}}^{\text{eq}})$ and $\eta_{\text{act,ae}} = (\phi_{\text{ae}} - \phi_{\text{elyt}}) - (\phi_{\text{ae}}^{\text{eq}} - \phi_{\text{elyt}}^{\text{eq}})$. The well-known semi-empirical Butler-Volmer (B-V) equation is used to correlate η_{act} with the current density i at each electrode-electrolyte interface. The general form is given as

$$i = i_0 \left[\exp\left(\frac{n_{e,r}\beta_a F \eta_{\text{act,fe/ae}}}{RT}\right) - \exp\left(-\frac{n_e \beta_c F \eta_{\text{act,fe/ae}}}{RT}\right) \right] \quad (2.22)$$

Here, the subscripts a and c represent the anodic direction (producing e^-) and cathodic direction (consuming e^-) of a charge transfer reaction respectively. β_a and β_c are charge-transfer coefficients in the anodic and cathodic directions and signify the portion of the total electric potential ($F(\phi_{\text{ae/fe}} - \phi_{\text{elyt}})$) acting as the barrier for an electron jump in either direction [75,76]. Ergo, $\beta_a + \beta_c = 1$.

When the cell is running in electrolysis mode, for example when investigating co-electrolysis in Chapter 3, the second exponential term in Eq. 2.22 represents the electrochemical reduction of H_2O and CO_2 in the fuel electrode while the first exponential term represents O_2 production in the air electrode. To catalyze these reactions and drive them from equilibrium in this desired direction, η_{fe} must become more negative and η_{ae} more positive. Since $\phi_{\text{ae}} > \phi_{\text{elyt}} > \phi_{\text{fe}}$, ϕ_{ae} must increase relative to ϕ_{elyt} while ϕ_{fe} must decrease, assuming ϕ_{elyt} is held constant at its equilibrium value. Therefore, increasing

$E_{\text{cell}} = \phi_{\text{ae}} - \phi_{\text{fe}}$ above the equilibrium value $E_{\text{rev}} = \phi_{\text{ae}}^{\text{eq}} - \phi_{\text{fe}}^{\text{eq}}$ ‘activates’ and drives the electrolysis set of reactions forward leading to faster kinetics at higher E_{cell} values. Similarly, in fuel cell mode, decreasing E_{cell} below E_{rev} drives the reactions in the reverse direction resulting in faster kinetics at lower E_{cell} values.

The exchange current density, i_0 in Eq. 2.22, is a lumped parameter that accounts for the thermal part of the chemical potential of the reacting species, including the pre-factor, the thermal activation barrier and the reaction orders of the reacting species. The area of the three-phase boundary, i.e. the interface between the gas, electronic, and ionic phases where electrochemical reactions predominantly occur in composite electrodes, is also lumped into i_0 . The exact form of i_0 is specific to the reaction system studied and is defined in Chapter 3 for the co-electrolysis reaction system.

2.3 Energy Conservation

2.3.1 Bulk gas phase

Heat transport in the gas channels is one-dimensional along the flow direction and solely due to forced convection. In a single planar RU, the fluid temperature is evaluated as

$$\begin{aligned} \frac{\partial(\rho_g C_{p,g} T_g)}{\partial t} = & - \frac{\partial(u \rho_g C_{p,g} T_g)}{\partial z} + \frac{1}{t_{\text{ch}}} h_{\text{conv}}(T_{\text{ede}} - T_g) \\ & + \frac{1}{t_{\text{ch}}} h_{\text{conv}}(T_{\text{ic}} - T_g) \end{aligned} \quad (2.23)$$

where, $C_{p,g}$ is the specific heat capacity of the gas stream and T_g , T_{ede} and T_{ic} are the local gas, electrode and interconnect temperatures. The first term on the right-hand side represents the heat transported by the gas downstream via convection whilst the second and third terms account for the heat exchange with the electrode and the interconnect via convection.

For a stack, the energy conservation equation is identical to Eq. 2.23 except that the two exchange terms are lumped into one,

$$\frac{\partial(\rho_g C_{p,g} T_g)}{\partial t} = - \frac{\partial(u \rho_g C_{p,g} T_g)}{\partial z} + \frac{4}{d_h} h_{\text{conv}}(T_{\text{stack,s}} - T_g) \quad (2.24)$$

Here, $T_{\text{stack},s}$ is the local temperature of the solid phase of the stack. The factor $\frac{4}{d_h}$ arising from the integration over the finite volume is due to heat exchange between the gas and the electrode and interconnect surfaces. The hydraulic diameter d_h is defined as [77]

$$d_h = \frac{2w_{\text{ch}}t_{\text{ch}}}{(w_{\text{ch}} + t_{\text{ch}})} \quad (2.25)$$

where, w_{ch} is the width of the channel.

The convective heat transfer coefficient in Eqs. 2.23 and 2.24 is given as

$$h_{\text{conv}} = \frac{Nu\lambda_g}{d_h} \quad (2.26)$$

Here, λ_g is the thermal conductivity of the gas and the Nusselt number Nu is evaluated from an empirical correlation for fully developed laminar flow in catalytic monolith channels [78]. The correlation, a function of the Graetz number Gz , considers an entrance region with a thermal boundary layer before converging to a constant value down the length of the channel,

$$Nu = 3.095 + 8.933 \left(\frac{1000}{Gz} \right)^{-0.5386} \exp \left(-\frac{6.7275}{Gz} \right) \quad (2.27)$$

and,

$$Gz = \frac{d_h}{z} RePr \quad (2.28)$$

where, z is the axial position and Pr is the Prandtl number.

2.3.2 Solid phase of a single Planar Repeating Unit

The heat transport equation in the solid components of a single planar RU is solved in both the axial direction and along the thickness of the RU. The energy conservation equation is formulated by accounting for all three principle modes of heat transfer, namely, conduction, convection, and radiation. Heat sinks/sources due to the endothermic/exothermic electrochemical reactions at the electrode-electrolyte interface \dot{Q}_{echem} , the heterogeneous surface chemistry in the fuel electrode \dot{Q}_{hchem} and Joule heating due to irreversibilities such as the ohmic and activation overpotentials are also included.

In the porous electrodes,

$$\begin{aligned}
\rho_{\text{ede},s} C_{p,\text{ede}}^e \frac{\partial T_{\text{ede}}}{\partial t} &= \frac{\partial}{\partial y} \left(\lambda_{\text{ede}}^e \frac{\partial T_{\text{ede}}}{\partial y} \right) + \frac{\partial}{\partial z} \left(\lambda_{\text{ede}}^e \frac{\partial T_{\text{ede}}}{\partial z} \right) + \frac{i^2}{\sigma_{\text{ede}}^e} \\
&+ \begin{cases} \dot{Q}_{\text{hchem}}, & \text{within the fuel electrode} \\ 0, & \text{within the air electrode} \end{cases}
\end{aligned} \tag{2.29}$$

where $\rho_{\text{ede},s}$ is the density of the solid phase of the electrode, $C_{p,\text{ede}}^e$ and λ_{ede}^e are the effective specific heat capacity and effective thermal conductivity of the porous electrode. The first two terms on the right-hand side represent the two-dimensional heat conduction through the porous electrode whilst the third term is the Joule heating due to current conduction through the electrode. The final term is defined as

$$\dot{Q}_{\text{hchem}} = - \sum_{k=1}^{K_g} H_k \dot{S}_k A_{\text{gas}/\text{ede}}^V \tag{2.30}$$

where H_k is the molar enthalpy of k . Additional heat source terms are added to the right-hand side of Eq. 2.29 at the boundaries of the electrodes in the y -direction. At the electrode-electrolyte interface, they are $\frac{\dot{Q}_{\text{echem}}}{\partial y}$ and $\frac{\dot{Q}_{\text{act}}}{\partial y}$ while at the electrode-channel/interconnect rib interface, they are $\frac{\dot{Q}_{\text{contact}}}{\partial y}$, $\frac{\dot{Q}_{\text{conv}}}{\partial y} \left(\frac{w_{\text{ch}}}{w_{\text{RU}}} \right)$ and $-\frac{\dot{Q}_{\text{rad}}}{\partial y} \left(\frac{1}{w_{\text{RU}}} \right)$. The factors $\left(\frac{w_{\text{ch}}}{w_{\text{RU}}} \right)$ and $\left(\frac{1}{w_{\text{RU}}} \right)$ which result from the integration of the heat fluxes $\dot{Q}_{\text{conv}} = h_{\text{conv}}(T_g - T_{\text{ede}})$ and \dot{Q}_{rad} over the finite-volume are a product of the varying geometries of the components and heat transfer areas (see Fig. 2.1(b) at the beginning of this chapter).

The electrochemical heat source/sink \dot{Q}_{echem} is the reversible heat due to the reaction entropy ΔS ,

$$\dot{Q}_{\text{echem}} = - \frac{i}{n_{e,r} F} T \Delta S_r \tag{2.31}$$

whereas the Joule heat due to activation losses \dot{Q}_{act} and the contact resistance between the electrode and the interconnect rib \dot{Q}_{contact} are given by

$$\dot{Q}_{\text{act}} = i \left(\eta_{\text{act,fe}} + \eta_{\text{act,ae}} \right) \tag{2.32}$$

$$\dot{Q}_{\text{contact}} = i^2 R_{\text{contact}} \tag{2.33}$$

Since, solid oxide cells operate typically at temperatures between 973K-1123K, heat transfer due to radiation must be considered. Damm and Fedorov [79] have previously shown that radiation within the MEA is negligible. Therefore, only surface-to-surface radiation between the electrodes and interconnects is modeled,

$$\dot{Q}_{\text{rad}} = \frac{\sigma_{SB}(T_{\text{ede}}^4 - T_{\text{ic}}^4)}{R_{\text{rad,ede}\rightarrow\text{ic}}} \quad (2.34)$$

Here, SBC is the Stefan-Boltzmann constant and $R_{\text{rad,ede}\rightarrow\text{ic}}$ is the thermal resistance to radiation and is a function of the areas of the electrode, interconnect and interconnect ribs participating in radiation exchange, the view factors between these areas $F_{\text{ede}\rightarrow\text{ic}}$ and their total emissivities ϵ_{rad} ,

$$R_{\text{rad,ede}\rightarrow\text{ic}} = \frac{1 - \epsilon_{\text{rad,ede}}}{\epsilon_{\text{rad,ede}}W_{\text{ch}}} + \frac{1}{F_{\text{ede}\rightarrow\text{ic}}W_{\text{ch}}} + \frac{1 - \epsilon_{\text{rad,ic}}}{\epsilon_{\text{rad,ic}}(W_{\text{ch}} + 2t_{\text{ch}})} \quad (2.35)$$

where, $F_{\text{ede}\rightarrow\text{ic}} = F_{\text{ede}\rightarrow\text{ic,plate}} + 2F_{\text{ede}\rightarrow\text{ic,rib}}$ and is calculated from analytical expressions for parallel and perpendicular planes of finite length.

In the dense electrolyte, the energy conservation equation is simply

$$\begin{aligned} \rho_{\text{elyt,b}}C_{\text{p,elyt,b}} \frac{\partial T_{\text{elyt}}}{\partial t} \\ = \frac{\partial}{\partial y} \left(\lambda_{\text{elyt,b}} \frac{\partial T_{\text{elyt}}}{\partial y} \right) + \frac{\partial}{\partial z} \left(\lambda_{\text{elyt,b}} \frac{\partial T_{\text{elyt}}}{\partial z} \right) + \frac{i^2}{\lambda_{\text{elyt,b}}} \end{aligned} \quad (2.36)$$

where $\rho_{\text{elyt,b}}$, $C_{\text{p,elyt,b}}$ and $\lambda_{\text{elyt,b}}$ are the bulk density, specific heat capacity and thermal conductivity of the electrolyte material.

Lastly, the temperature gradients in the fuel and air side interconnects are evaluated,

$$\rho_{\text{ic,b}}C_{\text{p,ic,b}} \frac{\partial T_{\text{ic}}}{\partial t} = \frac{\partial}{\partial y} \left(\lambda_{\text{ic,b}} \frac{\partial T_{\text{ic}}}{\partial y} \right) + \frac{\partial}{\partial z} \left(\lambda_{\text{ic,b}} \frac{\partial T_{\text{ic}}}{\partial z} \right) \quad (2.37)$$

Similar to the porous electrodes, two additional terms $h_{\text{conv}}(T_{\text{g}} - T_{\text{ic}}) \left(\frac{w_{\text{ch}}}{\text{vol}_{\text{ic}}} \right)$ and $\frac{\dot{Q}_{\text{rad}}}{\text{vol}_{\text{ic}}}$ enter as source terms in Eq. 2.37 at the interconnect-channel interface, where the volume per unit length of the interconnect is calculated as

$$\text{vol}_{\text{ic}} = (t_{\text{ic}} + t_{\text{ch}})w_{\text{RU}} - w_{\text{ch}}t_{\text{ch}} \quad (2.38)$$

2.3.3 Solid phase of a stack of Planar Repeating Units

The lumped approach to model all the solid (dense and porous) components of a stack of repeating units as a single phase has been previously reported to be a reasonable approach [80] and allows for its representation as a porous media with straight channels similar to a catalyst monolith (see Fig. 2.1(a) at the beginning of this chapter). Since the time-scale for heat transfer in the stack solid is now much larger than the time-scale for all the physics in a single RU, the stack solid phase temperature can be decoupled from the system of equations describing the RU, thereby improving both computational speed and stability [19,52].

The 3-D heat transport equation in the solid phase of the stack is formulated as

$$\begin{aligned}
 \rho_{\text{stack},s} C_{p,\text{stack}}^e \frac{\partial T_{\text{stack},s}}{\partial t} &= \nabla \cdot (\lambda_{\text{stack}}^e \nabla T_{\text{stack},s}) \\
 &+ \sum_{\text{ch} \in \text{air}, \text{fuel}} h_{\text{conv}} (T_g - T_{\text{stack},s}) \left(\frac{2(w_{\text{ch}} + t_{\text{ch}})}{w_{\text{RU}} t_{\text{RU}}} \right) + \frac{\dot{Q}_i}{t_{\text{RU}}} \\
 &+ \dot{Q}_{\text{hchem}} \left(\frac{t_{\text{fe}}}{t_{\text{RU}}} \right)
 \end{aligned} \tag{2.39}$$

where, $t_{\text{RU}} = t_{\text{ic}} + 2t_{\text{ch}} + t_{\text{ae}} + t_{\text{elyt}} + t_{\text{fe}}$ and \dot{Q}_i accounts for the net heat source/sink due to the endothermic/exothermic electrochemical reaction and the exothermic joule heating,

$$\dot{Q}_i = -i \left(E_{\text{cell}} + \frac{\Delta H_r}{n_{e,r} F} \right) \tag{2.40}$$

\dot{Q}_i is positive in fuel cell mode while in electrolysis mode, it is positive above the thermoneutral voltage and negative below it.

2.3.4 Boundary Conditions

With the heat fluxes due to external sources already specified at the boundaries of the various components for their corresponding energy conservation equations, the remaining boundary conditions deal with the spatial gradients due to conduction. For the single RU, heat flux continuity is enforced at the electrode-interconnect rib interfaces,

$$\lambda_{ede}^e w_{RU} \frac{\partial T_{ede}}{\partial y} = \left(\frac{1}{\lambda_{rib,b} w_{rib}} + \frac{1}{\lambda_{ic,b} w_{RU}} \right)^{-1} \frac{\partial T_{ic}}{\partial y} \quad (2.41)$$

and at the electrode-electrolyte interfaces

$$\lambda_{ede}^e \frac{\partial T_{ede}}{\partial y} = \lambda_{elyt,b} \frac{\partial T_{elyt}}{\partial y} \quad (2.42)$$

To implement adiabatic conditions, the heat flux is set to zero at the edges of the modeling domain in the y and z-directions.

For the stack model, a heat flux boundary condition, including convective and radiative heat exchange terms with the surroundings, was set at the edges of the 3-D modeling domain for the solid phase [52],

$$\lambda_{stack}^e \frac{\partial T_{stack,s}}{\partial y} = h_{surr} (T_{stack,s} - T_{surr}) + \epsilon_{rad} \sigma_{SB} (T_{stack,s}^4 - T_{surr}^4) \quad (2.43)$$

2.4 Effective Transport Properties

The continuum approximation when applied to porous media, implicitly assumes a homogeneous distribution of the solid and fluid phase over a finite volume. To model transport phenomena, effective properties for the porous media need to be found which are not only the functions of their bulk phase values but also of the fraction of a given phase in the finite volume i.e. porosity, and the heterogeneity of the actual microstructure of the porous media, i.e. tortuosity factor. For diffusion in the fluid phase, the ratio of the porosity and tortuosity factor is a good approximation of the influence of the porous media on the bulk diffusivities as described earlier in Eqs. 2.10 and 2.11. However, for charge transport in the solid phase, factors like the interconnectedness or percolation of the solid clusters must also be considered.

Bearing that in mind, Nam and Jeon [81] derived a relationship for the effective electrical conductivities for the composite porous electrodes,

$$\sigma_{ede}^e = \sum_{m \in \{el, io\}} \sigma_{m,b} [(1 - \epsilon) v_{f,s,m} \gamma_{s,m}]^{1.5} \quad (2.44)$$

where, $\sigma_{m,b}$ is the temperature-dependent bulk conductivity and $v_{f,s,m}$ is the volume fraction of the phase m (electronic or ionic) in the solid phase of the electrode. The percolation probability of phase m through the solid phase of the electrode $\gamma_{s,m}$ is a function

of the co-ordination number of particles of phase m , $Z_{m,m}$, and is given by a correlation developed by Bertei and Nicoletta [82],

$$\gamma_{s,m} = 1 - \left(\frac{4.236 - Z_{m,m}}{2.472} \right)^{3.7} \quad (2.45)$$

This correlation has been developed by non-linear least-square regression on simulated data of a random packing of spheres. As mentioned earlier, though there are limitations in assuming a packed bed of spheres to represent the real electrode microstructure, percolation theory does provide a better estimate of the effective transport properties than the oft-used Bruggeman correlation [83]. Percolation theory also accounts for sintering by defining a contact angle between neighboring particles to account for a region of overlap, thereby enabling the calculation of microstructural parameters like $A_{\text{gas/ede}}^V$ used in Eqs. 2.5, 2.6 and 2.30 and d_{pore} used in Eq. 2.10 [84].

For thermal transport, effective relationships between the bulk solid and fluid properties must be found to suitably represent the behavior of the porous electrodes. Since the bulk density of the gases is negligible compared to the solids, the bulk density of the solid phase is taken to be the density of the porous media. The effective specific heat capacity can be found by a simple parallel model weighted by the porosity,

$$C_{p,\text{ede}}^e = \epsilon C_{p,g} + (1 - \epsilon) C_{p,s} \quad (2.46)$$

However, the parallel model for the effective thermal conductivity is the theoretical maximum while the series model is the theoretical minimum. Thus, none of these models accurately depict reality. Thus, the geometric-mean model, which was found to be much more realistic for randomly structured porous media [85], was used,

$$\lambda_{\text{ede}}^e = \lambda_g^\epsilon \lambda_s^{1-\epsilon} \quad (2.47)$$

Since the solid phase of the electrodes is a composite, Eqs. 2.46 and 2.47 were also applied to evaluate the specific heat capacity and thermal conductivity of the composite from the bulk conductivities of its constituents. In this case, $v_{f,s,m}$ replaced ϵ in the equations.

The density and effective specific heat capacity of the lumped solid phase of the stack was also found by estimating the fractions of the stack volume occupied by each component and substituting it into the parallel model,

$$\rho_{\text{stack}}^e = \sum_q v_{f,\text{stack},q} \rho_q \quad (2.48)$$

$$C_{p,\text{stack}}^e = \sum_q v_{f,\text{stack},q} C_{p,q} \quad (2.49)$$

Here, $v_{f,\text{stack},q}$ is the volume fraction of component q in the stack.

The evaluation of the effective thermal conductivity for the stack solid is a bit more involved and requires the solution of two thermal resistance networks yielding separate λ_{stack}^e values for the radial and axial directions as depicted in Fig. 2.3 for the F-design stack. The two networks consist of a sequence of series and parallel thermal pathways and include both conduction through the solid components and radiative heat exchange between the electrodes and interconnects.

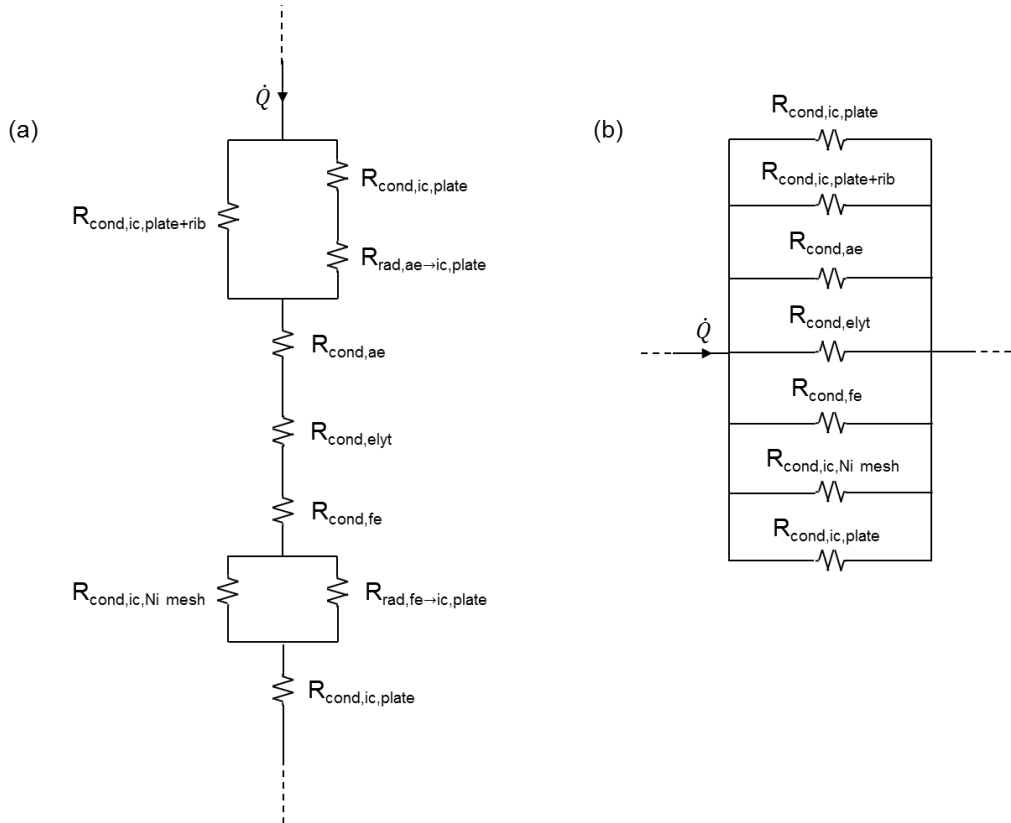


Figure 2.3. Thermal resistance networks across a repeating unit of the F-design stack in (a) radial, i.e. along the stack thickness and (b) axial directions.

Chapter 3

High Temperature Co-electrolysis – From Cells to Stacks⁵

To help understand the effects of scaling up, the work presented in this chapter adopts a hierarchical continuum modeling approach to analyze the performance of a solid oxide co-electrolysis stack. Initially, a transient isothermal model coupling 1-D gas transport through the porous electrodes' thickness to heterogeneous and electrochemical reactions is used to calibrate the electrochemical model against button cell experiments conducted by Fu et al. [46]. The measurements were made at operating temperatures of 1083.15K and 1133.15K and for two different reactant compositions – 10% H₂, 40%CO₂, 50%H₂O and 10% H₂, 30%CO₂, 60%H₂O. The commercially available ESC2 cell used by Fu consists of a dense Yttria Stabilized Zirconia (YSZ) electrolyte sandwiched between a porous Nickel-Gadolinium Doped Ceria (Ni-GDC) cermet fuel electrode and a porous Lanthanum Strontium Manganite-Yttria Stabilized Zirconia (LSM-YSZ) composite air electrode [46]. The calibrated kinetic model is then utilized to model a single repeating unit (RU) of a stack of Ni-GDC|YSZ|LSM-YSZ cells under co-flow and adiabatic conditions. The RU geometry is based on the fuel electrode-supported F-design planar cells developed by Forschungszentrum Jülich [47]. In addition to heat and mass transport along the thickness, the RU model also includes thermo-fluidic transport along the flow direction as well as accounting for the influence of the interconnects, the interconnect ribs, and the air and fuel electrode contact layers. Since, the molar ratio of the produced syngas is critical for its use in industrial applications, the RU's performance in producing two such H₂:CO ratios, namely 2:1 for methanol, DME and Fischer-Tropsch (F-T) synthesis [86], and 1.05:1 for hydroformylation [87], is mapped as a function of parameters such as cell length, inlet gas velocity, operating temperature and cell voltage. The capital costs accrued in scaling up

⁵ Parts of this section have been taken from A. Banerjee, Y. Wang, J. Diercks and O. Deutschmann, Hierarchical Modeling of Solid Oxide Cells and Stacks producing Syngas via H₂O/CO₂ Co-electrolysis for Industrial Applications, Appl. Energy 230 (2018) 996-1013.

from a single RU to stacks of RUs capable of producing a commercial yield of syngas is also analyzed. Finally, the RU model is coupled to a transient 3-D heat transfer model for the stack taking into account energy exchanged with the surroundings. On comparing the performance of the stack to the RU, the merits and de-merits of such a tiered approach to stack engineering and operation is discussed. Time constants for charge, mass and heat transport through the stack over a myriad of operating intervals are also evaluated.

3.1 Additional model details

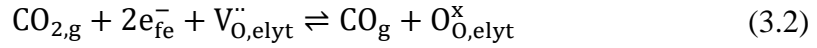
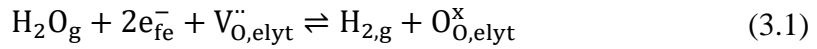
To facilitate a hierarchical modeling approach, a consistent set of model equations is required to simulate both a single cell and a stack of multiple cells performing co-electrolysis of steam and carbon dioxide. Thus, the following assumptions, in addition to those previously listed in Chapter 2, are made to make the system of mathematical equations tractable and computationally efficient on the scale of a stack,

1. The interfacial charge transfer model is employed. Thus, spatial distributions of the electronic and ionic phase potentials with respect to the electrode and electrolyte thickness are not evaluated. Menon et al. have already used the interfacial charge transfer model to reproduce the same experimental data set used to calibrate the electrochemical model in this study [20].
2. Modified Butler-Volmer type expressions informed by elementary step reaction mechanisms are used to formulate the kinetics of the charge transfer reactions at the electrode-electrolyte interfaces.
3. The heterogeneous thermochemical reactions on the Ni surface in the Ni-GDC fuel electrode are modeled using a detailed elementary step reaction mechanism. The kinetics are formulated using the mass-action law for each step and the chemical activities are evaluated using the mean-field approximation.

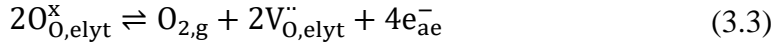
Keeping these assumptions in mind, the features added to the model for this study are discussed in the following sub-sections.

3.1.1 Electrochemistry

Both H₂O and CO₂ undergo reversible electrochemical reduction simultaneously during co-electrolysis. At the fuel electrode-electrolyte interface,



and at the air electrode-electrolyte interface,



Therefore, individual potential balances are constituted for the two parallel pathways,

$$E_{\text{cell}} = E_{\text{rev,H}_2\text{O}} + \eta_{\text{act,fe,H}_2\text{O}} + \eta_{\text{act,ae,H}_2\text{O}} + \eta_{\text{ohm,H}_2\text{O}} \quad (3.4)$$

$$E_{\text{cell}} = E_{\text{rev,CO}_2} + \eta_{\text{act,fe,CO}_2} + \eta_{\text{act,ae,CO}_2} + \eta_{\text{ohm,CO}_2} \quad (3.5)$$

Here, the subscripts H_2O and CO_2 denote the H_2O and CO_2 pathway respectively. The reversible potentials for each pathway are evaluated as

$$E_{\text{rev,H}_2\text{O}} = \frac{\Delta G_{\text{H}_2\text{O}}^0}{2F} + \frac{RT}{2F} \ln \left(\frac{p_{\text{H}_2,\text{fe/elyt}} p_{\text{O}_2,\text{ae/elyt}}^{1/2}}{p_{\text{H}_2\text{O,fe/elyt}}} \right) \quad (3.6)$$

$$E_{\text{rev,CO}_2} = \frac{\Delta G_{\text{CO}_2}^0}{2F} + \frac{RT}{2F} \ln \left(\frac{p_{\text{CO,fe/elyt}} p_{\text{O}_2,\text{ae/elyt}}^{1/2}}{p_{\text{CO}_2,\text{fe/elyt}}} \right) \quad (3.7)$$

The ohmic overpotentials due to the current densities in the H_2O and CO_2 pathways are evaluated by Eq. 2.21 in Chapter 2. A modified form of the Butler-Volmer (B-V) equation, derived by considering the rate-limiting step of elementary electrochemical reaction mechanisms for the H_2O [50] and CO_2 pathways [88], implicitly relates the activation overpotentials to the current density of their corresponding pathways,

$$i_{\text{H}_2\text{O}} = i_{0,\text{H}_2\text{O}} \left[\exp \left(\frac{(1 + \beta_a)F \eta_{\text{act,H}_2\text{O,fe}}}{RT} \right) - \exp \left(- \frac{\beta_c F \eta_{\text{act,H}_2\text{O,fe}}}{RT} \right) \right] \quad (3.8)$$

$$i_{\text{CO}_2} = i_{0,\text{CO}_2} \left[\exp \left(\frac{\beta_a F \eta_{\text{act,CO}_2,\text{fe}}}{RT} \right) - \exp \left(- \frac{(1 + \beta_c)F \eta_{\text{act,CO}_2,\text{fe}}}{RT} \right) \right] \quad (3.9)$$

$$i_{\text{O}_2} = i_{0,\text{O}_2} \left[\exp \left(\frac{\beta_a F \eta_{\text{act,ae}}}{RT} \right) - \exp \left(- \frac{\beta_c F \eta_{\text{act,ae}}}{RT} \right) \right] \quad (3.10)$$

The shift in the charge transfer coefficients in the anodic and cathodic branches of Eqs. 3.8 and 3.9 respectively, occurs due to the reduction of a mechanism with multiple charge transfer steps into a single step [50].

For H_2O reduction and oxygen production [50], i_0 is expressed as

$$i_{0,\text{H}_2\text{O}} = A_{\text{H}_2\text{O}} \exp\left(-\frac{E_{\text{H}_2\text{O}}}{RT}\right) \frac{(p_{\text{H}_2,\text{fe/elyt}}/p_{\text{H}_2}^*)^{1/4} (p_{\text{H}_2\text{O,fe/elyt}})^{3/4}}{1 + (p_{\text{H}_2,\text{fe/elyt}}/p_{\text{H}_2}^*)^{1/2}} \quad (3.11)$$

$$i_{0,\text{O}_2} = A_{\text{O}_2} \exp\left(-\frac{E_{\text{O}_2}}{RT}\right) \frac{(p_{\text{O}_2,\text{ae/elyt}}/p_{\text{O}_2}^*)^{1/4}}{1 + (p_{\text{O}_2,\text{ae/elyt}}/p_{\text{O}_2}^*)^{1/2}} \quad (3.12)$$

while for CO₂ reduction [88], it takes the form

$$i_{0,\text{CO}_2} = A_{\text{CO}_2} \exp\left(-\frac{E_{\text{CO}_2}}{RT}\right) \frac{(p_{\text{CO}_2,\text{fe/elyt}}/p_{\text{CO,fe/elyt}})^{1/4}}{1 + (p_{\text{CO,fe/elyt}}/p_{\text{CO}}^*) + (p_{\text{CO}_2,\text{fe/elyt}}/p_{\text{CO}_2}^*)} \quad (3.13)$$

Here, A_k and E_k constitute the Arrhenius-type temperature dependency of $i_{0,k}$ and are fitted to experimental data while the parameter p_k^* is obtained from the equilibrium constant for the adsorption-desorption of species k on the Ni surface [50,88]. The complex reaction orders of the reacting species in Eqs. 3.11-3.13 are a consequence of reducing the elementary reaction mechanisms to a single rate-limiting step.

With the current densities in the H₂O and CO₂ pathways evaluated, the overall current density can be calculated. Whilst, the most simple approach would be to simply sum the contribution of the two parallel pathways [16], it has been observed that their contributions to the overall current density is not equal [2,18,46,89,90]. Thus, a weighting factor w_{fac} needs to be introduced,

$$i = w_{\text{fac}} i_{\text{H}_2\text{O}} + (1 - w_{\text{fac}}) i_{\text{CO}_2} \quad (3.14)$$

Although constant values of w_{fac} based on experimentally measured data have been used in the literature [2,18], here w_{fac} is treated as a simple function of the relative availability of H₂O and CO₂ at the fuel electrode-electrolyte interface,

$$w_{\text{fac}} = \frac{X_{\text{H}_2\text{O,fe/elyt}}}{(X_{\text{H}_2\text{O,fe/elyt}} + X_{\text{CO}_2,\text{fe/elyt}})} \quad (3.15)$$

3.1.2 Heterogeneous chemistry

With the electrochemical reactions considered to be occurring only at the electrode-electrolyte interface, the reaction source term \dot{s}_k entering the mass balances equations in the finite volumes of the electrodes is either zero for the air electrode or is given by Eq. 3.16 for the fuel electrode,

$$\dot{s}_k = \sum_{i=1}^{K_r} (v''_{k,i} - v'_{k,i}) k_{f,i} \prod_{j=1}^{K_g+K_s} [X]_j^{v'_{j,i}} \quad (3.16)$$

Here, K_r is the total number of surface reactions, $v''_{k,i}$ and $v'_{k,i}$ are the stoichiometric coefficients of the species k in the i^{th} reaction on the product and reactant sides respectively, K_s is the total number of surface species adsorbed, $v'_{j,i}$ are the stoichiometric coefficients of all reactants j in the reaction i .

The forward reaction rate constant $k_{f,i}$ is evaluated from a heterogeneous reaction mechanism consisting of 42 elementary steps describing adsorption/desorption of gas phase H_2 , H_2O , CO , CO_2 , CH_4 and O_2 to/from the Ni surface, WGS/RWGS reactions, methanation steps, steam/dry reforming of methane, oxidation of C_1 species and formation of a carbon monolayer on the Ni surface [91]. The mechanism has been able to accurately reproduce different sets of experiments on steam reforming of CH_4 over the temperature range 900K – 1350K. A modified Arrhenius-type expression describes the forward rate constant of the i^{th} elementary step in the mechanism,

$$k_{f,i} = A_i T^{\kappa_i} \exp\left(-\frac{E_{a,i}}{RT}\right) \prod_{j=1}^{K_s} \exp\left(-\frac{\xi_{j,i} \theta_j}{RT}\right) \quad (3.17)$$

Here, A_i is the pre-exponential factor, κ_i introduces temperature dependency for the pre-factor, $E_{a,i}$ is the activation energy and $\xi_{j,i}$ is an additional dependency of surface coverage on activation energy to account for lateral interactions.

A key requirement of all reaction mechanisms is thermodynamic consistency. At equilibrium,

$$K_i = \frac{k_{f,i}}{k_{b,i}} = \exp\left(-\frac{\Delta G_i^0}{RT}\right) \quad (3.18)$$

Even though the reaction mechanism was formulated as a series of irreversible forward and backward steps, the pair of rate constants for the irreversible steps that constitute a reversible reaction satisfy Eq. 3.18 at equilibrium [91].

3.1.3 Performance Metrics

To characterize the performance of the solid oxide electrolyzer, suitable metrics for performance need to be defined. Here, the metrics chosen are overall efficiency η and net

syngas yield γ_{syn} .

The overall efficiency is defined simply as ratio of the total energy output to the total energy input. The energy output is essentially the total heat of combustion of the syngas produced whilst the energy input is the electrical power supplied to the cell as well as the sensible heat required to raise the temperature of the fuel and air streams from ambient to the specified inlet temperature,

$$\eta = \frac{(\dot{m}_{o,H_2} - \dot{m}_{i,H_2})LHV_{H_2} + (\dot{m}_{o,CO} - \dot{m}_{i,CO})LHV_{CO}}{w_{\text{RU}}E_{\text{cell}} \int_0^{L_{\text{RU}}} idz + \dot{m}_{i,\text{ach}} \int_{T_\infty}^{T_{i,\text{ach}}} C_{p,g,\text{ach}} dT + \dot{m}_{i,\text{fch}} \int_{T_\infty}^{T_{i,\text{fch}}} C_{p,g,\text{fch}} dT} \quad (3.19)$$

Here, \dot{m}_i and \dot{m}_o are the total mass flow rate of the gas streams at the inlet and outlet, and the subscripts ach and fch denote air and fuel channels respectively. The ambient temperature T_∞ is taken to be 298.15K and the lower heating values (LHV) of H₂ and CO is used. This definition of efficiency is identical to the one used by Luo et al. [2] and is intended to be a conservative one as depending on the end use, the higher heating values (HHV) of H₂ and CO can also be used. Moreover, the presence of an effective high temperature heat exchanger at the gas outlet, as is normally the case in practical applications, will also raise the overall efficiency.

The net syngas yield γ_{syn} is the ratio of the moles of syngas produced per mole of input H₂O and CO₂,

$$\gamma_{\text{syn}} = \frac{(X_{o,H_2} - X_{i,H_2}) + (X_{o,CO} - X_{i,CO})}{X_{i,H_2O} + X_{i,CO_2}} \quad (3.20)$$

The net syngas yield is perhaps a more useful metric than reactant conversion since it specifically focuses on the output gases of interest.

3.2 Computational Procedure

The model computes steady-state current density, velocity, concentration, surface coverage, and temperature profiles for an applied cell voltage and inlet temperature, velocity and gas composition at ambient pressure. The coupled continuity equations for mass, momentum, charge and energy described in Chapter 2, are solved in the button cell and the single planar RU by discretizing the modeling domain into 45 and 70 finite volume elements of equal size, Δy and Δz , in the y- and z-directions respectively. The spatial

derivatives in the governing equations for mass, momentum and energy are approximated as finite differences by the method of lines in each finite volume. Thereby, the partial differential equations in time and space are reduced to ordinary differential equations in time which are solved transiently using the semi-implicit solver LIMEX [92]. The algebraic equations for charge conservation coupled to the differential equations are solved using a non-linear damped Newton-iteration solver [51]. The conservation equations for mass and momentum, which are hyperbolic for the bulk gas phase and parabolic for the porous electrodes, form an iterative loop along with the charge balance equations. A space marching algorithm is adopted to solve the resulting system of differential-algebraic equations for the single planar RU where each axial element of the RU is solved to convergence and the next element is initialized with the solution of the previous converged element. This leads to an overall '1-D+1-D' or quasi-2D effect. The fully 2-D heat transport equation (parabolic in time but elliptical in space) wraps around this inner loop and the entire transient system attains steady-state after a few iterations, typically under 15 minutes on a quad-core processor.

The solution of the governing equations for the stack is similar to the solution of the RU, with the outer iterative loop now being replaced by the 3-D transient heat transport equation for the solid phase of the stack. Since, the stack consists of a large number of repeating units, the solution of each RU becomes the bottleneck in terms of computation time. Therefore, an algorithm was developed to choose a single RU from a cluster having the same or a very similar local temperature field and assume its performance to be representative of the entire cluster [52]. Although this measure helps reduce the computational cost significantly, depending on the boundary conditions and the size of the stack, the computational time required to attain steady-state can vary from a day to a week depending on the size and number of cells in the stack.

The computer program describing the button cell, single planar RU and stack model is written in FORTRAN and is a part of the software package DETCHEM [93].

Since the goal of this study is to investigate the performance of the RU, and ultimately the stack, for two specified H₂:CO ratios, the inlet fuel composition must be adjusted and the entire solution procedure for each configuration repeated till the desired output syngas ratio is attained. Depending on the initial guesses for the inlet feed composition, tens of

simulations may need to be run for one set of parameters. Subsequently, mapping the performance as a function of the applied voltage, inlet gas temperature, inlet gas velocity and cell length requires several hundreds of simulations. To do so with full 3-D stack simulations would result in quite a significant computational time and effort. Thus, the performance of a single RU is mapped first, and the stack is modeled only at certain selected operating points.

3.3 Results and Discussion

The geometries for the button cell and planar RU as well as the microstructural and electrochemical parameters required by the model are listed in Table 3.1. The RU width is estimated by considering the 80 cm² active area of the F-design cell [70] to be a square of sides 8.94 cm which is, in turn, comprised of 20 repeating units of 4.47 mm width. The interconnect rib width is set to half the channel width to keep concentration losses and contact resistances realistic [72–74]. The thermal properties of the porous composite electrodes listed in the table are the effective values of the solid phase after factoring in the porosity.

3.3.1 Comparison of model and experiment

Figure 3.1 shows the comparison between simulated and experimental polarization curves measured by Fu et al. [46] for two operating temperatures and two inlet fuel compositions. The two sets of curves agree very well over the entire range of conditions studied and the model is also able to accurately predict the experimental open-circuit voltage (OCV). Apart from the curve for $T=1133.15\text{K}$ in Fig. 3.1(a), the current density of the ESC2 cell was under -1 A cm^{-2} and the cell temperature increased by a mere 5K [46] thereby giving the isothermal approach of modeling the button cell credence. However, the isothermal approach may break down when trying to predict performance at limiting current densities of $\sim -2\text{ A cm}^{-2}$ where cell temperatures increase by up to 25K [46,90].

The parameters defining the temperature and reaction order dependency that have been tuned to reproduce the button cell measurements are listed in Table 3.2. The electrochemical model was calibrated to this set of experimental data since the operating conditions closely resembled the range of conditions to be used for the performance analysis of the RU and stack. The syngas ratios necessary for F-T synthesis and

TABLE 3.1. Input model parameters

Parameter	Value	Reference
<i>Button Cell – ESC2</i>		
Fuel electrode thickness	40 μm	[46]
Electrolyte thickness	90 μm	[46]
Air electrode thickness	40 μm	[46]
Inlet gas velocity	0.3 m s^{-1}	Estimate
<i>Planar RU – F-design</i>		
Fuel electrode thickness	1010 μm	[70]
Electrolyte thickness	10 μm	[70]
Air electrode (LSM-YSZ) layer thickness	15 μm	[70]
Air electrode (LSM) layer thickness	70 μm	[70]
Interconnect thickness	0.75 mm	[13]
Gas channel thickness	1 mm	Estimate
RU width	4.47 mm	Estimate
Gas channel width	2.98 mm	Estimate
Interconnect rib width	1.49 mm	Estimate
<i>General</i>		
Pressure	1 atm	[46]
Mole fraction of oxygen in air channel	0.211	[46]
Porosity	0.35	[20]
Particle diameter	2.5 μm	[20]
Ni volume fraction	0.5	Estimate
GDC volume fraction	0.5	Estimate
LSM volume fraction	0.5	Estimate
YSZ volume fraction	0.5	Estimate
Ni surface site density	$2.66 \times 10^{-9} \text{ mol cm}^{-2}$	[20]
<i>Material Properties</i>		
Electronic conductivity of Ni	$3.27 \times 10^4 - 10.653T$	[94]
Ionic conductivity of GDC	$(1.45 \times 10^5 / T) \cdot e^{-7818.1/T} \text{ S cm}^{-1}$	[42]
Density of porous Ni-GDC	5140.4 kg m^{-3}	[95,96]
Specific heat capacity of porous Ni-GDC	352.8	[97,98]
Thermal conductivity of porous Ni-GDC	4.0	[99,100]
Total emissivity of fuel electrode	0.5	Estimate
Ionic conductivity of YSZ	$3.34 \times 10^2 \cdot e^{-10300/T} \text{ S cm}^{-1}$	[101]
Density of YSZ	5938.0 kg m^{-3}	[102]
Specific heat capacity of YSZ	620.0	[103]
Thermal conductivity of YSZ	2.1	[103]
Electronic conductivity of LSM	$(8.885 \times 10^5 / T) \cdot e^{-1082.5/T} \text{ S cm}^{-1}$	[104]
Density of porous LSM-YSZ	3815.0 kg m^{-3}	[102,105]
Specific heat capacity of porous LSM-YSZ	398.0	[103,106]
Thermal conductivity of porous LSM-YSZ	3.5	[103,107]
Total emissivity of air electrode	0.8	Estimate
Density of Crofer 22 APU	7700.0 kg m^{-3}	[108]
Specific heat capacity of Crofer 22 APU	660.0	[108]
Thermal conductivity of Crofer 22 APU	24.0	[108]
Total emissivity of interconnect	0.3	Estimate
Ni mesh-Crofer 22 APU contact resistance	0.01 $\Omega\text{-cm}^2$	[108]
(La,Sr)CoO ₃ -Crofer 22 APU contact resistance	0.025 $\Omega\text{-cm}^2$	[108]

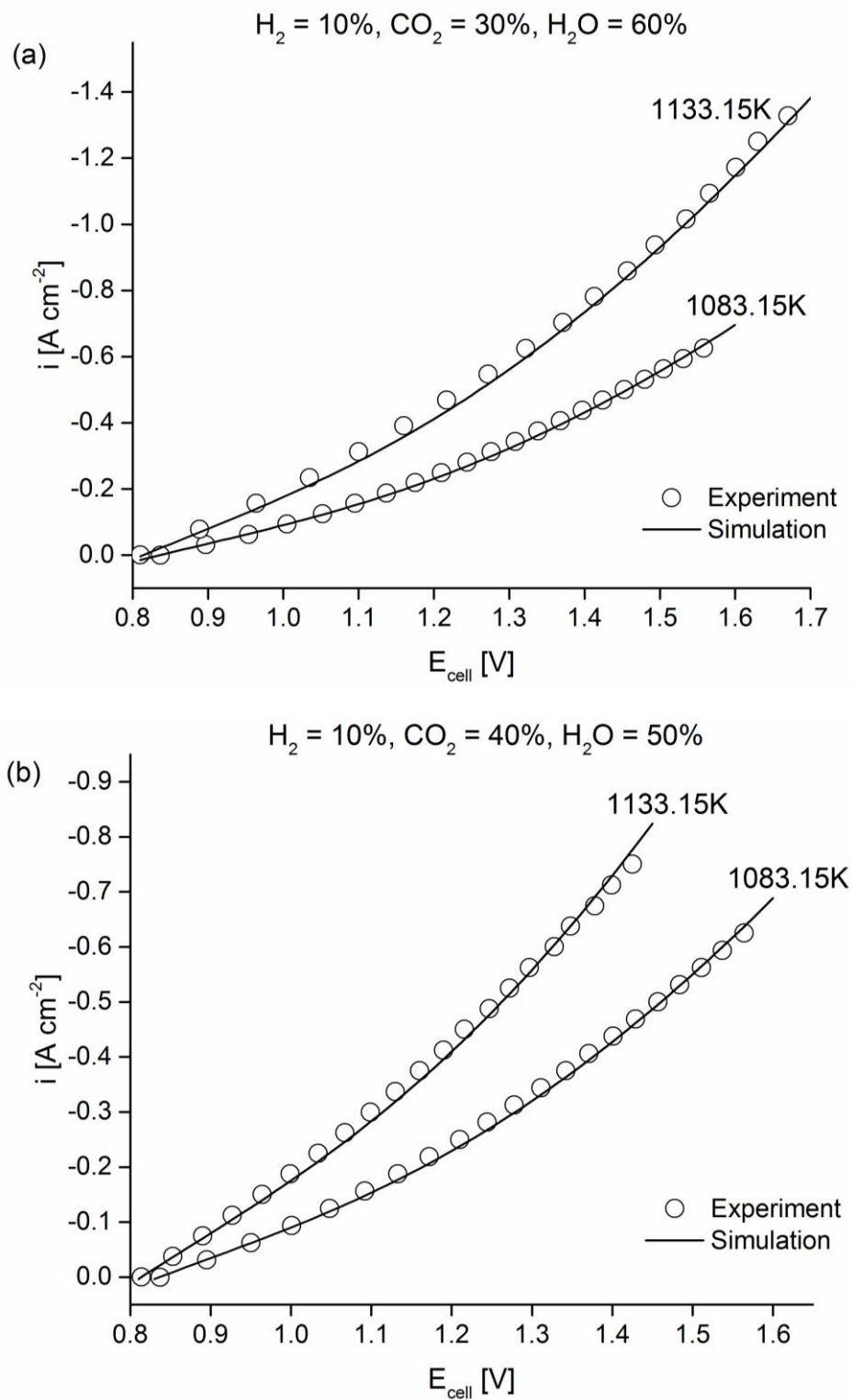


Figure 3.1. Steady-state polarization curves for simulation and experiment (Fu et al. [46]) at $T = 1083.15K$ and $T = 1133.15K$, fed with an fuel composition of (a) $X_{i,H_2} = 0.1, X_{i,CO_2} = 0.3, X_{i,H_2O} = 0.6$ and (b) $X_{i,H_2} = 0.1, X_{i,CO_2} = 0.4, X_{i,H_2O} = 0.5$.

TABLE 3.2. Electrochemical parameters for modified B-V model fitted to data from Fu et al. [46].

Fit Parameter	Value
$\text{H}_2\text{O}_g + 2e_{\text{fe}}^- + V_{\text{O,elyt}}'' \rightleftharpoons \text{H}_{2,g} + \text{O}_{\text{O,elyt}}^x$	
Pre-exponential Factor	$3.57 \times 10^6 \text{ A cm}^{-2}$
Activation Energy	$108.4 \times 10^3 \text{ J mol}^{-1}$
Anodic charge-transfer coefficient	0.7
$\text{CO}_{2,g} + 2e_{\text{fe}}^- + V_{\text{O,elyt}}'' \rightleftharpoons \text{CO}_g + \text{O}_{\text{O,elyt}}^x$	
Pre-exponential Factor	$1.48 \times 10^6 \text{ A cm}^{-2}$
Activation Energy	$131.38 \times 10^3 \text{ J mol}^{-1}$
Anodic charge-transfer coefficient	0.5
$2\text{O}_{\text{O,elyt}}^x \rightleftharpoons \text{O}_{2,g} + 2V_{\text{O,elyt}}'' + 4e_{\text{ae}}^-$	
Pre-exponential Factor	$1.06 \times 10^5 \text{ A cm}^{-2}$
Activation Energy	$122.5 \times 10^3 \text{ J mol}^{-1}$
Anodic charge-transfer coefficient	0.55

hydroformylation require ~30-50% of CO₂ in the feed and the 10% of inlet H₂ is necessary to prevent the oxidation of Ni in the Ni-GDC fuel electrode.

To test the thermal model and evaluate the differences between the ESC2 and F-design cells, the results from adiabatic simulations of single planar repeating units of both configurations are compared against syngas yield and temperature data for the single ESC2 cell [46] as illustrated in Fig. 3.2. At low-moderate voltages (~1.1V- 1.4V) the syngas yield of the ESC2 RU is only slightly lower than the measured values due to the additional contact resistance from the interconnects while the F-design RU yields more syngas than the measured ESC2 cell owing to its fuel electrode-supported geometry. Moreover, because of the smaller active area, the temperature of both repeating units is lower than the single cell measurements. The higher temperatures in the F-design RU as compared to the ESC2 RU is governed by the interplay between the heat adsorbed by the electrochemical reduction of H₂O and CO₂ and the ohmic heat released. The heat released/consumed due to thermochemistry on the Ni surface and the heat delivered by the input gases are 1-2 orders of magnitude lower than the afore-mentioned electrochemical heating terms. The ~1010 μm fuel electrode in the F-design RU, as compared to the ~40 μm fuel electrode in the ESC2 RU, affords a significantly larger reaction area which leads to higher current densities in the F-design RU between 1.1-1.4V. For example, at 1.36V, the length-averaged current density rises from ~-0.525 A cm⁻² in the ESC2 RU to ~-0.674 A cm⁻² in the F-design RU.

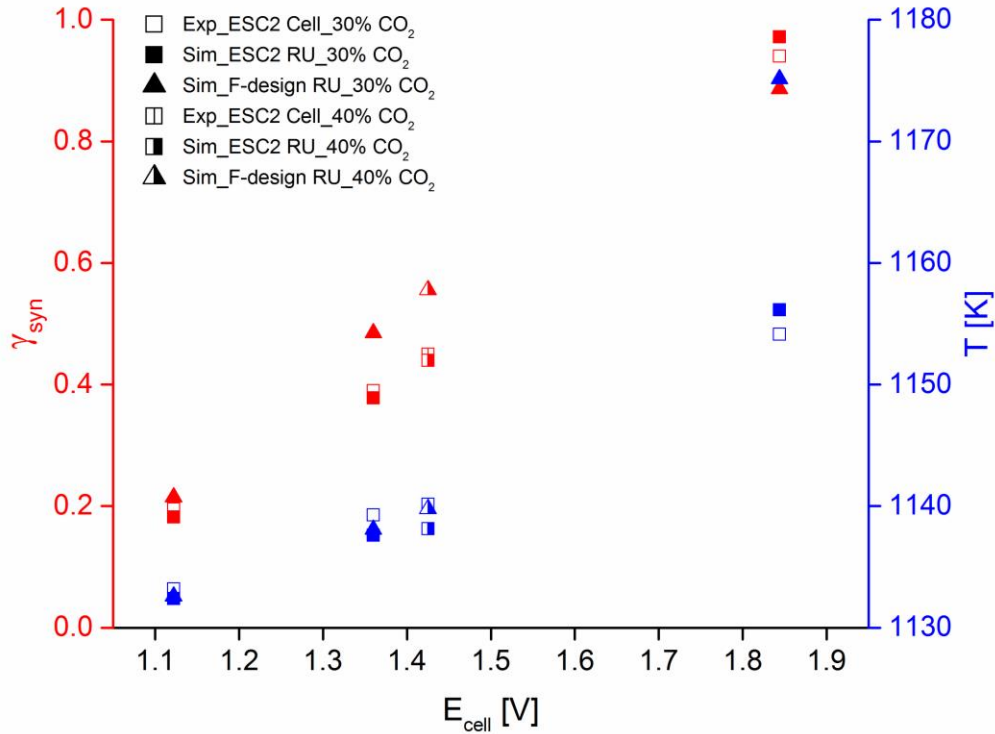


Figure 3.2. Syngas yield and cell temperature for simulation and experiment (Fu et al. [46]) at an inlet composition of 10% H₂, 30% or 40% CO₂ and balance H₂O.

However, at 1.844V the model slightly overestimates the performance of the ESC2 RU in contrast to the single cell while the F-design RU has a lower syngas yield due to diffusion limitations through the $\sim 1010 \mu\text{m}$ thick fuel electrode. The lower γ_{syn} also leads to the F-design RU being hotter despite its current density being limited to $\sim -1.23 \text{ A cm}^{-2}$ as compared to $\sim -1.375 \text{ A cm}^{-2}$ in the ESC2 RU. This is because the $\sim 99\%$ reactant conversion in the ESC2 RU leads to the heat consumed due to electrochemistry and the ohmic heating to be on the same order of magnitude whereas ohmic heating in the F-design RU is an order of magnitude larger than the electrochemical heat consumption due to a comparatively lower reactant conversion of $\sim 88\%$.

Figure 3.3 illustrates the species mole fraction profiles along the channel length and fuel electrode thickness. Looking at the H₂O profile in the fuel channel outlet, there is a slight increase during the first 3 mm for both configurations. This increase in X_{H_2O} is a result of the RWGS shift reaction on the Ni surface between the inlet CO₂ and H₂. However, as elucidated by the radial species profiles along the fuel electrode, the RWGS reaction is more dominant in the ESC2 RU since the RWGS reaction overlaps with the

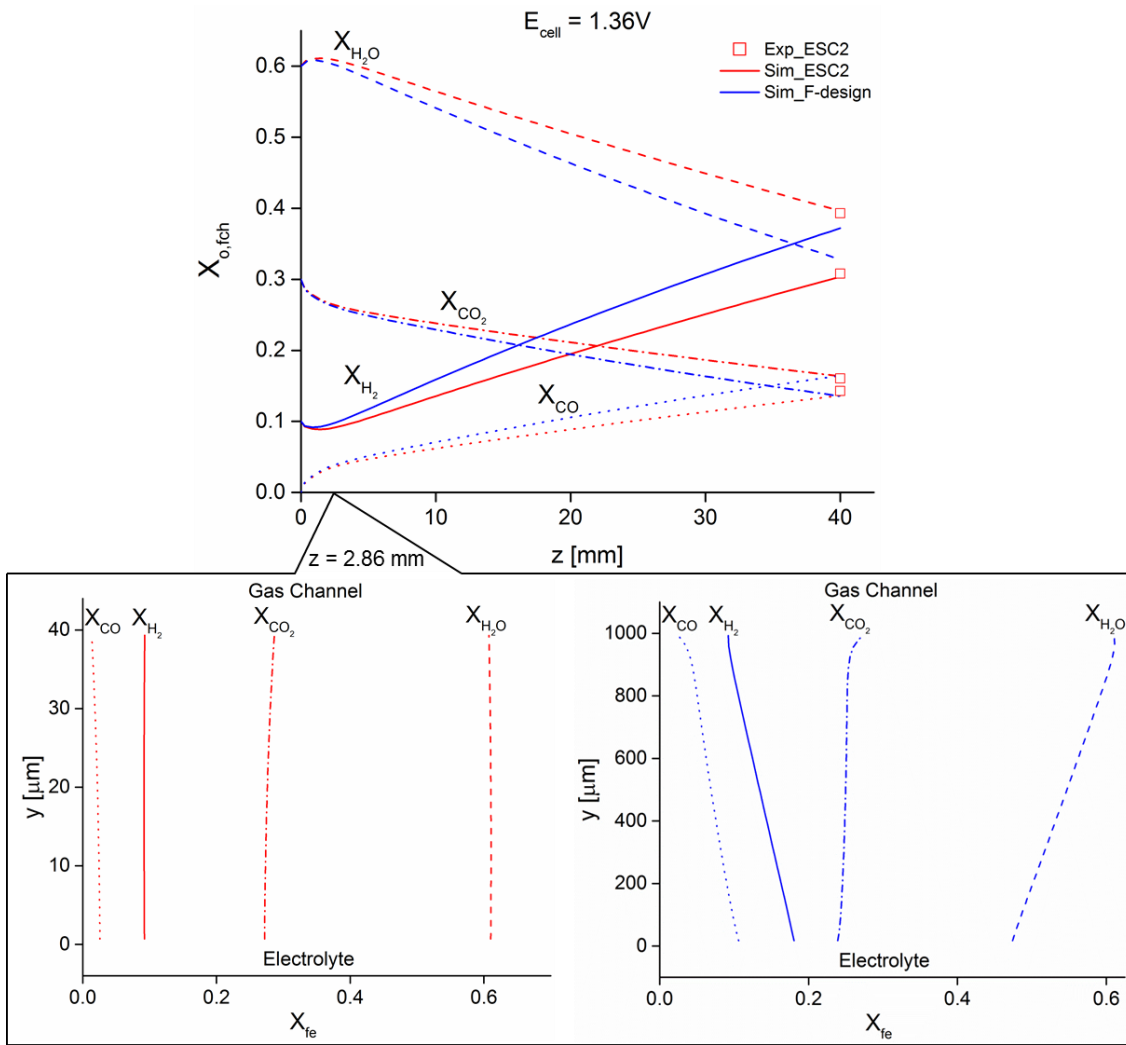


Figure 3.3. Mole fractions of H_2O , CO_2 , H_2 and CO as a function of the fuel channel axial position z and the fuel electrode radial position y . The open symbols are the outlet mole fractions measured by Fu et al. [46].

electrochemical reaction zones. For the thicker F-design fuel electrodes, the radial species profiles show that the RWGS reaction dominates over only a tiny zone ($\sim 100 \mu m$) near the gas channel interface with the rest of the electrode dominated by the electrochemical reactions. The predominance of the RWGS reaction at the RU inlet has been previously reported by Stoots et al. [109]. Despite the equilibrium being shifted in direction of the RWGS reaction throughout the entire length of the ESC2 and F-design repeating units (the ratio of the equilibrium constant to the reaction quotient is less than 1 throughout), it is overwhelmed by the electrochemical reduction of H_2O and CO_2 as evidenced by the

monotonic decrease in X_{H_2O} and X_{CO_2} and increase in X_{H_2} and X_{CO} along the length of the channel after the first 3 mm.

As shown in Fig. 3.3, the close agreement between the outlet gas composition for the simulated ESC2 RU and the measured ESC2 cell indicate that the relative contributions of the H_2O and CO_2 electrochemical pathways to the overall performance and the interplay between the charge transfer reactions and heterogeneous surface reactions on Ni are congruent with experiments.

3.3.2 Performance analysis of F-design RU

Having found the F-design RU to perform better than the ESC2 RU over the voltage range typically used to operate co-electrolysis cells and stacks (1.1V-1.4V), the performance of the F-design RU over this voltage range is analyzed for production of syngas ($H_2:CO$) in ratios of 2:1 for F-T synthesis and 1.05:1 for hydroformylation.

Figure 3.4 shows 3-D contour maps with the vertical axis denoting the RU efficiency and the color scale indicating total syngas yield over the RU length and inlet gas velocity horizontal parameter space. The maps encompass inlet gas temperatures of 1073.15K and 1123.15K and a voltage range of 1.1V-1.4V. For a single performance map at a given temperature and applied voltage, η and γ_{syn} are directly proportional to one another and to L_{RU} while being inversely proportional to u_i . The contours depicting isolines for η and γ_{syn} correspond to isolines for residence time of the reacting species in the RU i.e. L_{RU}/u_i . Due to the slow kinetics of the electrochemical and thermochemical reactions in the RU, increasing residence time by tweaking L_{RU} and u_i leads to an increase in η and γ_{syn} over the range of L_{RU} and u_i reported in the figure.

Increasing the applied voltage from 1.1V to 1.4V, in general, leads to an increase in η and γ_{syn} . At $T_{g,i}=1073.15K$ (see Fig. 3.4(a)), η and γ_{syn} are maximum at 1.4V, though the relative increase in peak efficiencies diminish with increasing voltages. The peak efficiencies at 1.3V and 1.4V are nearly identical. At $T_{g,i}=1123.15K$, the RU efficiency now attains a maximum at 1.3V as shown in Fig. 3.4(b). In fact, the peak efficiency at 1.2V is still higher than the peak efficiency at 1.4V despite the corresponding yield at 1.4V being ~1.8 times the yield at 1.2V. The shift of the peak efficiency maxima towards lower

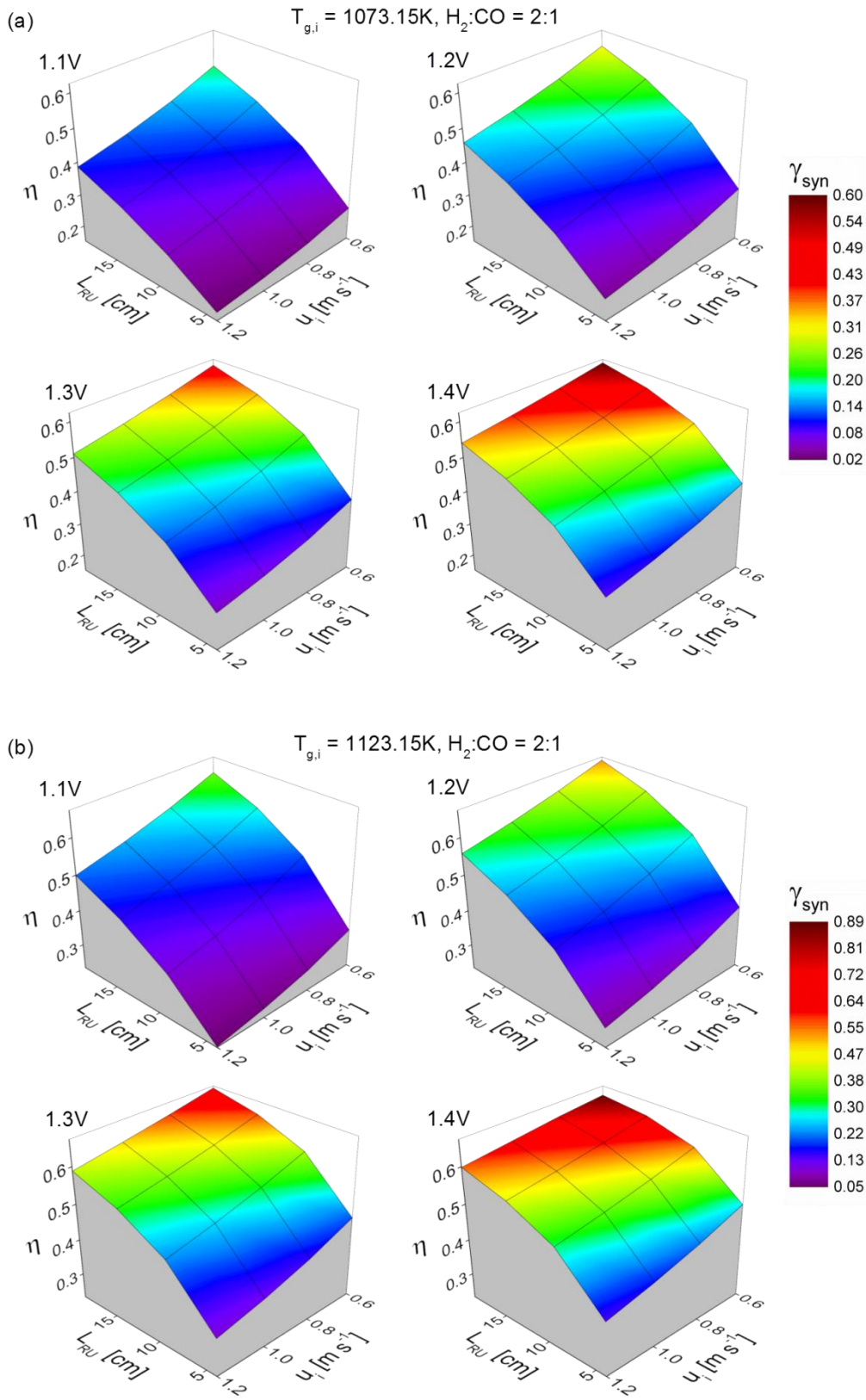


Figure 3.4. Performance maps of a F-design RU producing a $\text{H}_2:\text{CO}$ ratio of 2:1 over $E_{\text{cell}} = 1.1\text{V} - 1.4\text{V}$ at (a) $T_{g,i} = 1073.15\text{K}$ and (b) $T_{g,i} = 1123.15\text{K}$.

voltages with increasing heat input is a result of the thermodynamics of the electrochemistry governing the electrolyzer. Thermodynamically, the total electrical energy that needs to be supplied decreases with increasing temperature, even though the total heat required for the endothermic electrochemical reactions increases slightly [110]. This is one of the major advantages of high temperature electrolysis over low temperature electrolysis as cheap heat energy can be used to offset more expensive electrical energy as input [110], enabling cells to be operated at voltages below thermoneutral thereby preventing overheating and improving the reliability and lifetime of the electrolyzer. However, the significantly improved yields at higher voltages for both 1073.15K and 1123.15K illustrate the need to arrive at a compromise between the syngas yield required and the desired efficiency.

The interplay between efficiency and syngas yield is further highlighted by the performance maps of the F-design RU at inlet gas temperatures of 973.15K and 1023.15K depicted in Fig. 3.5. While both η and γ_{syn} decrease significantly overall with decreasing temperature and voltage, comparing the peak values for η and γ_{syn} for different voltages

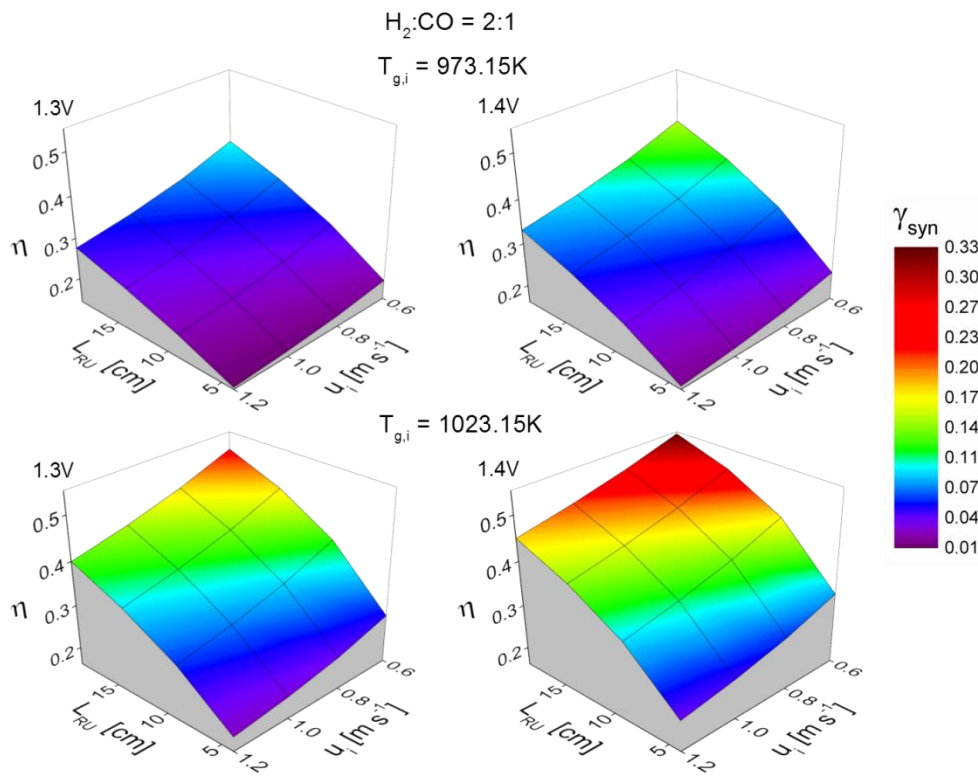


Figure 3.5. Performance maps of a F-design RU producing a $\text{H}_2:\text{CO}$ ratio of 2:1 for $E_{\text{cell}} = 1.3\text{V}$ and 1.4V and $T_{\text{g,i}} = 973.15\text{K}$ and 1023.15K .

and temperatures emphasize the increasingly dominant role of temperature over applied voltage. Increasing the cell voltage from 1.3V to 1.4V increases the peak RU efficiency by ~6 percentage points at $T_{g,i}=973.15\text{K}$ and only ~3 percentage points at $T_{g,i}=1023.15\text{K}$. However, for $E_{\text{cell}}=1.3\text{V}$, raising $T_{g,i}$ from 973.15K to 1023.15K improves the peak RU efficiency by ~14 percentage points. This trend is only amplified when looking at peak syngas yield. Increasing the operating temperature not only affects the thermodynamics but also drastically improves the kinetics of the reactions inside the electrolyzer.

In the same vein, the amount of CO_2 required in the feed to produce the 2:1 $\text{H}_2:\text{CO}$ syngas ratio decreases from ~44% to ~33% on increasing $T_{g,i}$ from 973.15K to 1123.15K. Since, the energy (and monetary) costs of capturing and feeding CO_2 to the electrolyzer is higher than feeding steam, the dependency of efficiency on temperature can be expected to be even higher than shown here. Thus, the benefits of using an external heat source such as waste heat from high-temperature industrial processes, nuclear power, renewable energy, etc. to raise the electrolyzer temperature is multitudinous.

Figure 3.6 depicts the performance of the F-design RU when producing syngas in the $\text{H}_2:\text{CO}$ ratio of 1.05:1 for hydroformylation. Essentially, changing the $\text{H}_2:\text{CO}$ ratio from 2:1 to 1.05:1 requires more CO_2 in the feed which in turn, operates the electrolyzer at a lower current density for a given applied voltage. The performance maps in the figure look virtually the same as the performance maps for the corresponding voltages in Fig. 3.4. This is a very important result as it underlines the ability of the electrolyzer to produce syngas in different $\text{H}_2:\text{CO}$ ratios under the same operating conditions with very similar performance. This syngas ratio flexibility gives SOECs a leg up on conventional gas-to-liquids syngas production methods like CPOX and SMR [8].

Though the syngas yields are lower due to the lower current densities and higher CO_2 in the inlet, the RU efficiencies for $\text{H}_2:\text{CO}$ ratio of 1.05:1 are slightly higher than the corresponding efficiencies for $\text{H}_2:\text{CO}$ ratio of 2:1. The improved efficiencies indicate that the WGS/RWGS reactions on the Ni surface help counteract the reduced electrochemical conversion of H_2O and CO_2 to an extent and mitigate a 1:1 decrease in syngas yield with decreasing electrical power input.

The change to a more CO enriched fuel output also impacts the coverages of the two

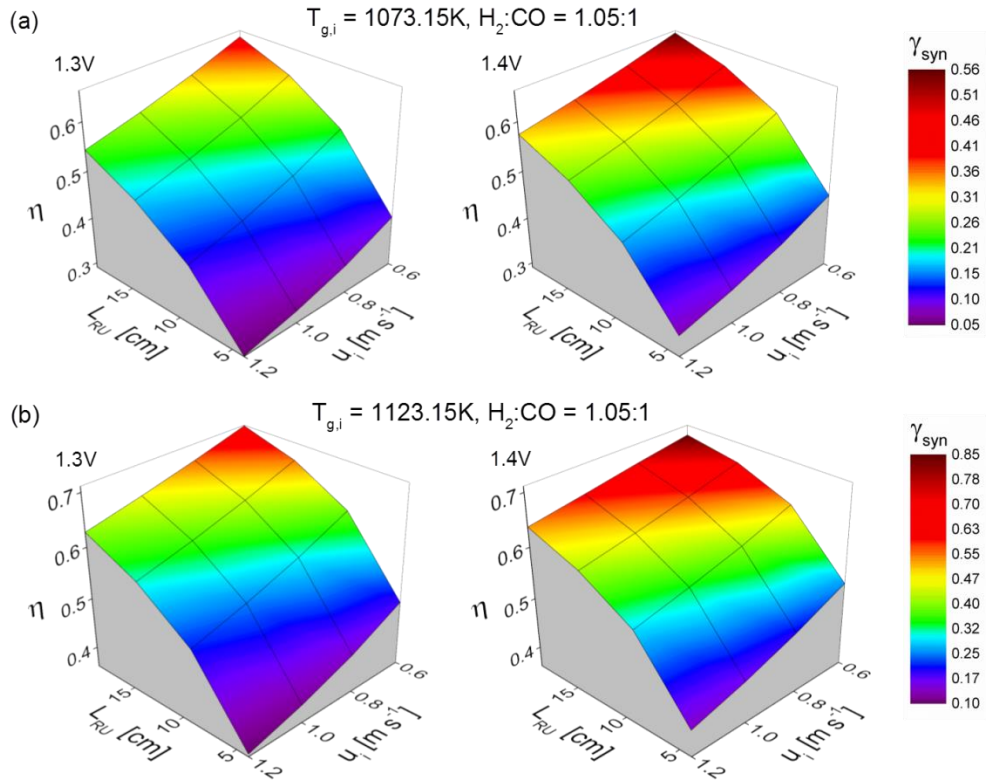


Figure 3.6. Performance maps of a F-design RU producing a H₂:CO ratio of 1.05:1 for $E_{\text{cell}} = 1.3\text{V}$ and 1.4V at (a) $T_{\text{g,i}} = 1073.15\text{K}$ and (b) 1123.15K .

dominant surface species on Nickel, i.e. H_s and CO_s. On switching from a desired output H₂:CO ratio of 2:1 to 1.05:1, the H_s coverage on Ni decreases from 0.15-0.2 to 0.1-0.15 while the CO_s coverage on Ni increases from 0.25-0.3 to 0.35-0.4 over the range of conditions studied. The C_s coverage on Ni also increases from $\sim 1\text{e-}8$ to $\sim 1\text{e-}6$ though the mechanism by Maier et al. [91] can only capture the formation of a single monolayer of elemental carbon on the Ni surface. A carbon activity factor, a_{C} , which indicates the thermodynamic favorability of the dissolution, oversaturation and inward growth of solid C on Ni is also evaluated [111]. Over the range of conditions studied in Figs. 3.4-3.6, a_{C} is less than 1 implying that the Ni surface is not susceptible to coking.

As mentioned earlier, in all the maps shown in Figs. 3.4-3.6, at a given voltage and temperature, the efficiency is directly proportional to syngas yield and in turn, the residence time. However, for the range of operating voltages and temperatures studied, SOCs are typically co-limited by reaction kinetics and reactant transport through the thick porous fuel electrodes [48]. Thus, it is expected that beyond a certain threshold value, the

efficiency will be inversely proportional to the residence time due to reactant starvation near the fuel electrode-electrolyte interface. This threshold residence time is evaluated with the help of Fig. 3.7. At $E_{\text{cell}}=1.3\text{V}$ and $T_{\text{g,i}}=1123.15\text{K}$, Fig. 3.7(a) shows that the RU efficiency decreases below inlet gas velocities of $\sim 0.2\text{ m s}^{-1}$ and $\sim 0.4\text{ m s}^{-1}$ for fixed RU lengths of 8.94 cm and 18.94 cm respectively. Conversely, Fig. 3.7(b) shows that increasing the RU length beyond $\sim 28.5\text{ cm}$ for an inlet gas velocity of 0.6 m s^{-1} also decreases the RU efficiency. Based on these results, a threshold residence time of $\sim 0.47\text{ s}$ can be evaluated. Though the syngas yield may increase beyond this threshold residence time as shown in the figure, the very high reactant conversion rates ($>96\%$) lead to the dearth of reactants in the RU and do not justify the additional electrical energy input required to convert them into product.

Along with η , γ_{syn} also decreases below 0.15 m s^{-1} for a RU length of 8.94 cm due to the production in parallel of $\sim 5\%$ methane. The faster methane production kinetics can be attributed to the increasing mole fractions of CO and H_2 ($\sim 33\%$ and $\sim 65\%$ respectively at $u_i \leq 0.15\text{ m s}^{-1}$) in the fuel electrode which leads to methanation on Ni in accordance with the mechanism by Maier et al [91]. Menon et al. [20] have shown via a reaction flow analysis that the primary pathway for methanation is the formation of elemental carbon from CO followed by hydrogenation of the surface carbon. However, they make note that Maier's mechanism has certain assumptions for the methanation steps that may not hold for SOCs, thus warranting further investigation. Additionally, operating at or above the threshold residence time increases the C coverage on Ni to $\sim 1\text{e-}5$ and makes the Ni surface more favorable to coking ($a_C > 1$). For a RU length of 8.94 cm, at $u_i = 0.2\text{ m s}^{-1}$, $a_C = 1.1$ while at $u_i = 0.1\text{ m s}^{-1}$, a_C increases to 19 near the fuel channel outlet assuring Ni coking [111].

The importance of long residence times for maximizing performance, especially reactant conversion, is obviously well-known to researchers, with inlet gas velocities in the range of 0.05 m s^{-1} to 0.4 m s^{-1} typically used to test lab-scale co-electrolysis cells and stacks [13,109,112]. However, these lab-scale electrolyzers must be scaled up to produce syngas in industrially relevant quantities, i.e. in the range 2500 kg day^{-1} - 7500 kg day^{-1} , that is required to operate commercial F-T synthesis plants [8].

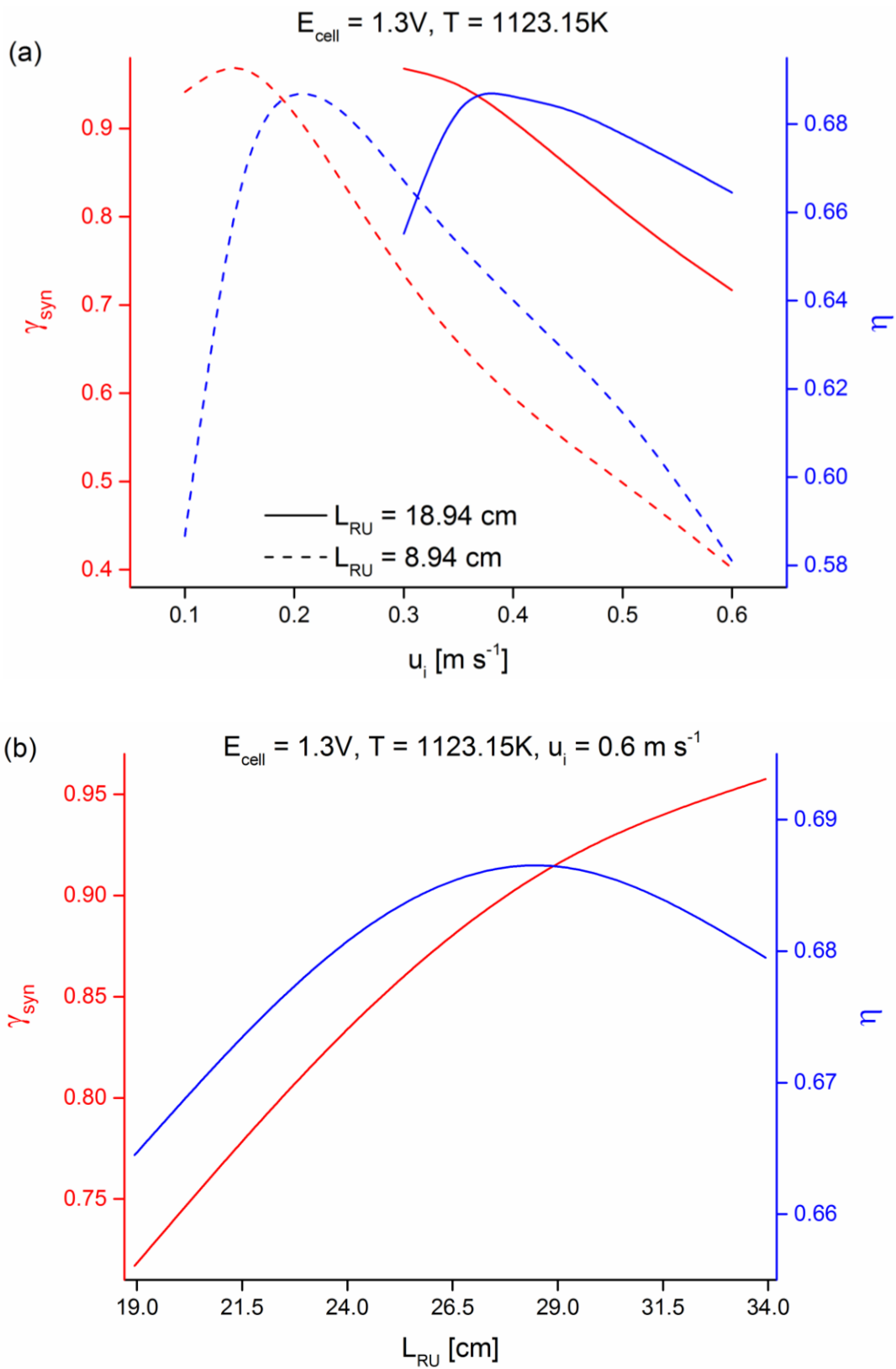


Figure 3.7. Efficiency and syngas yield of a F-design RU producing a $\text{H}_2:\text{CO}$ ratio of 2:1 as a function of (a) inlet gas velocity and (b) RU length for $E_{\text{cell}}=1.3\text{V}$ and $T_{\text{g,i}}=1123.15\text{K}$.

To help analyze the effects of such a scale up, a 3-D contour plot with the vertical axis representing the electrolyzer capital cost in Euros and the color bar denoting the total mass of syngas produced per day in the H₂:CO ratio of 2:1 by a single cell, i.e. 20 repeating units, \dot{m}_{syn} is shown in Fig. 3.8. The two quantities are plotted as a function of the RU length and inlet gas velocity horizontal parameter space for a fixed applied voltage of 1.3V and inlet gas temperature of 1123.15K. The electrolyzer capital cost is estimated by evaluating the active electrolyzer area required to produce 5000 kg day⁻¹ of syngas and by assuming a cost per active area of 1500€ m⁻² [21].

The isolines for \dot{m}_{syn} are directionally opposite to the corresponding isolines for η and γ_{syn} in Fig. 3.4(b). While Figs. 3.4-3.7 show that high values for η and γ_{syn} can be obtained by increasing the residence time, Fig. 3.8 shows that \dot{m}_{syn} is directly proportional to both L_{RU}

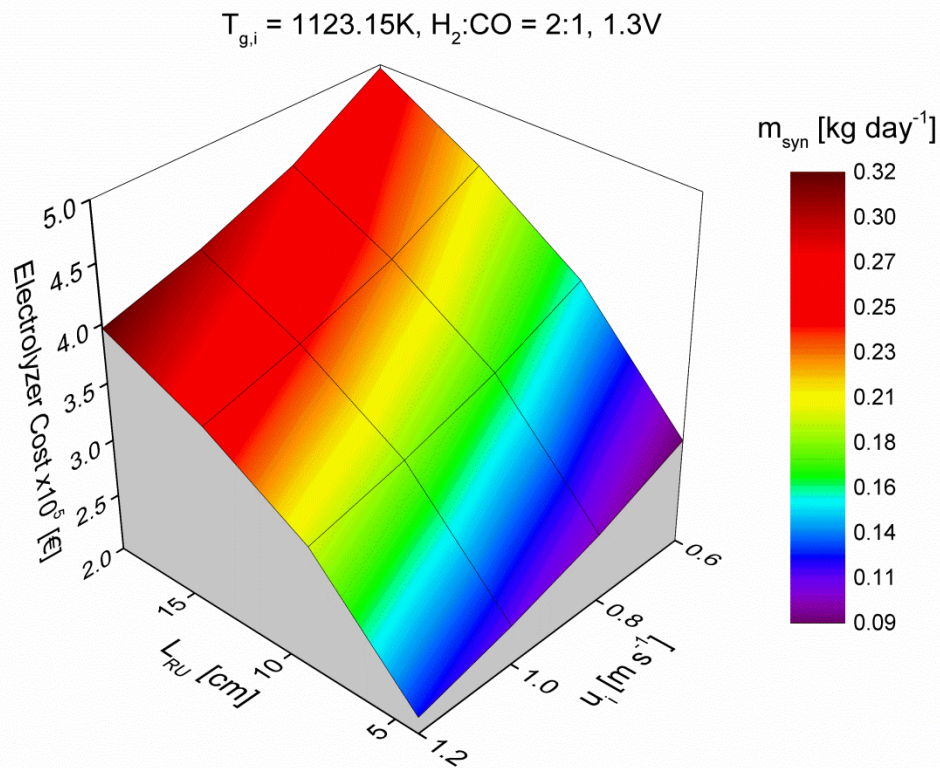


Figure 3.8. 3-D Contour map of the estimated F-design Electrolyzer capital cost and total mass of syngas produced per day in the H₂:CO ratio of 2:1 by a single cell (=20 RU) as a function of inlet gas velocity and RU length for $E_{\text{cell}} = 1.3\text{V}$ and $T_{\text{g,i}} = 1123.15\text{K}$. The capital cost is calculated based on the active electrolyzer area required to produce a commercially relevant quantity of 5000 kgs of syngas per day [21].

and u_i , i.e. a product of the residence time and the reactant flow rate. This is equivalent to the trade-off between cell efficiency and power density in SOFC mode. However, the electrolyzer size and cost follows a trend opposite to both \dot{m}_{syn} , and η and γ_{syn} since the lowest capital costs and smallest electrolyzer areas are attained with short repeating units and high gas velocities. As an example, on decreasing u_i from 1.2 m s^{-1} to 0.2 m s^{-1} , for a RU length of 8.94 cm the capital cost rises by $\sim 81\%$ from $\sim \text{€}307,000$ to $\sim \text{€}556,500$ (or, $\sim 205 \text{ m}^2$ to $\sim 371 \text{ m}^2$) whereas for a RU length of 18.94 cm, the capital cost increases by $\sim 50\%$ from $\sim \text{€}396,500$ to $\sim \text{€}595,300$ (or $\sim 264 \text{ m}^2$ to $\sim 397 \text{ m}^2$). This is because for any given inlet velocity, the peak current density is obtained within $\sim 3 \text{ mm}$ from the inlet after which, it monotonically decreases along the length of the stack in conjunction with reactant concentration.

Figure 3.7 has previously shown that high performance can be attained by simply adjusting the gas velocity to reach the threshold residence time for a given RU length. Thus, based on the capital cost trends, it seems reasonable to fabricate smaller repeating units and then adjust the gas velocity to a value which represents a reasonable compromise between capital cost and performance. Fu et al. [21] have previously reported the annual operational cost of the electrolyzer ($\sim 90\%$ of which is the cost of CO_2 and electricity) to be significantly larger than the capital cost. Thus, such a study would suggest operating the electrolyzer near the threshold residence time to be optimal provided there are no size constraints. This conclusion is further backed up by the analysis of temperature gradients across commercial scale stacks presented in the following sub-section.

3.3.3 Performance analysis of F-design stacks

Aside from electrolyzer cost and size, the effect of scaling up from cells to stacks on the reliability and lifetime of these devices also needs to be investigated. To that end, temperature gradients across medium and large stacks are evaluated since thermally induced failure modes are the major cause of shorter cell lifetimes [9]. Figures 3.9 and 3.10 show axial cut-away views of 3-D temperature profiles for F-design stacks with a length of 8.94 cm under different operating conditions. For both figures presented, the surrounding temperature is set equal to the inlet gas temperature in order to physically represent the common approach of testing stacks in a furnace with a set temperature.

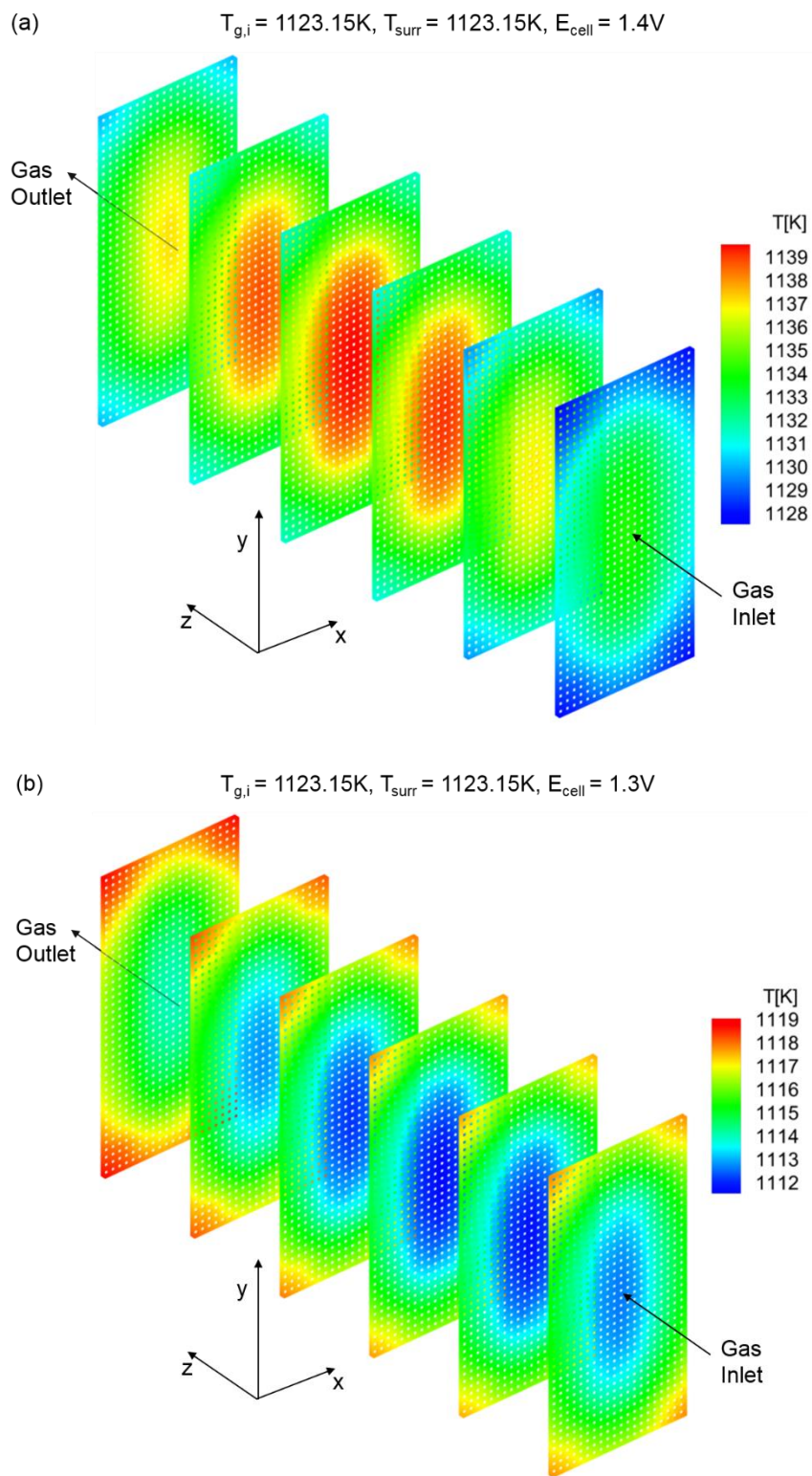


Figure 3.9. Axial cut-away views of 3-D temperature profiles for a 40-cell stack producing a $\text{H}_2:\text{CO}$ ratio of 2:1 with $L_{\text{RU}} = 8.94\text{ cm}$ and $u_i = 0.6\text{ m s}^{-1}$, operating at $T_{g,i} = T_{surr} = 1123.15\text{K}$ and (a) $E_{\text{cell}} = 1.4\text{V}$ and (b) $E_{\text{cell}} = 1.3\text{V}$.

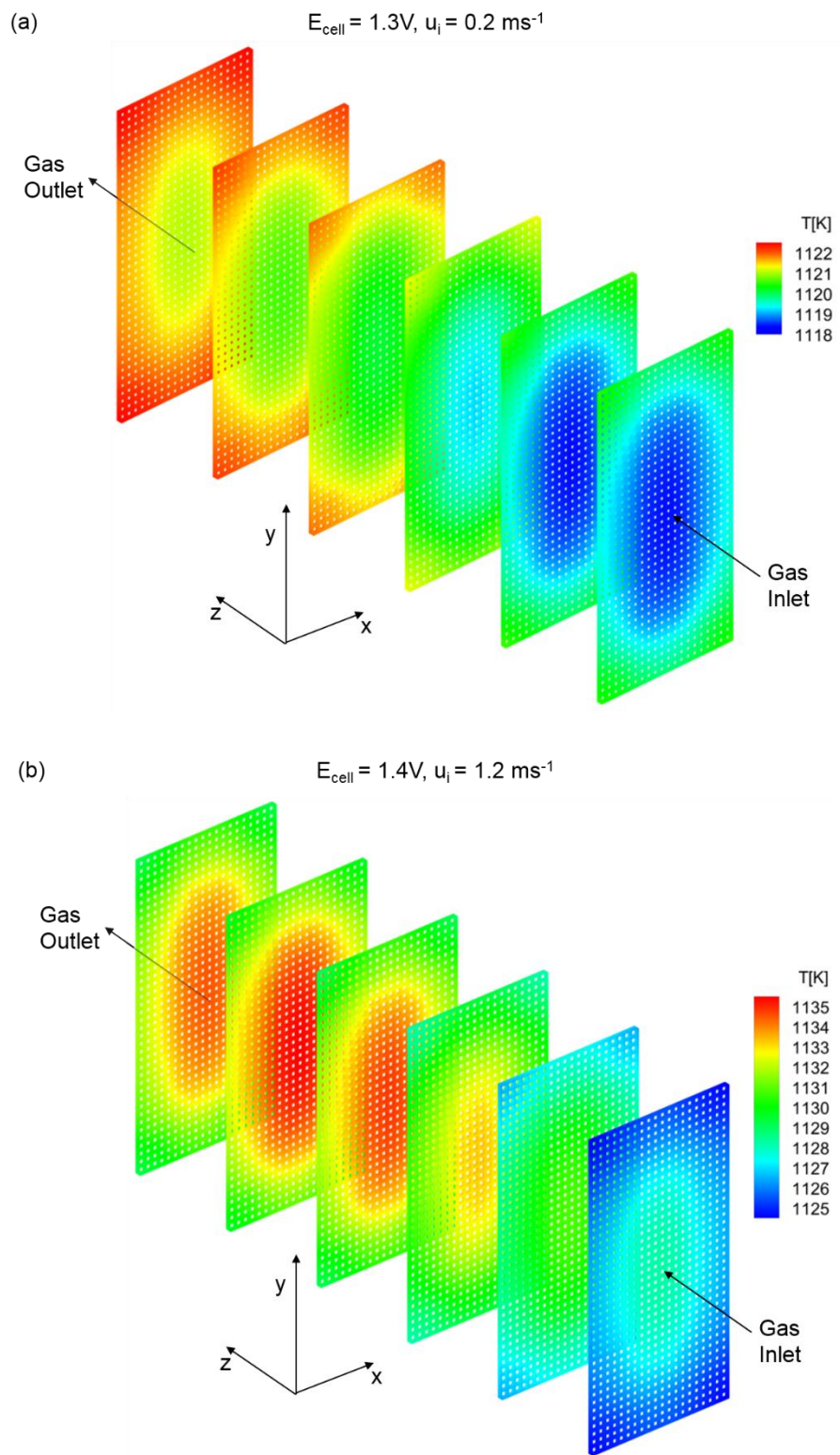


Figure 3.10. Axial cut-away view of 3-D temperature profile of a 40-cell stack producing a $\text{H}_2:\text{CO}$ ratio of 2:1 with $L_{\text{RU}} = 8.94\text{ cm}$, operating at $T_{\text{g,i}} = T_{\text{surr}} = 1123.15\text{K}$, and (a) $E_{\text{cell}} = 1.3\text{V}$ and $u_i = 0.2\text{ m s}^{-1}$ and (b) $E_{\text{cell}} = 1.4\text{V}$ and $u_i = 1.2\text{ m s}^{-1}$.

Figure 3.9 illustrates the impact of operating voltage and furnace temperature on the temperature profile for a 40-cell stack. When operating at 1.4V, above the thermoneutral voltage, the heat release due to joule heating, thermochemistry on Ni surface and the heat delivered to the stack by the input gases exceeds the heat required to drive the electrochemical reactions. As a result, the stack heats up to ~5K-16K above the set furnace temperature of 1123.15K (Fig. 3.9(a)). For every axial section, there is a central hot spot with heat flowing radially outward towards the corners of the stack. Conversely, on running the stack below thermoneutral at 1.3V, the heat release due to joule heating, Ni surface thermochemistry and heat delivered to the stack by the input gases are not sufficient to drive the electrochemical reactions. Ergo, the entire stack is colder than the set furnace temperature of 1123.15K by ~4K-11K (Fig. 3.9(b)). Heat now flows radially inward from the corners towards a central cold spot for each axial section. These results illustrate that cells at the stack corners perform differently vis-à-vis cells at the stack center. The area of the central hot/cold region also lends credence to the assumption of an isolated RU at the stack center to be effectively adiabatic.

Figure 3.10 illustrates the influence of inlet gas velocity and in turn, current density on stack temperature. On decreasing the inlet gas velocity from 0.6 m s⁻¹ to 0.2 m s⁻¹ to reach the threshold residence time and thereby maximize performance, the temperature profile flattens out over the 40-cell stack operating below thermoneutral at 1.3V as shown in Fig. 3.10(a). The slightly higher temperatures can be attributed to the much lower average current densities at $u_i = 0.2 \text{ m s}^{-1}$ (~0.365 A cm⁻²) as compared to $u_i = 0.6 \text{ m s}^{-1}$ (~0.467 A cm⁻²) due to the smaller volume of reactants processed by the electrolyzer. When running the stack above thermoneutral at 1.4V, Fig. 3.10(b) reveals that increasing u_i to 1.2 m s⁻¹ to reduce electrolyzer cost and size, also leads to slightly lower temperatures as compared to $u_i = 0.6 \text{ m s}^{-1}$. Despite a 9% increase in average current density at $u_i = 1.2 \text{ m s}^{-1}$ (~0.777 A cm⁻²) as compared to $u_i = 0.6 \text{ m s}^{-1}$ (~0.713 A cm⁻²), the increased fuel and air velocities sufficiently improve convective heat transfer between the fluid and solid phases of the stack to counteract the additional joule heating. This illustrates why one of the most common methods of stack temperature control is flowing excess air through the air channel. The movement of the central hot spot down the length of the stack on increasing u_i from 0.6 m s⁻¹ to 1.2 m s⁻¹ is indicative of the reduction in the relative decrease in current density over the 8.94 cm stack length (~35% for $u_i = 0.6 \text{ m s}^{-1}$ and ~17% for $u_i = 1.2 \text{ m s}^{-1}$).

Figure 3.11 evaluates the impact of scaling up from a single repeating unit to a stack on efficiency and syngas yield. To characterize stack performance, three representative repeating units are selected. The first RU is at the center, the second at the side and the third at the bottom corner of the stack. These three repeating units are enough to account for the various temperature localities across the stack cross-section. Based on the different conditions studied, the performance of the single RU is quite representative of the stack performance. For the 40-cell stack, the figure shows that the single RU provides a slightly conservative projection of stack performance at an operating voltage of 1.4V and a furnace temperature of 1123.15K while at 1.3V it marginally overpredicts the stack performance. Moreover, the performance at the stack side and corner improves as compared to the center with decreasing voltage since the stack center cools down (see Fig. 3.9).

3.3.4 Transient operation of F-design stacks

The results presented thus far report the steady-state performance of the F-design stack. Obviously, the transient model described in this study can also be used to simulate the dynamics of stack operation. The analysis of transients is of interest when the electrolyzer stack is integrated with the electric grid and can help identify strategies to ensure a constant stream of products and to minimize thermal transients leading to mechanical stress and strain.

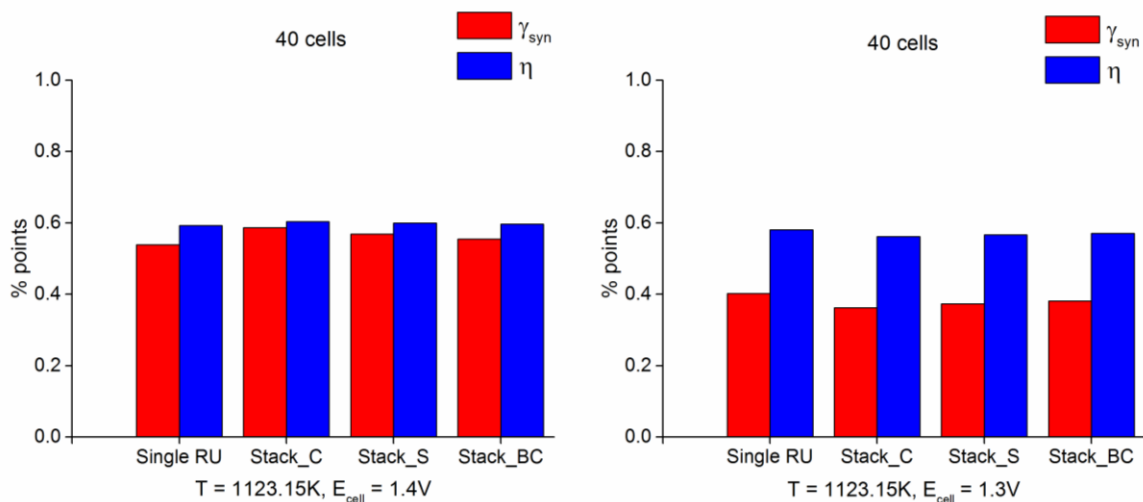


Figure 3.11. Efficiency and syngas yield ($H_2:CO = 2:1$) of a single repeating unit and three representative repeating units of a stack with a length of 8.94 cm and an inlet gas velocity of 0.6 m s^{-1} .

Figure 3.12 is a snapshot of various intervals of operation for an 80-cell stack with a length of 8.94 cm and an inlet gas velocity of 0.6 m s^{-1} . The multiple operating intervals include switching the stack between co-electrolysis, H_2O electrolysis and CO_2 electrolysis modes as well as step changes in voltage and inlet gas temperature. The current density and outlet gas composition of the RU at the stack center change rapidly at the beginning of each interval as evinced by a time constant τ_{const} (time taken to reach 90% of steady-state value) of $<1 \text{ s}$. After, they creep towards their steady state dictated by the slow response of the stack temperature ($\tau_{\text{const}} = \sim 800\text{-}900 \text{ s}$) as previously shown by Luo et al. for tubular cells [19].

On replacing the CO_2 in the inlet with Ar at 2050 s, in accordance with prior reports in the

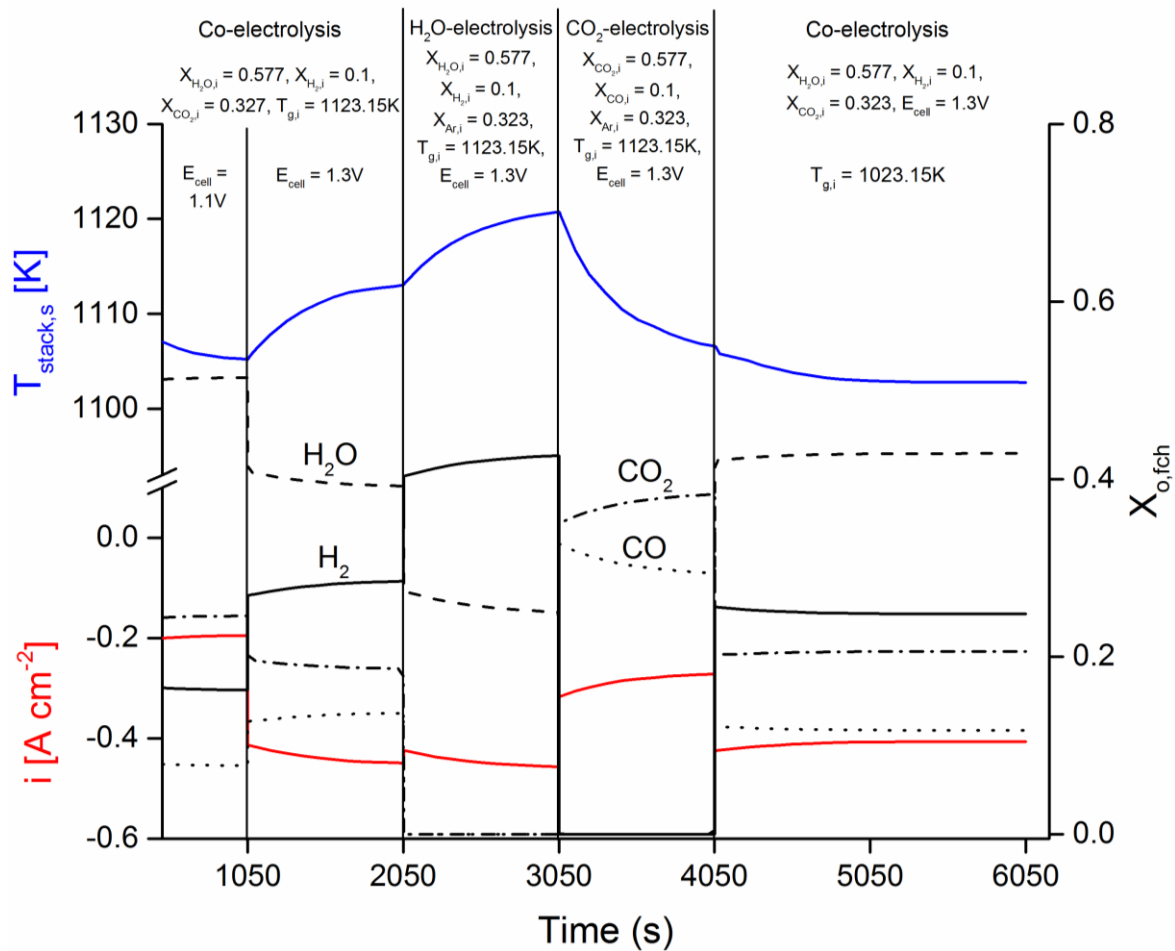


Figure 3.12. Mean stack temperature, and mean current density and outlet gas composition from RU at stack center for various operating intervals of an 80-cell stack with a length of 8.94 cm and an inlet gas velocity of 0.6 m s^{-1} .

literature [46,89], the current density decreases as the stack switches from co-electrolysis to pure steam electrolysis. The decrease in current density implies that the product yield is higher during co-electrolysis than pure steam electrolysis since CO_2 is converted into CO via a combination of the RWGS and electrochemical reduction reactions. Switching from steam electrolysis to pure CO_2 electrolysis at 3050 s reduces the current density by a factor of ~ 1.4 also in agreement with measurements for fuel-electrode supported cells [89]. The rise and fall in stack temperature when switching between co-electrolysis to steam electrolysis and subsequently to CO_2 electrolysis is because the operating voltage ($=1.3\text{V}$) is above the thermoneutral voltage for H_2O electrolysis but below the thermoneutral voltage for CO_2 electrolysis.

Although the snapshot exhibited is for less than a couple of hours of stack operation, it serves to demonstrate the capability of the model to simulate stack transients. Provided the model is coupled with ‘realistic’ mechanisms to capture long-term degradation, stack reliability and lifetime studies for operating intervals of 10,000-100,000 hrs or more could potentially be simulated, saving precious time and cost of experimental testing and vastly speeding up the stack design process. The bottleneck however, very clearly, is the development of such credible long-term degradation mechanisms.

Chapter 4

Elementary Kinetics of the Oxygen Reduction/Evolution Reaction on LSM-YSZ Composite Electrodes⁶

To help develop an intrinsic micro-kinetic mechanism for O₂ reduction/evolution on LSM-YSZ composites, the work presented in this chapter integrates ORR elementary kinetics into a fully transient continuum model of an LSM-YSZ half-cell. The half-cell consists of a porous LSM-8YSZ (8 mol% Ytria in Zirconia) composite air electrode sintered to a dense 8YSZ electrolyte. In addition to an elementary kinetic ORR model, the model also incorporates gas transport through the porous air electrode while charge transport through the MEA is modeled using the distributed charge transfer model. The coupled transport and kinetic model so developed is then used to simulate three separate experimental studies conducted by Barbucci et al. [43], Cronin et al. [44] and Nielsen and Hjelm [45] to ensure realistic kinetic and thermodynamic parameters for the ORR mechanism. The experimental data sets consist of transient electrochemical impedance spectra and steady-state Tafel plots measured over a temperature range of 873 K – 1173 K and an oxygen partial pressure (p_{O_2}) range of 0.05 atm – 1 atm. Three separate ORR mechanisms, each including parallel surface and bulk reaction pathways driven by three different electric phase potentials, are modeled to identify the mechanism which best describes the three sets of experiments. The rate limiting steps for each mechanism are also identified with the aid of a sensitivity analysis.

4.1 Micro-kinetic modeling of electrochemistry

The micro-kinetic elementary step approach has two important advantages over the more commonly used B-V approach. The first is that this approach makes no a priori assumption about the rate limiting step (RLS). The reaction can thus have a single RLS or be co-limited

⁶ Parts of this section are taken with permission from [49] A. Banerjee, O. Deutschmann, Elementary kinetics of the oxygen reduction reaction on LSM-YSZ composite cathodes, *J. Catal.* 346 (2017) 30-49.

by multiple RLSs. The second advantage is that the Nernst potential, valid only at thermodynamic equilibrium, is not required in the model formulation. This ensures a more accurate prediction of the open circuit voltage (OCV) for fuel cells operating with non-equilibrated gas mixtures, for e.g. when modeling DIR cells [67].

The incorporation of a detailed elementary step approach to modeling electrochemical reactions is facilitated by the following assumptions

1. The modeling domain (air electrode + electrolyte) is isothermal.
2. The principle of electroneutrality holds in the air electrode.
3. ORR is modeled by resolving the global reaction into a series of reversible steps involving reaction intermediates with each step being thermodynamically consistent and obeying the law of mass action. The chemical activities of the reacting species are set equal to their concentrations, which are evaluated using a mean-field approximation.
4. There are no reactions occurring at the current collector-air electrode and air electrode-electrolyte interfaces due to the small reactive area available in contrast to the reactive area of the porous air electrode composite matrix.
5. Direct oxygen adsorption on YSZ is not considered due to unfavorable kinetics relative to oxygen adsorption on LSM.

In light of these assumptions, the various facets of the micro-kinetic model are described in the following sub-sections.

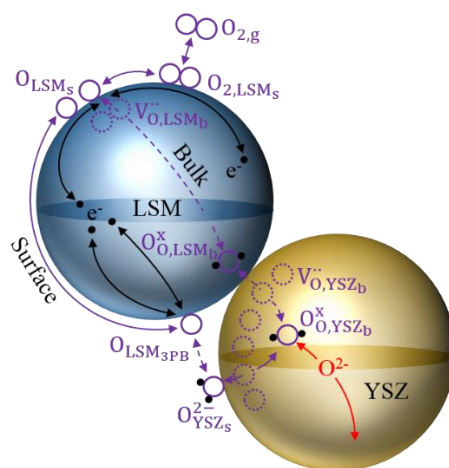
4.1.1 ORR mechanisms

Since the goal of this study is to develop a robust and intrinsic mechanism, a thorough investigation of the most pervasive ORR mechanisms in the SOC literature is essential. In this study, three such mechanisms are selected and illustrated in Fig. 4.1. When compared against experimental data, the impact (or lack thereof) of the various individual steps/intermediates posited by each mechanism on macroscopic parameters like current density and polarization resistance are elucidated. All of these mechanisms were postulated

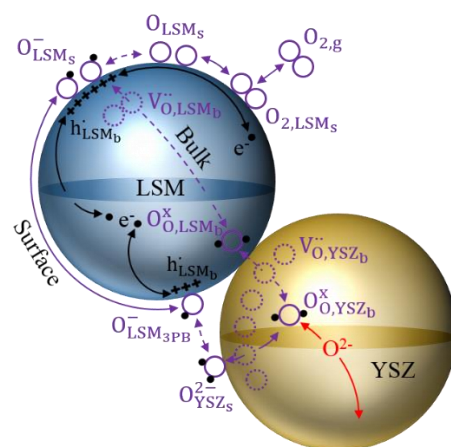
at least as far back as 1996 and 1997 by Adler et al. [113] and van Heuveln and Bouwmeester [114] among others. The mechanisms have in common one gas-phase species ($O_{2,g}$), four LSM bulk lattice species ($V_{O,LSM_b}^{\bullet\bullet}$, $V_{O,LSM_{2PB}}^{\bullet\bullet}$, O_{O,LSM_b}^{\times} and $O_{O,LSM_{2PB}}^{\times}$), two YSZ surface species ($O_{YSZ_s}^{2-}$ and \square_{YSZ_s}) and two YSZ bulk lattice species ($V_{O,YSZ_b}^{\bullet\bullet}$ and O_{O,YSZ_b}^{\times}). In addition, mechanism 1 comprises of four LSM surface species (O_{2,LSM_s} , O_{LSM_s} , $O_{LSM_{3PB}}$ and \square_{LSM_s}), mechanism 2 comprises of five LSM surface species (O_{2,LSM_s} , O_{LSM_s} , $O_{LSM_s}^-$, $O_{LSM_{3PB}}^-$ and \square_{LSM_s}) and mechanism 3 comprises of four LSM surface species (O_{2,LSM_s}^- , $O_{LSM_s}^-$, $O_{LSM_{3PB}}^-$ and \square_{LSM_s}). Here, 2PB refers to the two-phase boundary i.e. the LSM-YSZ bulk interface, 3PB is the three-phase boundary, i.e. the interface between the gas-phase and LSM and YSZ surfaces, and \square_{LSM_s} and \square_{YSZ_s} represent vacant surface sites on LSM and YSZ respectively.

The variation in number and type of LSM surface species from one mechanism to the next signifies that the difference between the mechanisms center around the steps posited to describe O_2 surface kinetics on LSM. Mechanism 1 is the simplest and is commonly adopted in the field of heterogeneous catalysis to describe oxygen incorporation in non-stoichiometric oxides [115]. It assumes that the reaction intermediate which spills over onto the YSZ surface at the 3PB and/or gets incorporated into a bulk LSM vacancy is a neutral oxygen ad-atom, O_{LSM_s} . No surface-to-bulk charge transfer steps are considered. Mechanisms 2 and 3 contradict this hypothesis and posit the formation of the ionized reaction intermediate $O_{LSM_s}^-$ because of surface-to-bulk charge transfer in LSM. The discrepancy between mechanisms 2 and 3 lies in the steps leading up to the formation of $O_{LSM_s}^-$. While mechanism 2 posits physisorption of $O_{2,g}$ on the LSM surface followed by dissociation and a surface to bulk charge transfer step to form $O_{LSM_s}^-$, mechanism 3 proposes that $O_{2,g}$ first undergoes chemisorption on the LSM surface to form the superoxo-like ad-atom O_{2,LSM_s}^- . The superoxo-like species then dissociates in conjunction with surface-to-bulk charge transfer into two $O_{LSM_s}^-$ ions. Although mechanism 2 is frequently used in the literature to describe ORR [116–119], mechanism 3 has also garnered tenability based on quantum chemical calculations [28,35,37,38].

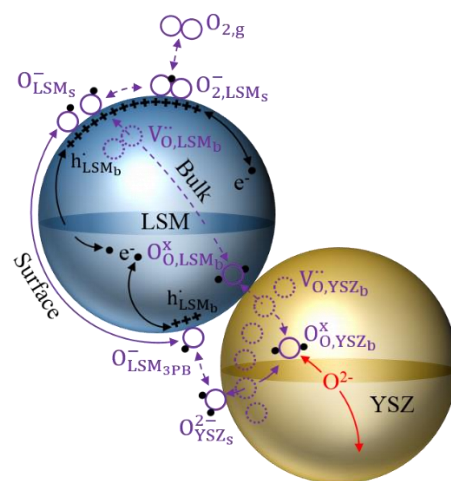
Although the surface pathway is dominant in porous LSM-YSZ composite air electrodes



Mechanism 1



Mechanism 2



Mechanism 3

↔ Surface Reaction ↔ Charge transfer Reaction

Figure 4.1. Schematic of the detailed ORR mechanisms used in the model.

[32,116,117,120], the mechanisms have been adapted to include the bulk pathway for O₂ reduction in parallel. Studies conducted by Horita et al. [121] and Brichzin et al. [122] show that for dense microelectrodes, the bulk pathway continues to be important at high cathodic polarization even when the 3PB length is high. Moreover, Adler surmises in his review of ORR on LSM air electrodes that hysteretic effects with time constants of several hours caused by polarization (as observed by McIntosh et al. [123]) can perhaps be attributed to the transition from the surface to the bulk pathway when the air electrode is maintained at high cathodic polarization for a considerable time [24]. Considering these observations, it seems prudent to include the bulk pathway and isolate its contribution, if any.

4.1.2 ORR kinetics

The faradaic current source term entering the distributed charge transfer equations, as shown in section 2.2.1 in Chapter 2, is a result of the charge-transfer reactions occurring between the LSM and YSZ phases,

$$i_F^V = -2F(A_{\text{LSM/YSZ}}^V r_{2\text{PB}} + \lambda_{3\text{PB}}^V r_{3\text{PB}}) \quad (4.1)$$

Here, $\lambda_{3\text{PB}}^V$ is the volumetric three phase boundary length, and $r_{2\text{PB}}$ and $r_{3\text{PB}}$ are the rates of the charge transfer reactions at the 2PB and 3PB respectively.

The molar production rate of species k due to both surface and CT reactions, \dot{s}_k , needs to be taken into account when conserving mass across a finite volume in the air electrode. It is evaluated here as

$$\dot{s}_k = f \sum_j \nu_{k,j} r_j \quad (4.2)$$

where j represents a reaction in which species k is involved and f is a factor that has different values for different types of reactions,

1. for a surface reaction or a surface-to-bulk charge transfer reaction, $f=1$,
2. for the charge transfer reaction at the 3PB, $f=\lambda_{3\text{PB}}^V/A_s^V$ where s denotes the surface on which the species is located, and
3. for the charge transfer reaction representing the bulk pathway, $f=1/A_s^V$.

For a given mechanism, the law of mass action gives the rate of an elementary step p ,

$$r_p = (k_{f,p} \prod_{i \in R_{f,p}} c_i^{v_i'} - k_{b,p} \prod_{i \in R_{b,p}} c_i^{v_i''}) \quad (4.3)$$

The species activity c_i is equal to volumetric concentrations for gas-phase species, surface concentrations for surface species and mole fractions for bulk lattice species. The rate coefficients of the reactions are given by modified Arrhenius expressions,

$$k_p = A \exp\left(\frac{E_a}{RT}\right) \exp\left(-\frac{n_{e,p} \beta F E_{CT}}{RT}\right) \quad (4.4)$$

where E_{CT} is the potential difference between the phases participating in a CT reaction and the charge transfer coefficient β is fixed at 0.5. For a surface reaction, E_{CT} is zero and Eq. 4.4 reduces to a purely thermally activated expression. For a CT reaction, an additional exponential dependence on E_{CT} is introduced in accordance with transition state theory (TST) [75,76,124–126]. This additional activation barrier for gaining/losing an electron is a measure of the band gap between the electron donor and electron acceptor phases relative to the Fermi level.

As evident from Fig. 4.1, for each mechanism CT reactions occur at three different regions, namely, the LSM surface exposed to the gas phase, the 2PB, and the 3PB. On the LSM surface exposed to the gas phase, a DL is formed due to the oxygen anions adsorbed on the LSM surface and the electron holes in the LSM bulk while at the 2PB a DL results from the lattice oxygen in the LSM bulk and the oxygen vacancies in the YSZ bulk. On applying TST to the CT reactions, the potential difference across each interface is expressed as a function of the potentials of each participating phase,

$$E_{\text{LSM}_{s/b}} = \phi_{\text{LSM}_b} - \phi_{\text{LSM}_s} \quad (4.5)$$

$$E_{2\text{PB}} = \phi_{\text{LSM}_b} - \phi_{\text{YSZ}_b} \quad (4.6)$$

$$E_{3\text{PB}} = \phi_{\text{LSM}_b} + \phi_{\text{LSM}_s} - 2\phi_{\text{YSZ}_s} \quad (4.7)$$

Since, ϕ_{LSM_s} is not evaluated directly, $E_{\text{LSM}_{s/b}}$ across the DL between the LSM surface and LSM bulk is evaluated using the Helmholtz model which treats the DL as a parallel plate capacitor with homogeneous charge distribution [64]. The Poisson's equation can then be solved to relate the potential across the DL, $E_{\text{LSM}_{s/b}}$, to the area specific charge and in turn, the surface coverage of anions $\theta_{\text{O}_{\text{LSM}_s}^{n-}}$,

$$E_{\text{LSM}_{s/b}} = \frac{F\Gamma_{\text{LSM}}}{C_{\text{DL}}^{\text{LSM}_{s/b}}} \sum \theta_{\text{O}_{\text{LSM}_s}^{n-}} \quad (4.8)$$

Here, $C_{\text{DL}}^{\text{LSM}_{s/b}}$ is the DL capacitance at the LSM surface-LSM bulk interface (which is equivalent to the ratio of dielectric constant to ionic radius) and $\theta_{\text{O}_{\text{LSM}_s}^{n-}}$ is the coverage of an oxygen ion species adsorbed on the LSM surface. At the 2PB, $E_{2\text{PB}}$ across the DL is calculated directly from Eq. 4.6 after ϕ_{LSM_b} and ϕ_{YSZ_b} have been evaluated using Eqs. 2.16 and 2.17 in Chapter 2. To evaluate $E_{3\text{PB}}$, it is assumed, that unlike the LSM phase, the potential difference between the YSZ surface and the bulk layer just below the YSZ surface is negligible i.e. $\phi_{\text{YSZ}_s} = \phi_{\text{YSZ}_b}$. Then combining Eqs. 4.5, 4.6 and 4.7 yields

$$E_{3\text{PB}} = 2E_{2\text{PB}} - E_{\text{LSM}_{s/B}} \quad (4.9)$$

The mechanistic details as well as the corresponding kinetic data (except the fit parameters) is given in Table 4.1 for mechanism 1, Table 4.2 for mechanism 2 and Table 4.3 for mechanism 3. Pre-exponential factors (A) and activation energies ($E_{a,f}$) are provided only for the forward reaction since the backward reaction rate constants are calculated from thermodynamic data to ensure consistency.

TABLE 4.1. ORR Mechanism 1. \square_{LSM_s} and \square_{YSZ_s} denote vacant LSM and YSZ surface sites.

	Reaction	A	$E_{a,f}$ (kJ mol ⁻¹)	Reference
R1	$\text{O}_{2,g} + \square_{\text{LSM}_s} \rightleftharpoons \text{O}_{2,\text{LSM}_s}$	1×10^{-4} ^a	0.0	[127]
R2	$\text{O}_{2,\text{LSM}_s} + \square_{\text{LSM}_s} \rightleftharpoons 2\text{O}_{\text{LSM}_s}$	Fit	Fit	-
R3	$\text{O}_{\text{LSM}_s} \rightleftharpoons \text{O}_{\text{LSM}_{3\text{PB}}}$	9.45×10^{10} s ⁻¹	144.73	[38,128]
R4	$\text{O}_{\text{LSM}_{3\text{PB}}} + \square_{\text{YSZ}_s} \rightleftharpoons \text{O}_{\text{YSZ}_s}^{2-} + \square_{\text{LSM}_s} + 2h_{\text{LSM}_b}$	Fit	Fit	-
R5	$\text{O}_{\text{YSZ}_s}^{2-} + V_{\text{O},\text{YSZ}_b} \rightleftharpoons \text{O}_{\text{O},\text{YSZ}_b}^x + \square_{\text{YSZ}_s}$	1.84×10^{13} s ⁻¹	90.9	[40]
R6	$\text{O}_{\text{LSM}_s} + V_{\text{O},\text{YSZ}_b} \rightleftharpoons \text{O}_{\text{O},\text{YSZ}_b}^x + \square_{\text{LSM}_s} + 2h_{\text{LSM}_b}$	4.87×10^7 s ⁻¹	270.29	[129]

^a sticking coefficient

TABLE 4.2. ORR Mechanism 2. \square_{LSM_s} and \square_{YSZ_s} denote vacant LSM and YSZ surface sites.

	Reaction	A	$E_{a,f}$ (kJ mol ⁻¹)	Reference
R1	$\text{O}_{2,g} + \square_{\text{LSM}_s} \rightleftharpoons \text{O}_{2,\text{LSM}_s}$	1×10^{-4} ^a	0.0	[127]
R2	$\text{O}_{2,\text{LSM}_s} + \square_{\text{LSM}_s} \rightleftharpoons 2\text{O}_{\text{LSM}_s}$	1.87×10^{21} cm ² mol ⁻¹ s ⁻¹	22.19	[37]
R3	$\text{O}_{\text{LSM}_s} \rightleftharpoons \text{O}_{\text{LSM}_s}^- + h_{\text{LSM}_b}$	Fit	Fit	-
R4	$\text{O}_{\text{LSM}_s}^- \rightleftharpoons \text{O}_{\text{LSM}_{3\text{PB}}}^-$	9.45×10^{10} s ⁻¹	144.73	[38,128]
R5	$\text{O}_{\text{LSM}_{3\text{PB}}}^- + \square_{\text{YSZ}_s} \rightleftharpoons \text{O}_{\text{YSZ}_s}^{2-} + \square_{\text{LSM}_s} + h_{\text{LSM}_b}$	Fit	Fit	-
R6	$\text{O}_{\text{YSZ}_s}^{2-} + V_{\text{O},\text{YSZ}_b} \rightleftharpoons \text{O}_{\text{O},\text{YSZ}_b}^x + \square_{\text{YSZ}_s}$	1.84×10^{13} s ⁻¹	90.9	[40]
R7	$\text{O}_{\text{LSM}_s}^- + V_{\text{O},\text{YSZ}_b} \rightleftharpoons \text{O}_{\text{O},\text{YSZ}_b}^x + \square_{\text{LSM}_s} + h_{\text{LSM}_b}$	4.87×10^7 s ⁻¹	270.29	[129]

^a sticking coefficient

TABLE 4.3. ORR Mechanism 3. \square_{LSM_s} and \square_{YSZ_s} denote vacant LSM and YSZ surface sites.

	Reaction	A	$E_{a,f}$ (kJ mol ⁻¹)	Reference
R1	$\text{O}_{2,g} + \square_{\text{LSM}_s} \rightleftharpoons \text{O}_{2,\text{LSM}_s}^- + \text{h}_{\text{LSM}_b}^+$	1×10^{-4} ^a	0.0	[127]
R2	$\text{O}_{2,\text{LSM}_s}^- + \square_{\text{LSM}_s} \rightleftharpoons 2\text{O}_{\text{LSM}_s}^- + \text{h}_{\text{LSM}_b}^+$	Fit	Fit	-
R3	$\text{O}_{\text{LSM}_s}^- \rightleftharpoons \text{O}_{\text{LSM}_{3\text{PB}}}^-$	9.45×10^{10} s ⁻¹	144.73	[38,128]
R4	$\text{O}_{\text{LSM}_{3\text{PB}}}^- + \square_{\text{YSZ}_s} \rightleftharpoons \text{O}_{\text{YSZ}_s}^{2-} + \square_{\text{LSM}_s} + \text{h}_{\text{LSM}_b}^+$	Fit	Fit	-
R5	$\text{O}_{\text{YSZ}_s}^{2-} + \text{V}_{\text{O,YSZ}_b}^{\cdot\cdot} \rightleftharpoons \text{O}_{\text{O,YSZ}_b}^{\times} + \square_{\text{YSZ}_s}$	1.84×10^{13} s ⁻¹	90.9	[40]
R6	$\text{O}_{\text{LSM}_s}^- + \text{V}_{\text{O,YSZ}_b}^{\cdot\cdot} \rightleftharpoons \text{O}_{\text{O,YSZ}_b}^{\times} + \square_{\text{LSM}_s} + \text{h}_{\text{LSM}_b}^+$	4.87×10^7 s ⁻¹	270.29	[129]

^a sticking coefficient

For mechanism 1, step R1 represents the physisorption of O₂ on LSM. The reaction is a stick reaction with no activation barrier. The pre-factor describes the probability of O₂ adsorption on the LSM surface and is evaluated using a sticking coefficient S_0 ,

$$A_{\text{R1}} = \frac{S_0}{\Gamma_{\text{LSM}}} \cdot \sqrt{\frac{RT}{2\pi W_{\text{O}_2}}} \quad (4.10)$$

S_0 is set equal to the value previously used by DeCaluwe et al. [127] based on data published by Jiang et al. [130] for O₂ adsorption on LSM. The physisorbed O₂ then dissociates to the atomic species O in step R2. The kinetic parameters of this step are obtained through fitting.

Step R3 represents the diffusion of the ad-atom O along the LSM surface to the 3PB. The rate of this step is equivalent to a surface diffusion flux gradient and the rate coefficient is proportional to D_s/δ_s^2 [35],

$$k_{\text{R3}} = k_{f,\text{R3}} = k_{b,\text{R3}} = \frac{D_s}{\delta_s^2} \cdot \theta_{\square_{\text{LSM}_s}} \quad (4.11)$$

The mean distance for surface diffusion δ_s is set to 5 nm based on prior work by Goodwin et al. [41] and la O' et al. [128] on microelectrodes and the surface diffusivity D_s is evaluated using an Arrhenius expression. The activation energy for surface diffusion is taken to be 1.5 eV in congruence with the measured range in the literature [32,128]. The pre-factor represents the jump frequency for 1-D diffusion. Considering only nearest-neighbor uncorrelated jumps,

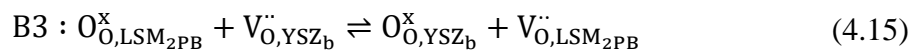
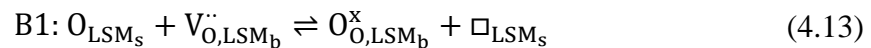
$$A_{D_s} = \frac{1}{2} \nu l^2 \quad (4.12)$$

where ν is the vibrational frequency of the ad-atom O on LSM and l is the jump distance (taken here to be the lattice constant) [38]. The rate coefficient is also weighted by the

coverage of vacant surface sites since there is no surface diffusion when all surface sites are occupied, i.e. when $\theta_{\square_{\text{LSM}_s}} = 0$.

Once the reaction intermediate O has reached the 3PB, it consumes two electrons from the LSM bulk and the O^{2-} ion so formed spills over onto the YSZ surface. The rate parameters for this step R4 are obtained through fitting. Step R5 represents the incorporation of the O^{2-} ion from the YSZ surface into the YSZ bulk. The pre-factor and activation energy for this step are related to the O_2 vacancy diffusivity in the YSZ bulk since it is assumed here that the YSZ surface is merely the boundary of the YSZ bulk lattice. The correlations used are analogous to Eqs. 4.11 and 4.12 and have been derived previously by Vogler et al. [40]. The activities of the bulk lattice species, $V_{\text{O,YSZ}_b}^{\ddot{\cdot}}$ and $\text{O}_{\text{O,YSZ}_b}^{\times}$, are fixed at their bulk mole fractions, $X_{V_{\text{O,YSZ}_b}^{\ddot{\cdot}}} = 0.0374$ and $X_{\text{O}_{\text{O,YSZ}_b}^{\times}} = 0.9626$, set by the Yttria doping level for 8 mol% Yttria in Zirconia [41].

Having traversed the traditional surface pathway for O_2 reduction on porous composite cathodes, step R6 describes the bulk pathway. In Table 4.1, the elementary steps for the bulk pathway, namely, the formation and incorporation of O^{2-} into the LSM bulk, bulk diffusion of O^{2-} through the LSM bulk, and CT at the 2PB are lumped into a single step. However, in formulating the kinetics of step R6, all three elementary steps are considered,



Although it is certainly possible to include all three steps kinetically, it would introduce additional fit parameters for steps B1 and B3 due to the absence of literature data. Moreover, measurements made on dense LSM microelectrodes, where the bulk pathway is considerably more dominant relative to the porous geometry studied here [131], have shown that step B2 is the RLS above 973K [128]. Therefore, assuming the bulk diffusion of O^{2-} through the LSM bulk to be the RLS and the other two steps to be ‘fast’ i.e. in equilibrium, the following rate expression for step R6 (which is different from the typical mass-action kinetic formulation for steps R1-R5) is obtained,

$$r_{R6} = k_{R6} \left(\frac{3}{V_{m,LSM}} \right) \left(\left(\frac{a}{1+a} - \frac{b}{1+b} \right) + \frac{2F\Delta\phi_{LSM_b}}{RT} \left(\frac{1}{1+a} \right) \right) \quad (4.16)$$

The above equation is essentially a modified Nernst-Planck equation for O₂ vacancy flux (see the Appendix for more details). The factor $\left(\frac{3}{V_{m,LSM}}\right)$ converts the bulk mole fractions of O_{0,LSM_b}^x and O_{0,LSM_{2PB}}^x into bulk molar concentrations with V_{m,LSM} representing the lattice molar volume of LSM. The terms $\left(\frac{a}{1+a} - \frac{b}{1+b}\right)$ and $\frac{2F\Delta\phi_{LSM_b}}{RT} \left(\frac{1}{1+a}\right)$ represents the O₂ vacancy flux through the LSM bulk due to diffusion and migration respectively. Here,

$$a = e^{\frac{-\Delta G_{B1}}{RT}} \cdot \frac{\theta_{O_{LSM_s}}}{\theta_{\square_{LSM_s}}} \quad (4.17)$$

$$b = e^{\frac{\Delta G_{B3}}{RT}} \cdot \frac{X_{O_{0,YSZ_b}^x}}{X_{V_{0,YSZ_b}^{\cdot}}} \cdot e^{\frac{2FE_{2PB}}{RT}} \quad (4.18)$$

where ΔG_{B1} and ΔG_{B3} are the Gibbs free energy change for steps B1 and B3 respectively. Finally, the rate coefficient k_{R6} in Eq. 4.16 is given by

$$k_{R6} = \frac{D_{V_{0,LSM_b}^{\cdot}}^e}{\delta_b} \quad (4.19)$$

Here, δ_b is the mean distance for bulk diffusion and is assumed equal to the finite volume cell thickness (see the Appendix). $D_{V_{0,LSM_b}^{\cdot}}^e$ is the effective O₂ vacancy diffusivity through the LSM bulk and is a function of the tracer self-diffusion coefficient, $D_{V_{0,LSM_b}^{\cdot}}^*$, and the electrode microstructure. It is evaluated from percolation theory in a manner similar to $\sigma_{el,LSM}^e$ and $\sigma_{io,YSZ}^e$ (see section 2.4 in Chapter 2). Since, the O₂ vacancy fraction in the bulk LSM lattice increases at high cathodic polarizations, i.e. at low p_{O_2} ,

$$D_{V_{0,LSM_b}^{\cdot}}^* = D_{V_{0,LSM_b}^{\cdot}}^{*,0} \cdot p_{O_2}^{-n} \quad (4.20)$$

Here, $D_{V_{0,LSM_b}^{\cdot}}^{*,0}$ (tracer self-diffusion coefficient at $p_{O_2} = 1$ bar) and the negative exponent n ($=0.41$) are obtained from measurements made by de Souza et al. [129,132].

Moving on to mechanism 2, the kinetics of step R1 is identical to mechanism 1. However, step R2 is assumed to be fast and the kinetic parameters of this step are taken from quantum chemical simulations performed by Choi et al. [37]. The parameter values result in a rate

coefficient similar to one published for O_2 dissociation on LSCF [42]. For the following surface-to-bulk charge transfer step R3, A_{R3} and $E_{a,f,R3}$ are fit parameters. For the subsequent steps R4-R6, the kinetics are derived as stated for steps R3-R5 of mechanism 1. For the bulk pathway, step R7, the factor a representing the rate of incorporation of the reaction intermediate O^- into the LSM bulk (given by Eq. 4.17) is augmented by an additional exponential dependence on the electric potential difference between the LSM surface and bulk, $E_{LSM_s/b}$, due to electron-hole transfer from the LSM bulk to the surface.

Finally, for mechanism 3, step R1 represents the chemisorption of gas-phase O_2 on the LSM surface, which translates kinetically to an additional exponential dependence of $k_{f,R1}$ on $E_{LSM_s/b}$ due to surface-to-bulk charge transfer. The activation energy $E_{a,f,R1}$ remains the same as for mechanisms 1 and 2. The so-formed superoxo-like ad-atom O_2^- dissociates into two O^- ad-atoms on the LSM surface by consuming another electron from the LSM bulk in step R2. The kinetic parameters of this step are obtained through fitting. The method for acquiring kinetics for the remaining steps R3-R6 are the same as for steps R4-R7 of mechanism 2.

4.1.3 ORR thermodynamics

With the forward reaction rate coefficients specified, the backward reaction rate coefficient follows from thermodynamic consistency,

$$k_b = k_f e^{\frac{\Delta G_r^0}{RT}} \quad (4.21)$$

where ΔG_r^0 is the standard Gibbs free energy change for the reaction and is evaluated using the thermodynamic properties of the species, i.e. molar enthalpies H_k and entropies S_k listed in Table 4.4. Typically, for non- equimolar reactions, e.g. step R1 for mechanisms 1, 2 and 3, the right-hand side term in Eq. 4.21 is multiplied by a reference molar concentration to obtain the correct units for k_b . However, since the thermodynamic data for O_{2,LSM_s} and O_{2,LSM_s}^- are set such that $A_{b,R1}$ and $E_{a,b,R1}$ for mechanisms 1, 2 and 3 correspond to the Arrhenius expression published by Choi for desorption of O_2 from LSM which already possesses the right units [37], this reference concentration is not necessary. The enthalpy of O_{LSM_s} and $O_{LSM_s}^-/O_{LSM_{3PB}}^-$ is a fit parameter for mechanisms 1 and 2 whereas for mechanism 3, the enthalpy of $O_{LSM_s}^-$ is evaluated from its enthalpy of formation

TABLE 4.4. Thermodynamic data (enthalpies and entropies) for gas phase, surface and bulk species used in Mechanisms 1, 2 and 3 at T=1073 K.

Species, k	H_k (kJ mol ⁻¹)			S_k (J K ⁻¹ mol ⁻¹)			Reference		
	Mech 1	Mech 2	Mech 3	Mech 1	Mech 2	Mech 3	Mech 1	Mech 2	Mech 3
<i>Gas phase</i>									
O ₂		25			246				[93]
<i>LSM phase</i>									
\square_{LSM_s}		0			0				reference species
O _{2,LSM_s}	-74.38		-	182.45		-			[37]
O _{2,LSM_s} ⁻	-		-74.38	-		182.45			[37]
O _{LSM_s}	-40		-	91.22		-			Fit
O _{LSM_s} ⁻	-	-165	-93.65	-		91.22			Fit [35]
O _{LSM_{3PB}} ⁻	-	-165	-93.65	-		91.22			Fit [35]
<i>LSM bulk</i>									
V _{O,LSM_b} ^{••}		0			0				reference species
O _{O,LSM_b} ^x		-148.24			91.22				[133]
<i>YSZ surface</i>									
\square_{YSZ_s}		0			0				reference species
O _{YSZ_s} ²⁻		-227			91.22				[40]
<i>YSZ bulk</i>									
V _{O,YSZ_b} ^{••}		0			0				reference species
O _{O,YSZ_b} ^x		-236			91.22				[40]

relative to O₂ gas [35]. The enthalpies of O_{YSZ_s}²⁻ and O_{O,YSZ_b}^x are set according to prior work in the literature [40,41,134]. To reduce the number of fit parameters, the entropies of the afore-mentioned species are set such that ΔG_r , for all steps except R1, is a function of reaction enthalpy only. Additionally, the enthalpies and entropies of the reference species (\square_{LSM_s} , \square_{YSZ_s} , V_{O,LSM_b}^{••}, V_{O,LSM_{2PB}}^{••} and V_{O,YSZ_b}^{••}) are set to zero. Lastly, the enthalpy of O_{O,LSM_b}^x is derived from equilibrium constant data [133] for the oxygen incorporation reaction into the LSM bulk in the oxygen excess region ($p_{\text{O}_2} > 10^{-5}$ atm).

4.2 Computational Procedure

To solve the coupled system of governing equations described in Chapter 2 alongside the micro-kinetic ORR mechanisms, the modeling domain is discretized into n finite volume elements of equal size Δy along the air electrode thickness such that $\Delta y \gg d_p$. The total number of elements varies from 10-30 depending on the thickness of the air electrode. In each finite volume element so formed, the spatial derivatives are resolved into algebraic expressions using the method of lines, thus converting the partial differential equations in time and space into ordinary differential equations in time only. The resulting differential algebraic system of equations are solved transiently using the semi-implicit solver LIMEX

[92]. The model computes a steady-state current density for an applied cell voltage and generates a Tafel plot by doing so for a range of applied cell voltages. To simulate electro-impedance spectra, the model uses a rapid exponential step voltage excitation method as published by Bessler [135].

4.3 Results and Discussion

4.3.1 Comparison of mechanisms against experimental data

To ensure a realistic set of kinetic and thermodynamic parameters, the mechanisms are first calibrated against experimental data measured by Barbucci et al. [43]. The baseline model parameters describing the geometry and microstructure of the cell configuration tested by Barbucci along with the electrochemical properties of the materials are listed in Table 4.5. The kinetic parameters for mechanisms 1, 2 and 3 that yield the best fits to Barbucci's measurements are listed in Table 4.6.

Figures 4.2 – 4.5 present a comparison of the simulated impedance spectra at open-circuit voltage (OCV) against Barbucci's experimental data for all three mechanisms. Figures 4.2 and 4.3 depict the Bode plots with the positive y-axis representing the real part of the complex impedance and the negative y-axis representing the imaginary part of the complex impedance. Figures 4.4 and 4.5 show the Nyquist plots. The ohmic drop across the electrolyte has been subtracted from the real part of the complex impedance in all the plots to focus solely on the electrode response. Moreover, since the experimental data refers to

TABLE 4.5. Baseline model parameters

Parameter	Value	Reference
Air electrode thickness	43 μm	[43]
Electrolyte thickness	2000 μm	[43]
Pressure	1 atm	[43]
Inlet gas velocity	10 m s^{-1}	Estimate
Porosity	0.4	Estimate
Porosity gradient	0.103 cm^{-1}	[136]
Tortuosity factor	2	Estimate
Particle diameter	0.3 μm	[43]
LSM volume fraction	0.5	[43]
YSZ volume fraction	0.5	[43]
Gas/LSM double layer capacitance	10 $\mu\text{F cm}^{-2}$	[64]
LSM/YSZ double layer capacitance	$1.067 \times 10^{-6} \cdot T - 7.438 \times 10^{-4} \text{ F cm}^{-2}$	[65]
LSM surface site density	$1.15 \times 10^{-9} \text{ mol cm}^{-2}$	Estimate
YSZ surface site density	$1.25 \times 10^{-9} \text{ mol cm}^{-2}$	[41]

TABLE 4.6. Kinetic parameters for mechanisms 1, 2 and 3 obtained by fitting to experimental data [43].

Reaction		A	$E_{a,f}$ (kJ mol ⁻¹)
<i>Mechanism 1</i>			
R2	$O_{2,LSM_s} + \square_{LSM_s} \rightleftharpoons 2O_{LSM_s}$	$5 \times 10^{22} \text{ cm}^2 \text{ mol}^{-1} \text{ s}^{-1}$	154.4
R4	$O_{LSM_{3PB}} + \square_{YSZ_s} \rightleftharpoons O_{YSZ_s}^2 + \square_{LSM_s} + 2h_{LSM_b}^i$	$7.5 \times 10^{18} \text{ cm}^3 \text{ mol}^{-1} \text{ s}^{-1}$	154.4
<i>Mechanism 2</i>			
R3	$O_{LSM_s} \rightleftharpoons O_{LSM_s}^- + h_{LSM_b}^i$	$5 \times 10^{13} \text{ cm}^2 \text{ mol}^{-1} \text{ s}^{-1}$	154.4
R5	$O_{LSM_{3PB}}^- + \square_{YSZ_s} \rightleftharpoons O_{YSZ_s}^{2-} + \square_{LSM_s} + h_{LSM_b}^i$	$4.5 \times 10^{17} \text{ cm}^3 \text{ mol}^{-1} \text{ s}^{-1}$	154.4
<i>Mechanism 3</i>			
R2	$O_{2,LSM_s}^- + \square_{LSM_s} \rightleftharpoons 2O_{LSM_s}^- + h_{LSM_b}^i$	$2.6 \times 10^{26} \text{ cm}^2 \text{ mol}^{-1} \text{ s}^{-1}$	190
R4	$O_{LSM_{3PB}}^- + \square_{YSZ_s} \rightleftharpoons O_{YSZ_s}^{2-} + \square_{LSM_s} + h_{LSM_b}^i$	$7.5 \times 10^{17} \text{ cm}^3 \text{ mol}^{-1} \text{ s}^{-1}$	144.73

the complete symmetrical cell response, the simulated impedances have been multiplied by two. On perusing the figures, it evident that all three mechanisms can match the relaxation frequency of the single impedance feature (~1-10 Hz) and estimate the impedance magnitudes over the entire range of conditions studied. The largest discrepancies are ~20% for mechanism 1 when simulating experiments at high p_{O_2} (0.5 atm and 1 atm).

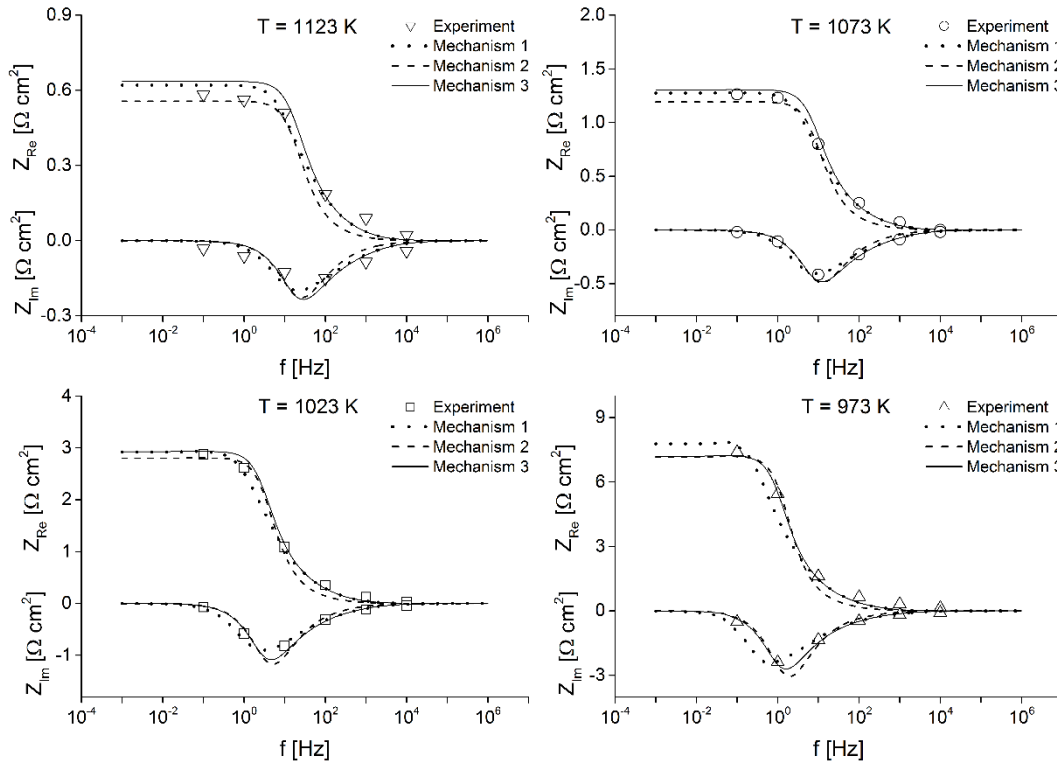


Figure 4.2. Bode plots of experimental (Barbucci et al. [43]) and simulated impedance spectra over $T = 973 \text{ K} - 1123 \text{ K}$ at OCV and $p_{O_2} = 0.21 \text{ atm}$.

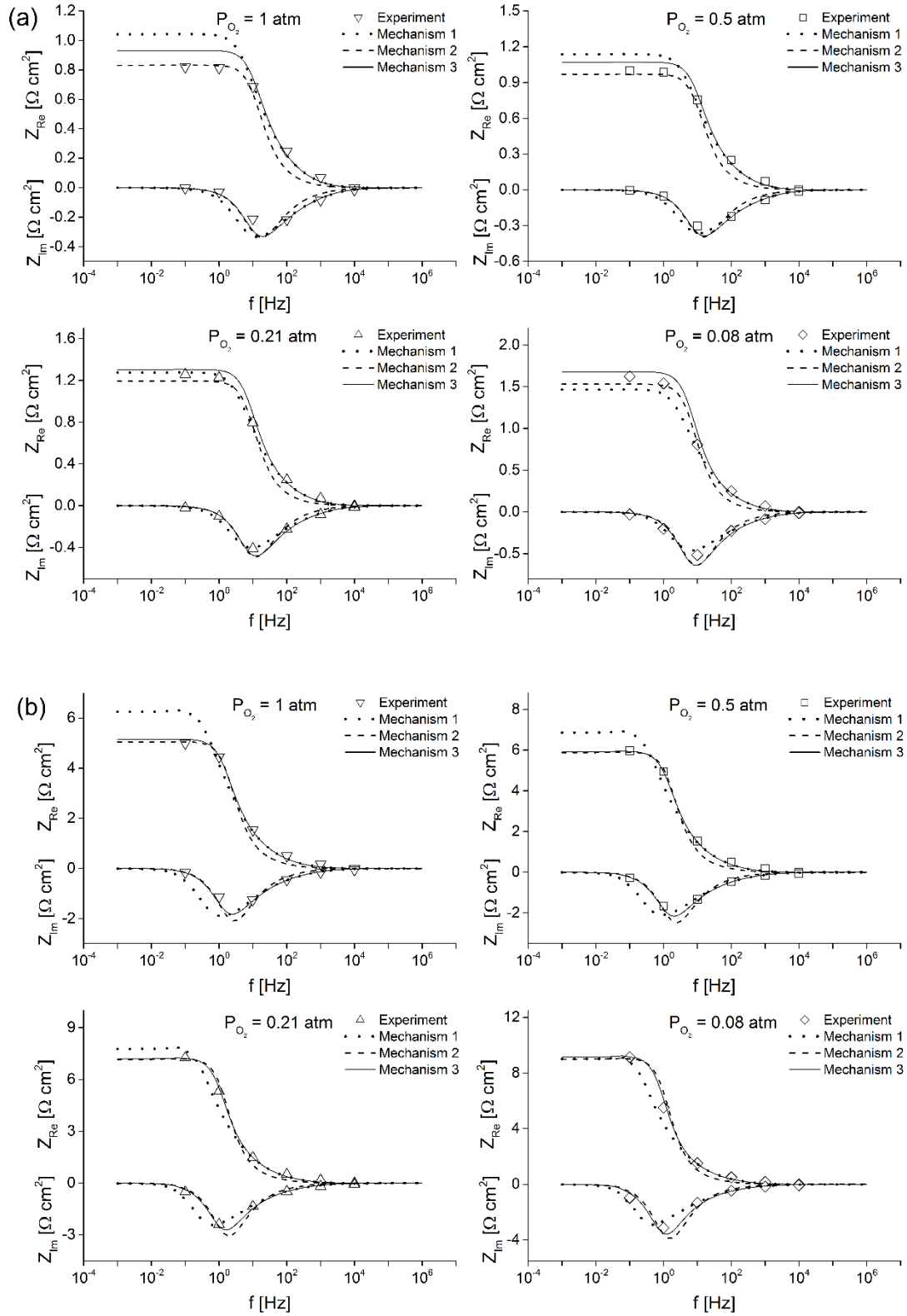


Figure 4.3. Bode plots of experimental (Barbucci et al. [43]) and simulated impedance spectra over $p_{\text{O}_2} = 0.08\text{ atm} - 1\text{ atm}$ and OCV at (a) $T = 1073\text{K}$ and (b) $T = 973\text{K}$.

However, the overall shape of the experimental spectra is best captured by mechanisms 1 and 3. The Nyquist plots show that the experimental spectra have the characteristic depressed shape as expected of these types of air electrodes. The spectra begin with a high frequency (HF) feature having a 45° slope before transitioning into a depressed semicircular feature at intermediate to low frequencies (LF). The simulated spectra for each mechanism are all variations of this depressed shape and can be attributed to the interplay between transport and kinetics. For example, the spectra corresponding to mechanism 2 have a HF slope greater than 45° and a more pronounced LF semicircle suggesting a greater contribution of kinetics to the impedance than what has been measured experimentally. On the other hand, for mechanisms 1 and 3 the relative contributions of transport and kinetics to the impedance are commensurate with the experiments.

Since the impact of polarization on LSM-YSZ composite air electrodes are well known, steady-state Tafel plots over an overpotential (η) range of -1V to +1V were also used to compare simulations with experiment. All three mechanisms can quantitatively fit the data

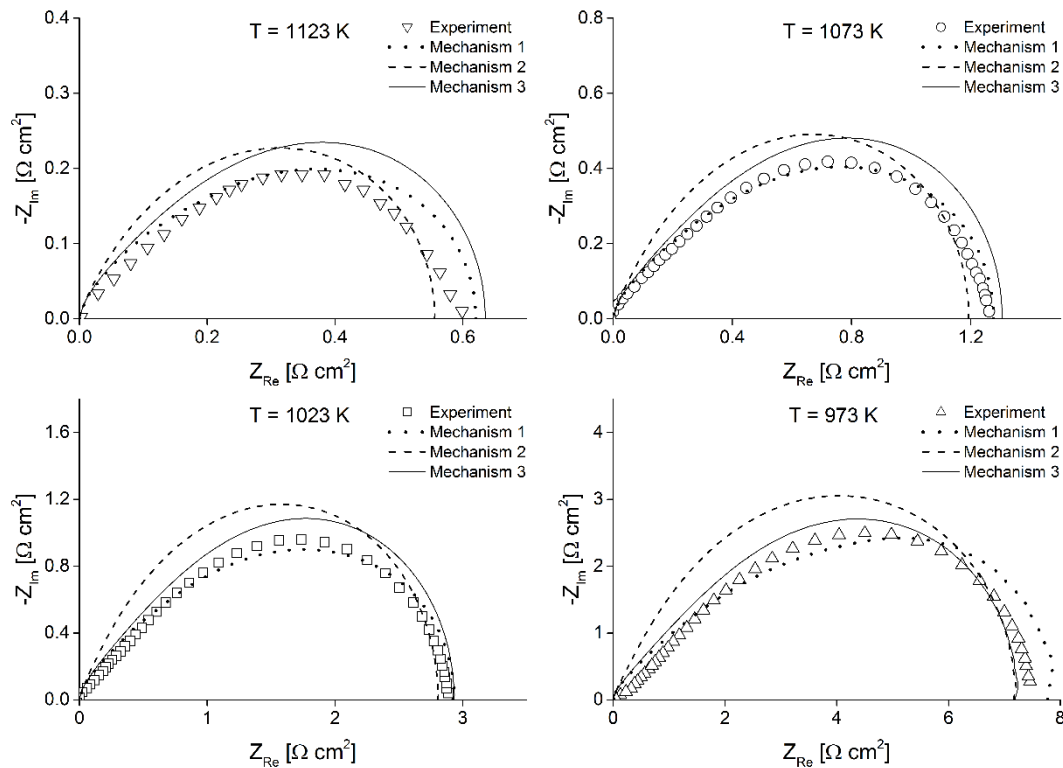


Figure 4.4. Nyquist plots of experimental (Barbucci et al. [43]) and simulated impedance spectra over $T = 973\text{ K} - 1123\text{ K}$ at OCV and $p_{O_2} = 0.21\text{ atm}$.

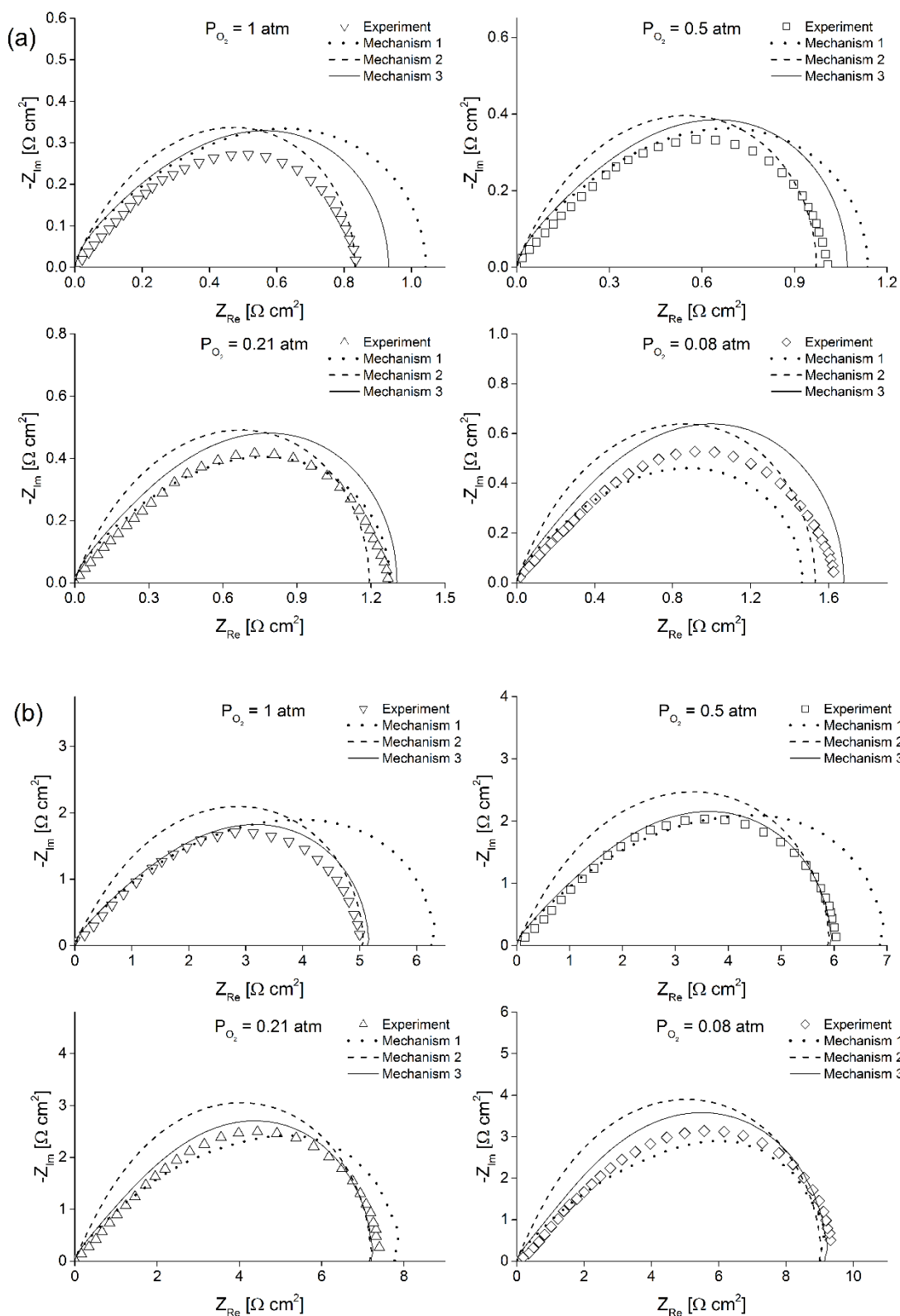


Figure 4.5. Nyquist plots of experimental (Barbucci et al. [43]) and simulated impedance spectra over $p_{O_2} = 0.08 \text{ atm} - 1 \text{ atm}$ and OCV at (a) $T = 1073\text{K}$ and (b) $T = 973\text{K}$.

and reproduce the general trend without any fictitious limiting currents at high overpotentials as illustrated in Fig. 4.6. The slight discrepancy between the experimental and simulated curves, especially at higher overpotentials, may be attributed to the 3-electrode configuration used by Barbucci for the polarization measurements as compared to the 2-electrode symmetrical cell configuration used for the EIS measurements at OCV.

Having obtained the set of best fit parameters, each mechanism is used to simulate experiments conducted by Cronin et al. [44] and Nielsen and Hjelm [45] without reparametrizing the kinetics and thermodynamics. The model parameters describing the cell configurations tested by Cronin and Nielsen are listed in Table 4.7.

A comparison of the simulated spectra against data measured by Cronin over $T=973\text{K} - 1073\text{K}$ and $p_{\text{O}_2}=0.05 \text{ atm} - 0.5 \text{ atm}$ is shown in Fig. 4.7. The experimental data has been corrected to remove a HF feature ($\sim 10 \text{ kHz}$) to ensure a more equitable comparison between simulation and experiment. The HF feature is attributed to grain boundary

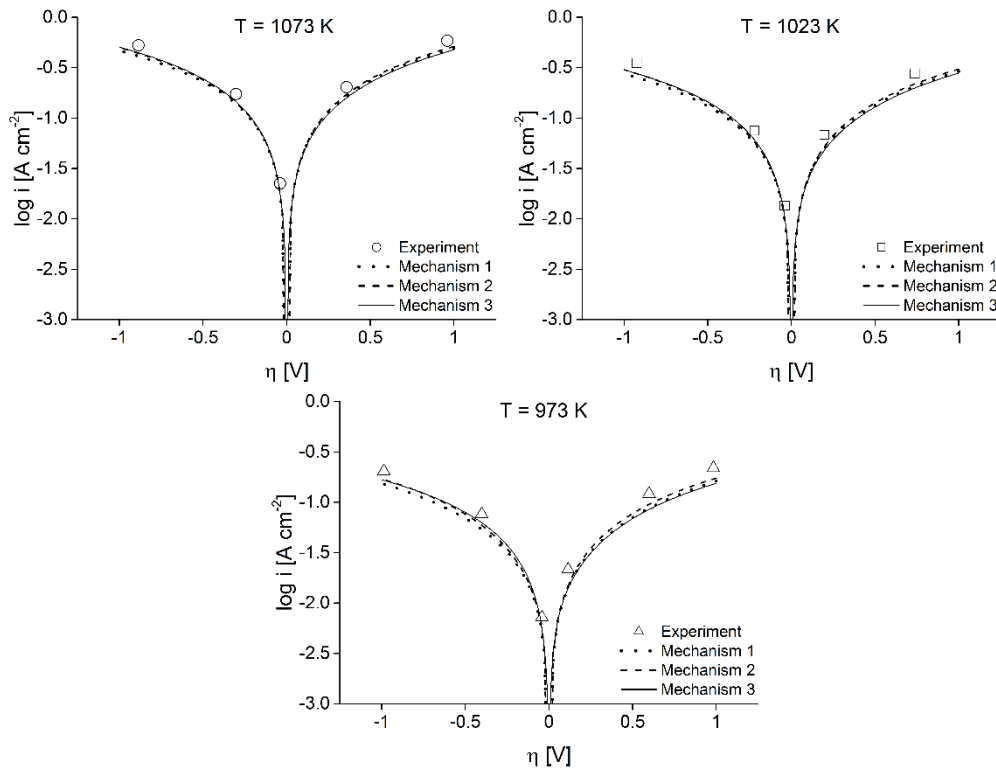


Figure 4.6. Steady-state polarization curves for experiment (Barbucci et al. [43]) and simulation over an overpotential range of -1V to $+1\text{V}$ at $p_{\text{O}_2} = 0.21 \text{ atm}$ and $T = 973\text{K} - 1073\text{K}$.

TABLE 4.7. Model parameters used to compare the mechanisms against experiments conducted by Cronin et al. [44] and Nielsen and Hjelm [45].

Parameter	Value		Reference	
	Cronin	Nielsen	Cronin	Nielsen
Air electrode Thickness	10.25 μm	20 μm	[44]	
Electrolyte Thickness	125 μm	150 μm	Estimate	[45]
Porosity	0.49	0.4	[44]	Estimate
Porosity Gradient		0		Estimate
Tortuosity	2.64	2	[44]	Estimate
Particle diameter		0.29 μm		Estimate
LSM volume fraction	0.4765	0.5	[44]	[45]
YSZ volume fraction	0.5235	0.5	[44]	[45]
Gas/LSM specific surface area				
Mechanism 1	$9.7 \times 10^4 \text{ cm}^{-1}$	$1.72 \times 10^5 \text{ cm}^{-1}$	[44]	Estimate
Mechanism 2	$9.7 \times 10^4 \text{ cm}^{-1}$	$1.15 \times 10^5 \text{ cm}^{-1}$	[44]	Estimate
Mechanism 3	$9.7 \times 10^4 \text{ cm}^{-1}$	$1.72 \times 10^5 \text{ cm}^{-1}$	[44]	Estimate
LSM/YSZ specific surface area		$1.07 \times 10^5 \text{ cm}^{-1}$		[44]
LSM/YSZ double layer capacitance				
Mechanism 1	$4.268 \times 10^{-6} \cdot T - 2.975 \times 10^{-3} \text{ F cm}^{-2}$			Estimate
Mechanism 2	$1.281 \times 10^{-5} \cdot T - 8.926 \times 10^{-3} \text{ F cm}^{-2}$			Estimate
Mechanism 3	$4.268 \times 10^{-6} \cdot T - 2.975 \times 10^{-3} \text{ F cm}^{-2}$			Estimate
Specific three phase boundary length				
Mechanism 1	$9.5 \times 10^8 \text{ cm}^{-2}$	$2.55 \times 10^9 \text{ cm}^{-2}$	[44]	Estimate
Mechanism 2		$9.5 \times 10^8 \text{ cm}^{-2}$		[44]
Mechanism 3		$9.5 \times 10^8 \text{ cm}^{-2}$		[44]

resistance in the YSZ electrolyte and/or secondary phase formation at the composite air electrode-electrolyte interface [45] and is not accounted for by the model. The plots show that while all three mechanisms can reasonably match the relaxation frequency in the Bode plot (Fig. 4.7a), mechanism 1 fails to estimate the impedances in the Nyquist plot (Fig. 4.7b). Mechanisms 2 and 3 perform reasonably well over the entire range of conditions, though mechanism 3 best captures the overall shape of the spectra.

When comparing the mechanisms against data measured by Nielsen and Hjelm in Fig. 4.8, a trend similar to that seen with the Cronin data set, is observed. While mechanisms 2 and 3 are able to adequately reproduce the measured spectra over the entire data set, mechanism 1 begins to deviate incrementally with decrease in operating temperature. These deviations become more pronounced at temperatures below 973 K where the mechanisms have not been calibrated previously.

At first glance, Figs. 4.7 and 4.8 seem to suggest that there is a different RLS for mechanism

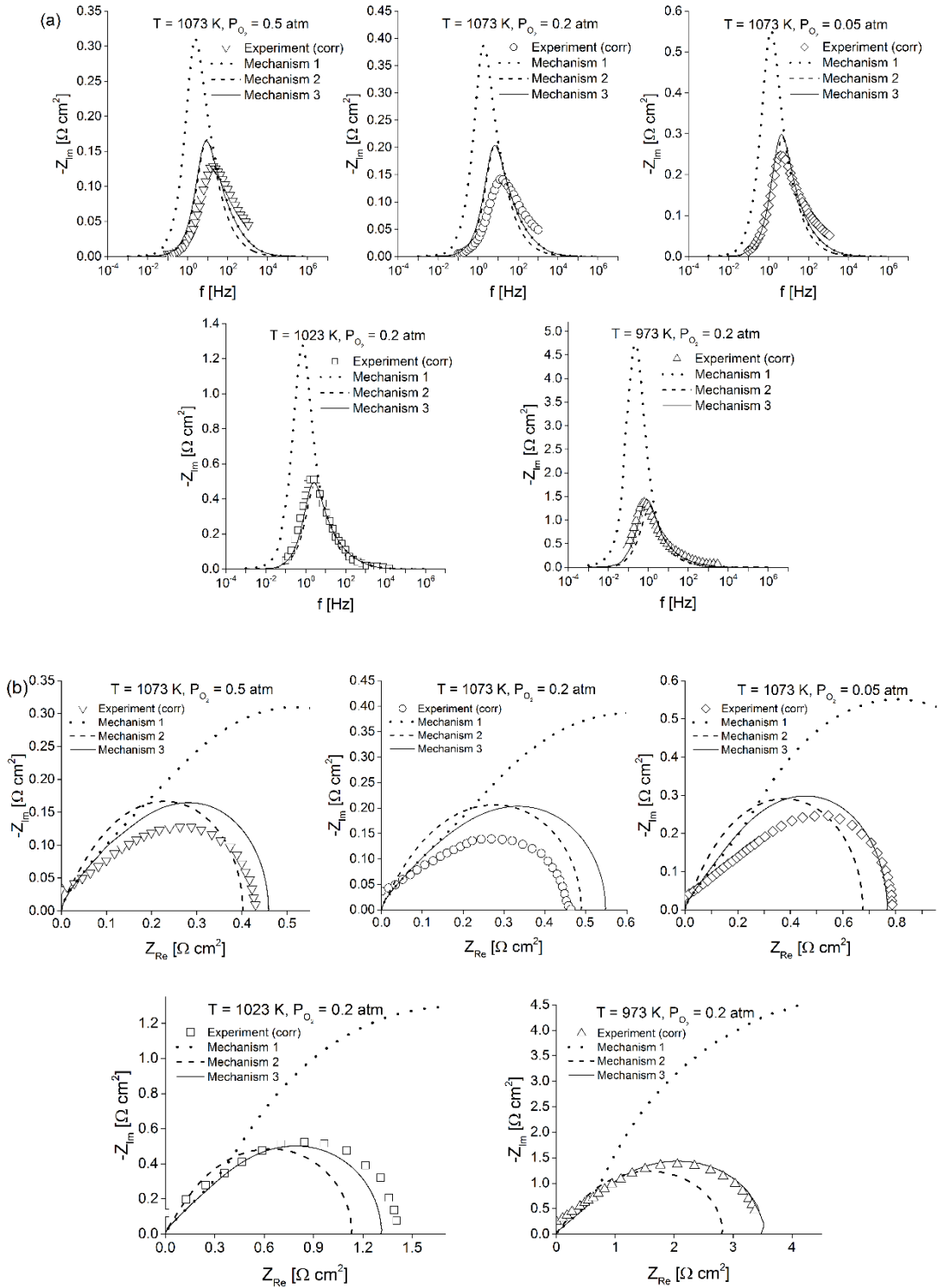


Figure 4.7. (a) Bode and (b) Nyquist plots of experimental (Cronin et al. [44]) and simulated impedance spectra over $p_{O_2} = 0.05$ atm – 0.5 atm and $T = 973\text{K} - 1073\text{K}$ at OCV. The experimental data has been corrected to remove the high frequency impedance feature due to grain boundary resistance in the YSZ phase unaccounted by the model.

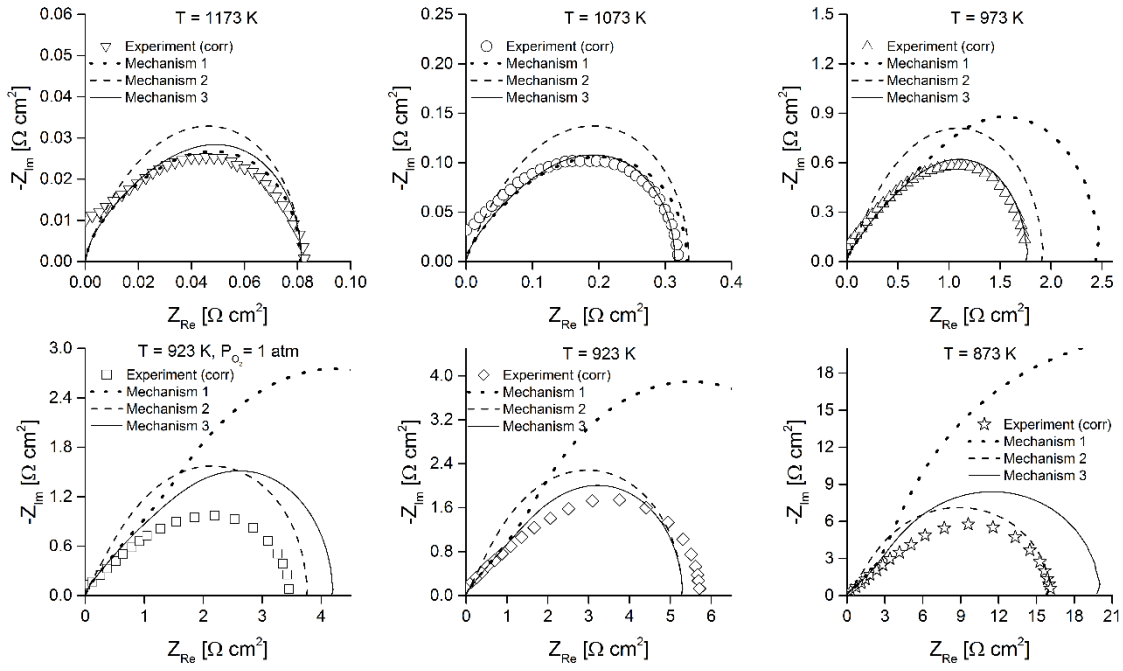


Figure 4.8. Nyquist plots of experimental (Nielsen and Hjelm [45]) and simulated impedance spectra over $T = 873\text{K} - 1173\text{K}$ at OCV. Unless mentioned otherwise, $p_{\text{O}_2} = 0.21\text{ atm}$ for all cases. The experimental data has been corrected to remove the high frequency impedance feature due to grain boundary resistance in the YSZ phase unaccounted by the model.

1 as compared to mechanisms 2 and 3. A different RLS would certainly explain why one mechanism would behave so differently than another under the same set of conditions. To investigate this further, a model-based sensitivity analysis is performed on all three mechanisms and is discussed in the following section.

4.3.2 Sensitivity Analysis

The RLSs for a given mechanism is identified by evaluating the sensitivity of the air electrode polarization resistance, R_p , to the kinetic and charge transport parameters in the model. The linear estimate of the change in R_p to a 1% change in each parameter P_i was calculated in terms of the dimensionless elasticity index,

$$EI = \frac{P_i}{R_p} \frac{\partial R_p}{\partial P_i} \quad (4.22)$$

When $EI = 1$, P_i is directly proportional to R_p , while a value of $EI = -1$ indicates P_i is indirectly proportional to R_p . When $EI = 0$, P_i is insensitive to R_p . A process is rate limiting

when the associated parameter has an $EI > 0.1$ [40]. The elasticity index is a useful metric for sensitivity since it enables direct comparison between the different parameters without having to worry about their orders of magnitude.

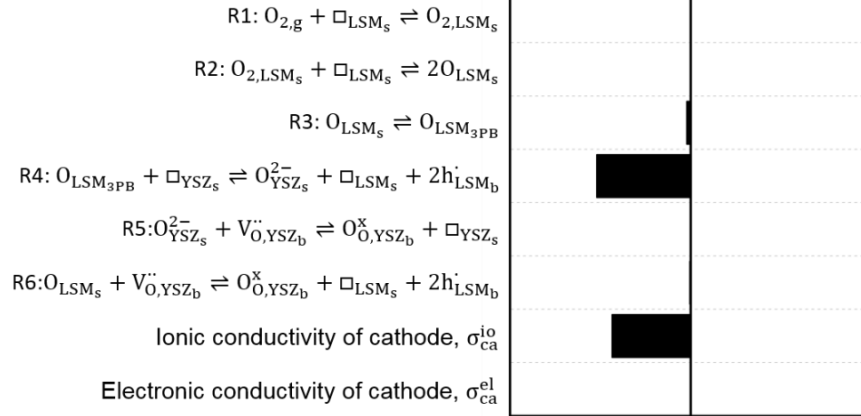
Figure 4.9 shows the sensitivities of the kinetic and charge transport processes to the polarization resistance at a given operating point for the three candidate mechanisms. The results at this point are representative of the entire range of conditions studied. The plot elucidates the difference between the three mechanisms. While ionic transport through the YSZ phase and charge transfer at the 3PB are common RLSs for all three mechanisms, mechanisms 2 and 3 have an additional RLS on the LSM surface. In fact, the surface step is the dominant RLS for mechanisms 2 and 3, while all surface steps are fast in mechanism 1.

In addition to identifying the RLSs for the three mechanisms, Fig. 4.9 also serves to highlight one of the pitfalls of the fitting approach commonly used in elementary kinetics. It is not satisfactory to simply calibrate a mechanism against one experimental data set, as even with an incorrect set of RLSs, a mechanism can adequately reproduce the data, as observed earlier in Figs. 4.2 – 4.6. Therefore, it is necessary to simulate other sets of experiments without re-fitting the kinetics and thermodynamics. Erroneous RLSs leading to deviations between mechanisms can be more clearly detected when the mechanisms are used as a predictive tool, particularly under conditions where they have not been calibrated.

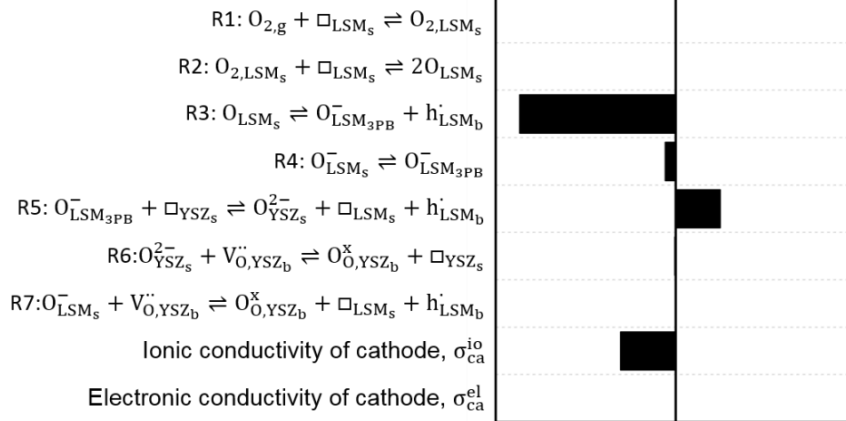
Based on the afore-mentioned results, mechanisms 2 and 3 emerge as the two best alternatives. Mechanism 3 captures the shape of the measured spectra better, particularly at higher frequencies, though owing to microstructure inhomogeneity in the actual measured electrodes and measurement uncertainty, it is a bit arbitrary to base a decision solely on this fact. From an engineering point-of-view, it may seem unnecessary to pick one mechanism over the other since both mechanisms 2 and 3 satisfy the primary objective of being ‘intrinsic’ mechanisms capable of quantitatively reproducing measured data from independent sources over a wide range of tested conditions. Adler et al. have also suggested previously that this degeneracy of mechanisms cannot be resolved without additional kinetic data distinct from the usual isotope exchange and EIS measurements at equilibrium [137]. However, while Adler’s supposition may largely hold true, for the specific case

Mechanism 1

T = 1023K, P_{O₂} = 0.21 atm, η = 0 V



Mechanism 2



Mechanism 3

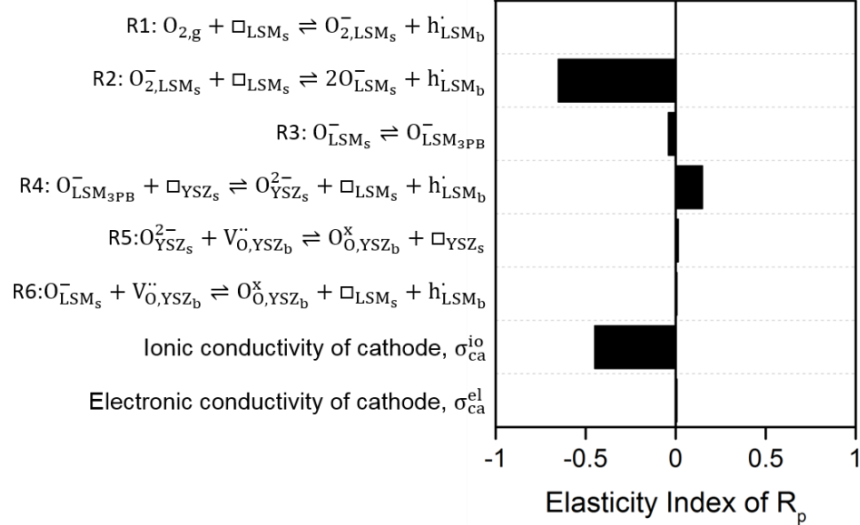


Figure 4.9. Sensitivity of the air electrode polarization resistance R_p to kinetic and charge transport parameters for the candidate mechanisms. The panels show the elasticity index of R_p at T = 1023K, $p_{O_2} = 0.21$ atm and $\eta = 0$ V.

studied here, a closer look at the set of parameters for mechanisms 2 and 3 seem to suggest that one mechanism is less plausible than the other.

The activation energies of the two fitted elementary steps (R3 and R5 for Mechanism 2 and R2 and R4 for Mechanism 3), as listed in Table 4.6, are certainly within the commonly cited range of 1.5 eV – 2.1 eV for rate limiting processes on LSM and LSM-YSZ composite air electrodes [32,128]. Yet, it must be recognized that Mechanism 2 has additional thermodynamic fit parameters, namely the species enthalpy of O_{LSM_s} and $O_{\text{LSM}_s}^-/O_{\text{LSM}_{3\text{PB}}}^-$ as listed in Table 4.4. Based on these fit values, the formation enthalpy of $2O_{\text{LSM}_s}^-$ is ~ -355 kJ/mol (-3.7 eV) relative to O_2 gas, significantly higher than the value of -2.2 eV reported in the literature [35,37]. For mechanism 3, as stated earlier in section 2.2, the species enthalpy of $O_{\text{LSM}_s}^-/O_{\text{LSM}_{3\text{PB}}}^-$ has been set to the literature value [35]. More importantly, the dissociation reaction forming atomic O_{LSM_s} in mechanism 2 is assumed to be fast with an activation energy of ~ 0.2 eV with the slow step being the surface-to-bulk charge transfer after dissociation. This assumption is in stark contrast with the accepted view in the literature of a charge transfer step preceding dissociation since the dissociation energy of O_{2,LSM_s} is over 5 eV whilst it is significantly lower for O_{2,LSM_s}^- [28,35]. Thus, though there is evidence to suggest that a surface-to-bulk charge transfer step is a rate-limiting process for transition metal oxides [64], mechanism 2 is improbable. Consequently, mechanism 3 is decidedly the most appropriate choice among the mechanisms considered in this study.

Having identified mechanism 3 to be the most tenable, the sensitivity of R_p to key electrochemical and structural model parameters was evaluated at three different temperatures, partial pressures of oxygen and overpotentials to try and shed light on the physics involved under diverse operating conditions. The model parameters used are the baseline values listed earlier in Table 4.5. The results of this more comprehensive sensitivity analysis are presented in Fig. 4.10.

Looking at the electrochemical parameters first, as stated earlier in this section, three distinct processes emerge as rate-limiting namely, the dissociation of O_{2,LSM_s}^- on the LSM surface, the charge transfer process at the 3PB and ionic transport through the YSZ phase of the air electrode. Adler in his review had highlighted that even though LSM behaved like a pure electronic conductor under these conditions, there might be a rate-limiting

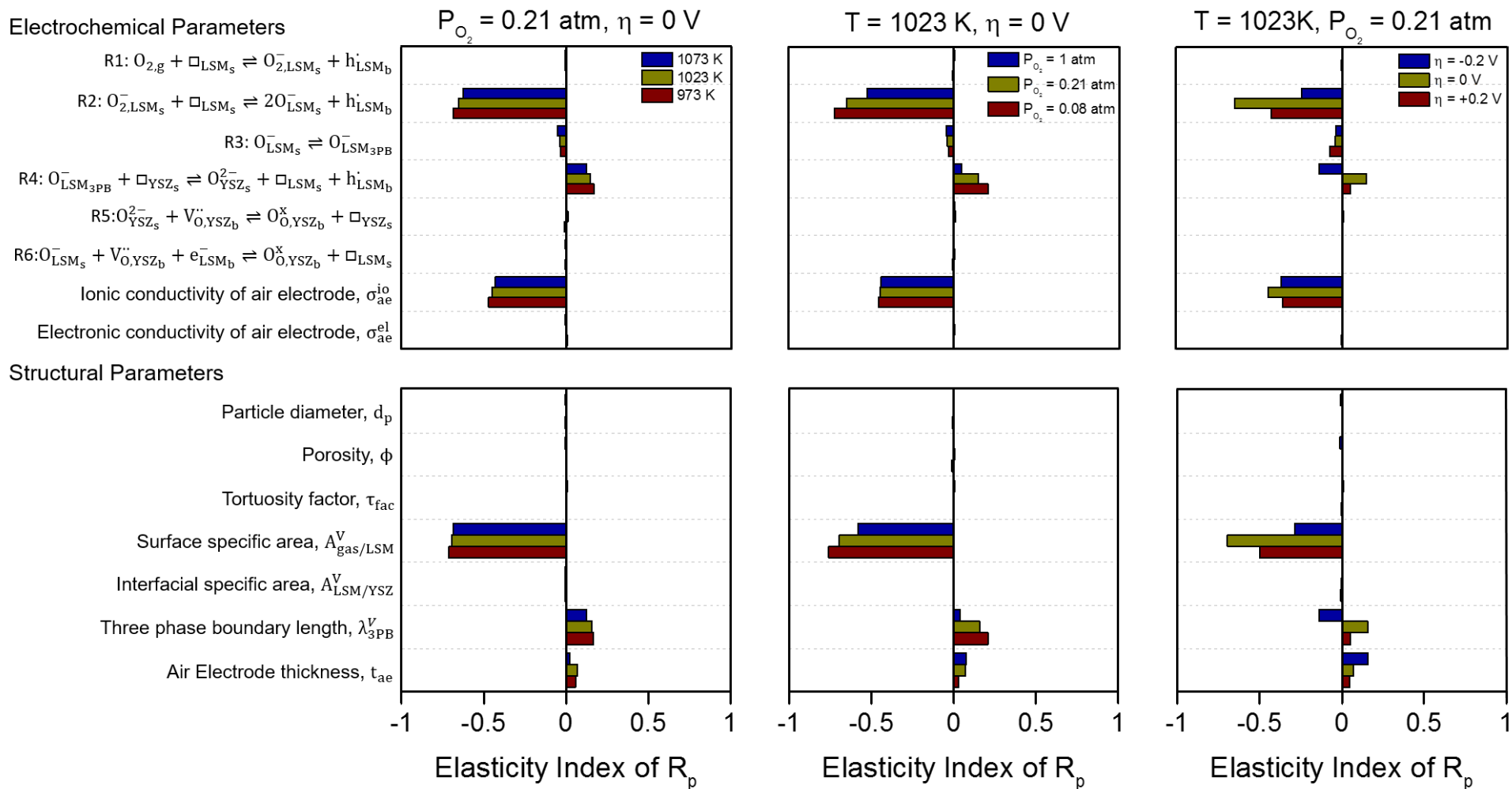


Figure 4.10. Sensitivity of the air electrode polarization resistance R_p to model parameters for mechanism 3. The left panel shows the elasticity index of R_p at $p_{O_2} = 0.21$ atm and $\eta = 0V$, the central panel at $T = 1023K$ and $\eta = 0V$ and the right panel at $T = 1023K$ and $p_{O_2} = 0.21$ atm.

surface process in addition to the charge transfer process at the TPB [24]. In fact, he attributed the depressed shape of the spectra to a coupling between surface diffusion and dissociation/adsorption which leads to the well-known ‘Gerischer’ impedance. However, as the results indicate, for the case of composite air electrodes, the depressed shape is due to a coupling between the transport of oxide ions in the ion-conducting cluster of the air electrode and electrochemical reactions (both surface and 3PB). Surface diffusion is relatively insignificant which is to be expected due to the abundance of 3PB sites in such a composite microstructure and the very short (~nm) diffusion length scales. The same conclusions were also drawn by Barbucci et al. [43] when analyzing their experimental data.

The coupling of ionic transport and kinetics for composite air electrodes has been described particularly well by Nielsen and Hjelm [45] in the language of equivalent circuits which is the most commonly used method to interpret impedance spectra in the SOC literature. They illustrate that the depressed shape purported to be a ‘Gerischer’ response can also be attained using the transmission line equivalent circuit model used first by de Levie to model porous electrodes [138]. The transmission line model is analogous to the physical electrochemical model developed in this study with the two transmission lines representing the electronic and ionic conduction networks in the air electrode connected to each other through an impedance due to electrochemical reactions. However, when one conduction network (electronic in this study) is much faster than the other, the transmission line model reduces to a Gerischer impedance.

On scrutinizing the magnitudes of the individual sensitivities to R_p , it is evident that the overall reaction is limited by the availability of O^- ions at the 3PB. The sensitivity plot shows that barring the negative overpotential case, R_p increases with increase in rate of charge transfer at the 3PB and decreases on increasing the rate of dissociation of O_2^- . The positive proportionality of R_p to r_{3PB} implies that the O^- ions at the 3PB are consumed faster than they are produced through dissociation. This situation alleviates to a certain degree under cathodic polarization when the equilibrium for both reactions are further shifted in the forward direction. The supply of O^- to the 3PB now measures up to the demand leading to a decrease in R_p with increase in 3PB charge transfer rate.

Figure 4.11 digs deeper into the shifting demand and supply of the intermediate O^- under polarization. For both cathodic and anodic polarization, the supply not only catches up to the demand but exceeds it under high polarizations. Consequently, a switchover of the dominant RLS, i.e. from the surface step R2 to the 3PB charge transfer step R4, takes place at $\eta = -0.3V$ when the air electrode is in fuel cell mode and at $\eta = 0.5V$ when the air electrode is in electrolysis mode. This is an important result to keep in mind when reducing such detailed mechanisms based on a single RLS.

The bulk pathway is insignificant under the conditions investigated in this study as evidenced by the insensitivity of R_p to the rate of step R6. Figure 4.12 is a plot of the volumetric faradaic current densities through the surface and the bulk against overpotential. As expected, at both $T=1073K$ and $973K$, the bulk pathway increases exponentially as η decreases from $-0.5V$ to $-1V$. This rise takes place because at high cathodic polarizations ($\sim -0.5V$), the Mn in the LSM bulk/surface becomes sufficiently reduced to exhibit bulk ionic conductivities similar to LSC or LSF [24]. However, as the figure elucidates, the bulk pathway is still $\sim 2-3$ orders of magnitude lower than the surface pathway, even at very high cathodic polarizations.

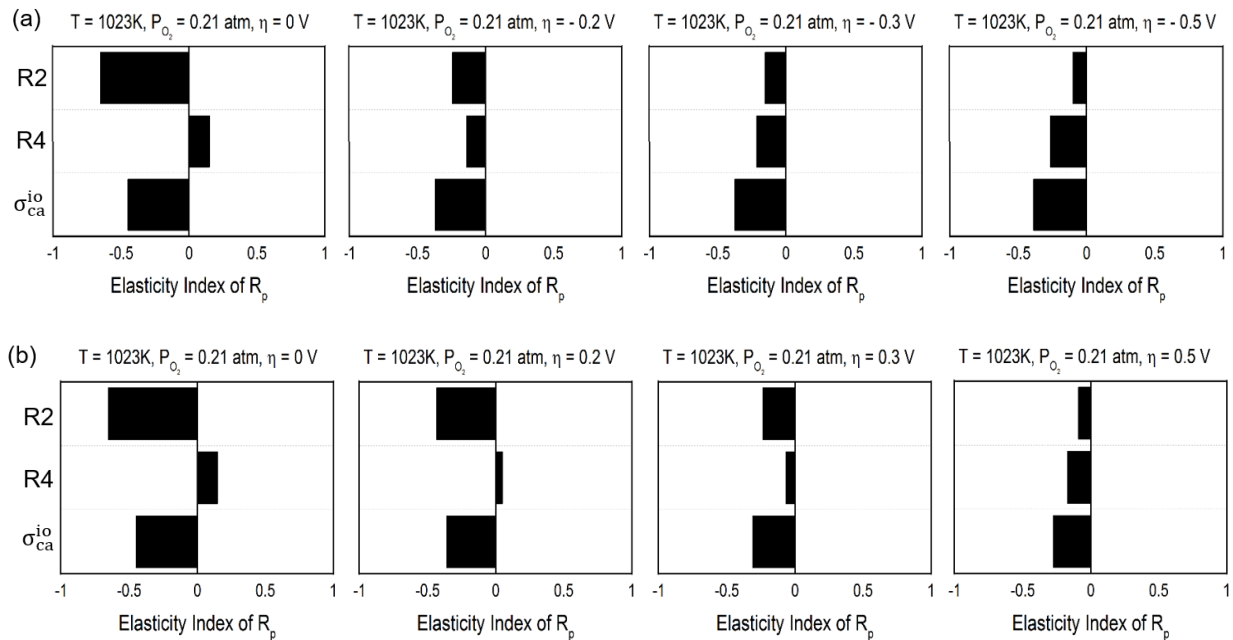


Figure 4.11. Sensitivity of the air electrode polarization resistance R_p to (a) cathodic polarization and (b) anodic polarization for mechanism 3 at $T = 1023K$ and $p_{O_2} = 0.21$ atm.

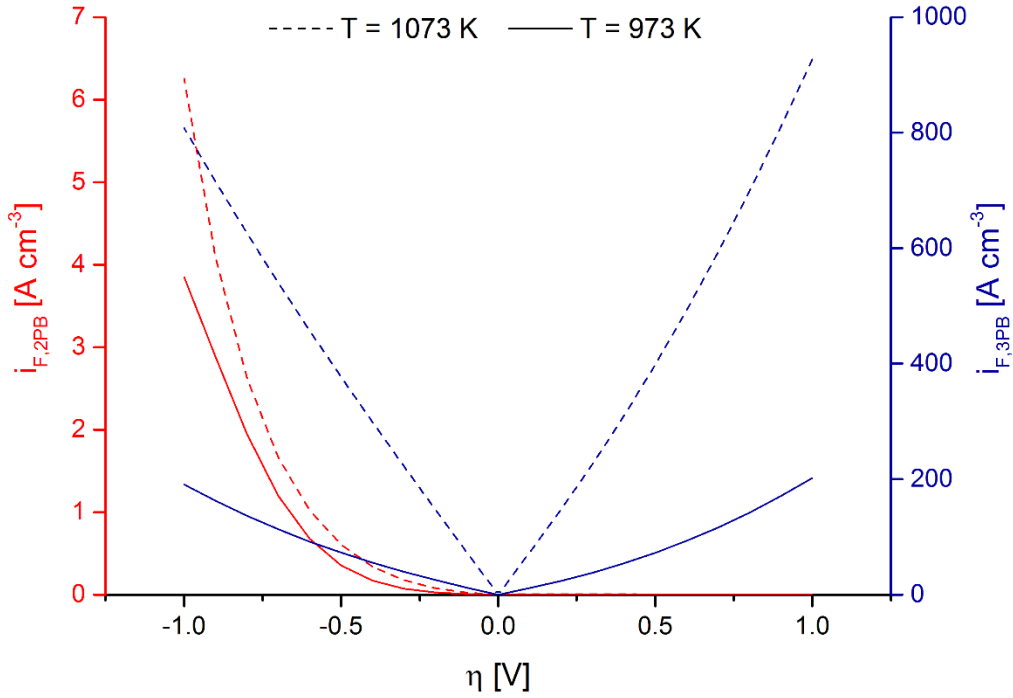


Figure 4.12. Variation of volumetric faradaic current densities at the two-phase boundary and three-phase boundary with overpotential for $T = 1073 \text{ K}$ and 973 K at $p_{O_2} = 0.21 \text{ atm}$.

Moving on to the structural parameters in Fig. 4.10, the dominance of the surface process relative to the 3PB process is reinforced by the high sensitivity of R_p to $A_{\text{gas/LSM}}^V$ juxtaposed with a comparatively lower sensitivity to $\lambda_{3\text{PB}}^V$. Though this will be flipped at high overpotentials due to the switchover of the RLS as shown previously in Fig. 4.11. Although R_p is insensitive to $A_{\text{LSM/YSZ}}^V$ since the bulk pathway is negligible, $A_{\text{LSM/YSZ}}^V$ does have an impact on the accumulation of charge at the LSM-YSZ interface which in turn, affects the relaxation frequencies in the impedance spectra. Having decoupled the dependency of d_p , ϵ and τ_{fac} to effective transport properties and specific areas and lengths for the sensitivity plot, the insensitivity of R_p to d_p , ϵ and τ_{fac} convey the absence of any gas diffusion limitations through the pores. It also signifies that the kinetic parameters so obtained are likely independent of mass transport effects even though they may still be dependent on other factors like sintering temperature, polarization history, surface reconstruction due to compositional changes, etc.

Lastly, the direct sensitivity of R_p to the air electrode thickness, t_{ae} , in Fig. 4.10 appears counter-intuitive at first but, nonetheless, was experimentally observed by Barbucci as

well. The researchers found that, in fact, R_p decreased after an optimal thickness of ~ 40 μm . The cause lies in the manufacturing process of the air electrodes. Barbucci noted that the air electrode porosity had a minor positive gradient going down from the current collector to the electrolyte interface. This gradient was quantified by Bertei et al. [136] and was included in the simulations as listed in Table 4.5. However, the sensitivity of R_p to t_{ae} ($=43$ μm) is weak since the utilization lengths of the air electrode was found to be ~ 18 μm at 1073 K and ~ 28 μm at 973 K as shown in Fig. 4.13.

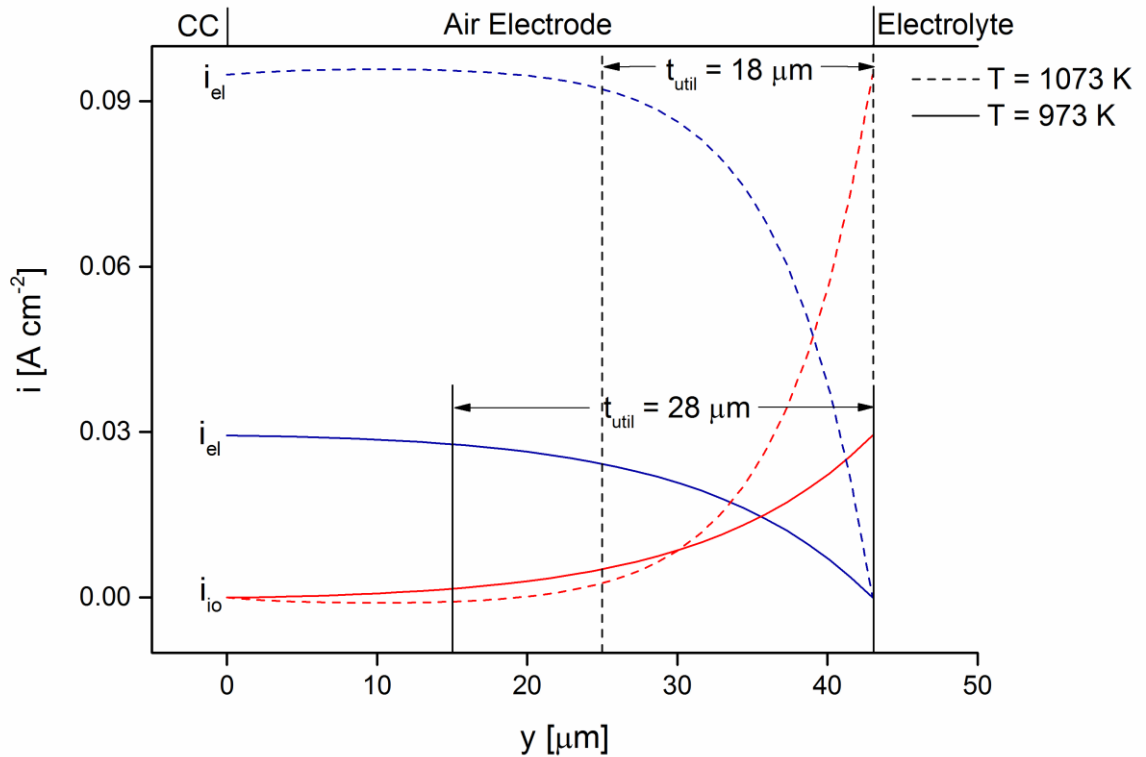


Figure 4.13. Distribution of electronic and ionic current densities along the air electrode thickness for $T = 1073$ K and 973 K at $\eta = -0.2$ V and $p_{\text{O}_2} = 0.21$ atm. CC denotes current collector.

Chapter 5

Summary and Outlook⁷

The details of a transient, multi-physics continuum model used to simulate solid oxide cells running in fuel cell and electrolysis modes have been elucidated in this present work. The model encompasses physics across multiple scales, including detailed elementary kinetic reactions on single particles at the nm scale, quasi 2-D mass, momentum, charge and energy transport in single cells at the μm -mm scales, and 3-D heat transfer in commercial stacks at the cm-m scale. Since the physics at each scale are all coupled to one another, a hierarchical approach is implemented to ensure a consistent mathematical framework. The various facets of the model are demonstrated via two example modeling studies. The examples chosen help showcase (i) the hierarchical nature of the model and (ii) the universality of the model.

To understand the effects of scaling up from lab-scale single cells to commercial cell stacks on performance, cost and reliability, the first modeling study involved the simulation of a solid oxide cell producing syngas via co-electrolysis of H_2O and CO_2 in three different configurations – a button cell, a single repeating unit (RU) and a stack of up to 40 cells. The model was first tested against polarization, cell temperature and outlet gas composition data measured by Fu et al. [46] on single Ni-GDC|YSZ|LSM-YSZ cells for different inlet reactant compositions and operating temperatures. The model agreed very well with the experiments up to current densities of $\sim 1 \text{ A cm}^{-2}$.

The model was then used to analyze the performance of a single RU of a F-design stack [47] producing $\text{H}_2:\text{CO}$ in two feed ratios necessary for Fischer-Tropsch synthesis and hydroformylation. The performance metrics, efficiency and syngas yield, were characterized using 3-D contour maps as a function of RU length, inlet gas velocity,

⁷ Parts of this section are taken with permission from [49] A. Banerjee, O. Deutschmann, Elementary kinetics of the oxygen reduction reaction on LSM-YSZ composite cathodes, *J. Catal.* 346 (2017) 30-49 and from A. Banerjee, Y. Wang, J. Diercks and O. Deutschmann, Hierarchical Modeling of Solid Oxide Cells and Stacks producing Syngas via $\text{H}_2\text{O}/\text{CO}_2$ Co-electrolysis for Industrial Applications, *Appl. Energy* 230 (2018) 996-1013.

operating voltage and operating temperature. Since the RU performance was co-limited by reactant diffusion across the thick fuel electrode and reaction kinetics over the range of operating voltages and temperatures studied, the RU efficiency and syngas yield increased with increase in residence time up to a certain value. Beyond this threshold residence time (~ 0.47 s at 1.3V and 1123.15K), reactant starvation caused mass transport limitations to become dominant resulting in a downturn in efficiency. The syngas yield corresponding to peak efficiency ($\sim 68.5\%$) was $\sim 90\%$. The high CO and H₂ contents in the fuel electrode at residence times > 0.47 s also increase the thermodynamic favorability for coking of Ni.

Although syngas yield improved considerably with both increase in voltage and temperature, the relative gain in efficiency, as expected from thermodynamics, decreased as temperature increased from 973.15K to 1123.15K. Due to the increasingly endothermic nature of H₂O and CO₂ reduction, at 1123.15K, operating at 1.2V yielded a higher peak efficiency than at 1.4V. Additionally, the 3-D performance maps were found to be virtually unchanged when changing the current density and inlet CO₂ to produce different H₂:CO ratios. The ability to operate SOECs optimally under the same conditions and flexibly produce different H₂:CO ratios without a downturn in performance is a major advantage over conventional syngas production routes.

When scaling up from a single repeating unit to a stack to meet commercial syngas production demands, shorter cells were found to be more cost and size-effective than longer cells for a target syngas production rate. Operating an 8.94 cm long 40-cell F-design stack at 1.3V and an inlet gas velocity of 0.2 m s^{-1} to attain peak efficiency led to a stack temperature variation of only $\sim 1\text{K}-4\text{K}$ below the furnace temperature of 1123.15K. However, the electrolyzer size and capital cost increased by $\sim 81\%$ compared to when the stack was run at an inlet velocity of 1.2 m s^{-1} . Nevertheless, since operational cost dominates capital cost [21], operating the electrolyzer at low current densities to maximize efficiency or yield is the most attractive option in the absence of space constraints.

Modeling a single repeating unit proved to be a computationally efficient method to evaluate stack performance. Over the range of conditions investigated, the single RU performance was representative of the performance of a 40-cell stack operating below 1.4V, while above that voltage, the repeating unit provided a slightly conservative projection of the stack performance. However, this might not be the case when modeling

SOEC stacks fed by renewable inputs like solar and wind or when modeling the highly exothermic SOFC stacks.

Finally, an investigation of the stack transients over a variety of operating conditions revealed the time constants of charge and mass transport to be insignificant compared to heat transport through the bulky thermal mass of the stack solid. The changes in product yield when switching between co-electrolysis, H₂O electrolysis and CO₂ electrolysis were congruent with previously reported measurements.

While this modeling study highlighted the diagnostic and engineering capabilities of the model, the electrochemical model formulated, like most models in the literature, can only accurately reproduce the experimental data against which it was calibrated. Due to the randomness of the electrode microstructure resulting from the sintering process, gas and charge transport effects through the microstructure are typically lumped into kinetic fit parameters. Thus, these electrochemical models are unable to reproduce measurements from multiple cells with the same configuration and operated under the same conditions without re-parametrizing the kinetic fit parameters. However, evaluating kinetic parameters that are intrinsic to the material and decoupled from microstructural effects should be able to overcome this limitation.

To that end, the second modeling study utilizes the model to compare three detailed, elementary kinetic mechanisms for the oxygen reduction/evolution reaction on LSM-YSZ composite air electrodes against measured EIS spectra and polarization curves from three distinct sources [43–45]. The comparisons are made over a wide range of temperatures, oxygen partial pressures and overpotentials. All three mechanisms provided reasonably good fits with the set of experimental data against which they were calibrated. However, mechanism 1 was unable to simulate the other two sets of experiments without reparametrizing the kinetics and thermodynamics due to an erroneous estimation of the rate limiting processes. To help decide on the most tenable mechanism between the intrinsic mechanisms 2 and 3, a more careful analysis of the kinetic and thermodynamic parameters was needed. Due to the improbable nature of a fast, neutral dissociation process and an unrealistic species enthalpy for the reaction intermediate O⁻, mechanism 2 was discarded and mechanism 3 proposing the chemisorption of O₂ to form the super-oxo like species O₂⁻ before ‘slowly’ dissociating to O⁻ was selected.

A comprehensive model-based sensitivity analysis using the selected mechanism identified the rate limiting processes under varying operating conditions for the air electrode. Ionic transport through the YSZ phase in the air electrode, dissociation of O_2^- on the LSM surface and charge transfer at the three-phase boundary were all found to be co-limiting over the entire range of operating conditions. The bulk pathway was found to be negligible relative to the surface pathway.

Although the proposed mechanism was able to qualitatively and quantitatively reproduce a large set of experimental data obtained by different experimental groups testing composite air electrodes with different microstructures and under different operating conditions, it remains unclear how close the mechanism is to being the ‘true’ mechanism for LSM-YSZ composite air electrodes. The exact nature of the reaction intermediates and elementary steps are difficult to determine experimentally. Although, based on quantum chemical studies, the proposed mechanism is the most probable mechanism with the most stable reaction intermediates and transition states.

Nonetheless, the study definitively shows that a surface process on LSM is rate limiting whether that be dissociation or surface to bulk charge transfer (or both) for these types of air electrodes. A mechanism that assumes 3PB charge transfer to be the only rate limiting step, is unable to quantitatively reproduce experimental data. Therefore, optimizing LSM specific surface area is equally as important as optimizing the 3PB length. Though, in practice, both parameters go hand-in-hand. However much more significantly, the study presents an intrinsic mechanism for ORR kinetics on LSM-YSZ composites that is capable of simulating air electrode polarization for different microstructures and operating conditions.

The results of the two modeling studies are the first steps towards the eventual target of developing a universal predictive tool for modeling SOCs. Combining a hierarchical SOC model with intrinsic electrochemical kinetics engenders a model tailored to design, monitor and control SOCs and future work can take further strides to realize such a tool. For example, developing linear state-space models from the differential form of the governing equations presented here can lead towards physics-based real-time monitoring and control models for SOCs. It would also be interesting to obtain intrinsic electrochemical kinetics for the fuel electrode, e.g. Ni-YSZ, and combine it with the LSM-YSZ kinetics developed

here and test the electrochemical model against the numerous polarization curves available in the literature for Ni-YSZ|YSZ|LSM-YSZ cells. Moreover, the elementary kinetic approach is especially conducive to developing electrode degradation mechanisms due to impurities, secondary phase formation at the electronic/ionic interfaces, surface reconfiguration due to polarization, etc. On uncovering such a reliable long-term degradation mechanism, the hierarchical stack model developed in this study can then be utilized to estimate stack lifetime and reliability by evaluating long-term stack performance over hundreds of thousands of hours thereby saving precious experimental time and cost as well as accelerating the design process. The integration of the hierarchical SOC model into a system-level model to move further up in scale is also interesting.

Appendix⁸

The purpose of this appendix is to provide further details about the derivation of the reaction rate expression used to evaluate the contribution from the bulk pathway. As stated earlier in section 2.2, the bulk pathway comprises of three reactions, viz., the incorporation of the oxygen anion into the LSM bulk lattice (B1), oxygen transport through the LSM bulk (B2) and oxygen transfer from the LSM lattice to the YSZ lattice at the bulk LSM-bulk YSZ interface (B3). Using mass-action law, the net rates of reactions B1 and B3 for mechanism 1 are

$$r_{B1} = k_{f_1} c_{O_{LSM_s}} X_{V_{O,LSM_b}^{\cdot\cdot}} - k_{b_1} X_{O_{O,LSM_b}^x} c_{\square_{LSM_s}} \quad (A.1)$$

$$r_{B3} = k_{f_3} X_{O_{O,LSM_{2PB}}^x} X_{V_{O,YSZ_b}^{\cdot\cdot}} \exp\left(-\frac{2\alpha F E_{2PB}}{RT}\right) - k_{b_3} X_{O_{O,YSZ_b}^x} X_{V_{O,LSM_{2PB}}^{\cdot\cdot}} \exp\left(\frac{2(1-\alpha) F E_{2PB}}{RT}\right) \quad (A.2)$$

The rate of reaction B2 is evaluated using the Nernst-Planck equation for oxygen vacancy transport,

$$r_{B2} = -D_{V_{O,LSM_b}^{\cdot\cdot}}^e \left(\frac{\partial c_{V_{O,LSM_b}^{\cdot\cdot}}}{\partial y} + \frac{2F}{RT} c_{V_{O,LSM_b}^{\cdot\cdot}} \frac{\partial \phi_{LSM_b}}{\partial y} \right) \quad (A.3)$$

Moreover, since the only species occupying the oxygen lattice site in LSM and YSZ are O_O^x and $V_O^{\cdot\cdot}$,

$$X_{V_O^{\cdot\cdot}} = 1 - X_{O_O^x} \quad (A.4)$$

(Note that all the symbols used in the appendix have the same meanings as in the body of the paper.)

As discussed earlier in section 2.2, reaction B2 is assumed to be the rate limiting step, i.e. reactions B1 and B3 are in equilibrium and $r_{R6} = r_{B2}$. Therefore, setting the LHS = RHS in Eqs. A.1 and A.3 and substituting Eq. A.4,

$$X_{V_{O,LSM_b}^{\cdot\cdot}} = \frac{1}{1 + a} \quad (A.5)$$

⁸ Parts of this section are taken with permission from [49] A. Banerjee, O. Deutschmann, Elementary kinetics of the oxygen reduction reaction on LSM-YSZ composite cathodes, J. Catal. 346 (2017) 30-49.

$$X_{X_{V_{\ddot{O}},LSM_2PB}} = \frac{1}{1+b} \quad (\text{A.6})$$

where

$$a = e^{\frac{-\Delta G_{B1}}{RT}} \cdot \frac{\theta_{O_{LSM_s}}}{\theta_{\square_{LSM_s}}} \quad (\text{A.7})$$

$$b = e^{\frac{\Delta G_{B3}}{RT}} \cdot \frac{X_{O_{\ddot{O},YSZ_b}}}{X_{V_{\ddot{O},YSZ_b}}} \cdot e^{\frac{2FE_{2PB}}{RT}} \quad (\text{A.8})$$

Now, re-writing Eq. A.3 in discrete form by assuming that the mean length scale for vacancy transport though the LSM bulk is equal to the discretized thickness of a finite volume element Δy and noting that the bulk vacancy mole fraction can be converted into volumetric vacancy molar concentration using the relation

$$c_{V_{\ddot{O}}} = \frac{3}{V_{m,LSM}} X_{V_{\ddot{O}}} \quad (\text{A.9})$$

Eq. A.10 yields the final form of reaction rate r_{R6} used in the model,

$$r_{R6} = r_{B2} = \frac{D_{V_{\ddot{O}},LSM_b}^e}{\Delta y} \left(\frac{3}{V_{m,LSM}} \right) \left(\left(\frac{a}{1+a} - \frac{b}{1+b} \right) + \frac{2F\Delta\phi_{LSM_b}}{RT} \left(\frac{1}{1+a} \right) \right) \quad (\text{A.10})$$

References

- [1] V.M. Janardhanan, O. Deutschmann, Modeling of Solid-Oxide Fuel Cells, *Zeitschrift Für Phys. Chemie.* 221 (2007) 443–478.
- [2] Y. Luo, Y. Shi, W. Li, N. Cai, Comprehensive modeling of tubular solid oxide electrolysis cell for co-electrolysis of steam and carbon dioxide, *Energy.* 70 (2014) 420–434.
- [3] I. Chorkendorff, J.W. Niemantsverdriet, Concepts of modern catalysis and kinetics, Wiley-VCH, Weinheim, 2005.
- [4] J. Töpler, J. Lehmann, Wasserstoff und Brennstoffzelle, Springer Berlin Heidelberg, Berlin, Heidelberg, 2014.
- [5] S. Ahmed, M. Krumpelt, Hydrogen from hydrocarbon fuels for fuel cells, *Int. J. Hydrogen Energy.* 26 (2001) 291–301.
- [6] D.K. Liguras, K. Goundani, X.E. Verykios, Production of hydrogen for fuel cells by catalytic partial oxidation of ethanol over structured Ni catalysts, *J. Power Sources.* 130 (2004) 30–37.
- [7] G. Rabenstein, V. Hacker, Hydrogen for fuel cells from ethanol by steam-reforming, partial-oxidation and combined auto-thermal reforming, *J. Power Sources.* 185 (2008) 1293–1304.
- [8] D.J. Wilhelm, D.R. Simbeck, A.D. Karp, R.L. Dickenson, Syngas production for gas-to-liquids applications: technologies, issues and outlook, *Fuel Process. Technol.* 71 (2001) 139–148.
- [9] J. Aicart, F. Usseglio-Viretta, J. Laurencin, M. Petitjean, G. Delette, L. Dessemond, Operating maps of high temperature H₂O electrolysis and H₂O+CO₂ co-electrolysis in solid oxide cells, *Int. J. Hydrogen Energy.* 41 (2016) 17233–17246.
- [10] M. Chen, J.V.T. Høgh, J.U. Nielsen, J.J. Bentzen, S.D. Ebbesen, P. V Hendriksen, High Temperature Co-Electrolysis of Steam and CO₂ in an SOC Stack, *Fuel Cells.* 13 (2013) 638–645.
- [11] M. Reytier, S. Di Iorio, A. Chatroux, M. Petitjean, J. Cren, M. Saint Jean, J. Aicart, J. Mougín, Stack performances in high temperature steam electrolysis and co-electrolysis, *Int. J. Hydrogen Energy.* 40 (2015) 11370–11377.
- [12] G. Cinti, G. Discepoli, G. Bidini, A. Lanzini, M. Santarelli, Co-electrolysis of water and CO₂ in a solid oxide electrolyzer (SOE) stack, *Int. J. Energy Res.* 40 (2016) 207–215.
- [13] N. van Nguyen, Q. Fang, U. Packbier, L. Blum, Long-term tests of a Jülich planar short stack with reversible solid oxide cells in both fuel cell and electrolysis modes, *Int. J. Hydrogen Energy.* 38 (2013) 4281–4290.
- [14] Y. Xie, X. Xue, Modeling of solid oxide electrolysis cell for syngas generation

- with detailed surface chemistry, *Solid State Ionics*. 224 (2012) 64–73.
- [15] W. Li, Y. Shi, Y. Luo, N. Cai, Elementary reaction modeling of CO₂/H₂O co-electrolysis cell considering effects of cathode thickness, *J. Power Sources*. 243 (2013) 118–130.
- [16] J. Aicart, J. Laurencin, M. Petitjean, L. Dessemond, Experimental Validation of Two-Dimensional H₂O and CO₂ Co-Electrolysis Modeling, *Fuel Cells*. 14 (2014) 430–447.
- [17] P. Kazempoor, R.J. Braun, Model validation and performance analysis of regenerative solid oxide cells, *Int. J. Hydrogen Energy*. 39 (2014) 2669–2684.
- [18] M. Ni, 2D thermal modeling of a solid oxide electrolyzer cell (SOEC) for syngas production by H₂O/CO₂ co-electrolysis, *Int. J. Hydrogen Energy*. 37 (2012) 6389–6399.
- [19] Y. Luo, Y. Shi, W. Li, N. Cai, Dynamic electro-thermal modeling of co-electrolysis of steam and carbon dioxide in a tubular solid oxide electrolysis cell, *Energy*. 89 (2015) 637–647.
- [20] V. Menon, Q. Fu, V.M. Janardhanan, O. Deutschmann, A model-based understanding of solid-oxide electrolysis cells (SOECs) for syngas production by H₂O/CO₂ co-electrolysis, *J. Power Sources*. 274 (2015) 768–781.
- [21] Q. Fu, C. Mabilat, M. Zahid, A. Brisse, L. Gautier, Syngas production via high-temperature steam/CO₂ co-electrolysis, *Energy Environ. Sci.* 3 (2010) 1382.
- [22] W.L. Becker, R.J. Braun, M. Penev, M. Melaina, Production of Fischer-Tropsch liquid fuels from high temperature solid oxide co-electrolysis units, *Energy*. 47 (2012) 99–115.
- [23] B.C.H. Steele, A. Heinzl, Materials for fuel-cell technologies, *Nature*. 414 (2001).
- [24] S.B. Adler, Factors Governing Oxygen Reduction in Solid Oxide Fuel Cell Cathodes, *Chem. Rev.* 104 (2004) 4791–4844.
- [25] H. Tu, U. Stimming, Advances, aging mechanisms and lifetime in solid-oxide fuel cells, *J. Power Sources*. 127 (2004) 284–293.
- [26] A. Indarto, J. Palguandi, *Syngas Production, Applications and Environmental Impact*, 2013.
- [27] B.A. Boukamp, H.J.M. Bouwmeester, A.J. Burggraaf, The Surface Oxygen Exchange Process in Oxygen Ion Conducting Materials, in: T.A. Ramanarayanan, W.L. Worrell, H.L. Tuller (Eds.), *Proc. Second Int. Symp. Ion. Mix. Conduct. Ceram.*, Electrochemical Society SV - v. 94-12, Pennington, NJ (10 S. Main St., Pennington 08534-2896), 1994.
- [28] R.A. Souza, A universal empirical expression for the isotope surface exchange coefficients (k*) of acceptor-doped perovskite and fluorite oxides, *Phys. Chem. Chem. Phys.* 8 (2006) 890–897.
- [29] M.J.L. Østergård, C. Clausen, C. Bagger, M. Mogensen, Manganite-zirconia composite cathodes for SOFC: Influence of structure and composition,

- Electrochim. Acta. 40 (1995) 1971–1981.
- [30] H. Fukunaga, M. Ihara, K. Sakaki, K. Yamada, The relationship between overpotential and the three phase boundary length, *Solid State Ionics*. 86 (1996) 1179–1185.
- [31] E.P. Murray, T. Tsai, S.A. Barnett, Oxygen transfer processes in (La,Sr)MnO₃/Y₂O₃-stabilized ZrO₂ cathodes: an impedance spectroscopy study, *Solid State Ionics*. 110 (1998) 235–243.
- [32] M.J. Jørgensen, M. Mogensen, Impedance of Solid Oxide Fuel Cell LSM/YSZ Composite Cathodes, *J. Electrochem. Soc.* 148 (2001) A433.
- [33] R. Merkle, J. Maier, H.J.M. Bouwmeester, A Linear Free Energy Relationship for Gas-Solid Interactions: Correlation between Surface Rate Constant and Diffusion Coefficient of Oxygen Tracer Exchange for Electron-Rich Perovskites, *Angew. Chemie Int. Ed.* 43 (2004) 5069–5073.
- [34] R. Merkle, J. Maier, How Is Oxygen Incorporated into Oxides? A Comprehensive Kinetic Study of a Simple Solid-State Reaction with SrTiO₃ as a Model Material, *Angew. Chemie Int. Ed.* 47 (2008) 3874–3894.
- [35] L. Wang, R. Merkle, Y.A. Mastrikov, E.A. Kotomin, J. Maier, Oxygen exchange kinetics on solid oxide fuel cell cathode materials—general trends and their mechanistic interpretation, *J. Mater. Res.* 27 (2012) 2000–2008.
- [36] Y. Choi, M.E. Lin, M. Liu, Computational study on the catalytic mechanism of oxygen reduction on La_{0.5}Sr_{0.5}MnO₃ in solid oxide fuel cells, *Angew. Chemie Int. Ed.* 46 (2007) 7214–7219.
- [37] Y. Choi, M.E. Lynch, M.C. Lin, M. Liu, Prediction of O₂ Dissociation Kinetics on LaMnO₃-Based Cathode Materials for Solid Oxide Fuel Cells, *J. Phys. Chem. C.* 113 (2009) 7290–7297.
- [38] H.T. Chen, P. Raghunath, M.C. Lin, Computational investigation of O₂ reduction and diffusion on 25% Sr-doped LaMnO₃ cathodes in solid oxide fuel cells, *Langmuir*. 27 (2011) 6787–6793.
- [39] S. Gewies, W.G. Bessler, V. Sonn, E. Ivers-Tiffée, Experimental and Modeling Study of the Impedance of Ni/YSZ Cermet Anodes, *10th Int. Symp. Solid Oxide Fuel Cells*. (2007) 1573–1582.
- [40] M. Vogler, A. Bieberle-Hütter, L. Gauckler, J. Warnatz, W.G. Bessler, Modelling Study of Surface Reactions, Diffusion, and Spillover at a Ni/YSZ Patterned Anode, *J. Electrochem. Soc.* 156 (2009) B663.
- [41] D.G. Goodwin, H. Zhu, A.M. Colclasure, R.J. Kee, Modeling Electrochemical Oxidation of Hydrogen on Ni–YSZ Pattern Anodes, *J. Electrochem. Soc.* 156 (2009) B1004.
- [42] V. Yurkiv, R. Costa, Z. Ilhan, A. Ansar, W.G. Bessler, Impedance of the Surface Double Layer of LSCF/CGO Composite Cathodes: An Elementary Kinetic Model, *J. Electrochem. Soc.* 161 (2014) F480–F492.

- [43] A. Barbucci, M. Paola Carpanese, M. Viviani, N. Vatistas, C. Nicolella, Morphology and electrochemical activity of SOFC composite cathodes: I. experimental analysis, *J. Appl. Electrochem.* 39 (2009) 513–521.
- [44] J.S. Cronin, K. Muangnapoh, Z. Patterson, K.J. Yakal-Kremiski, V.P. Dravid, S.A. Barnett, Effect of Firing Temperature on LSM-YSZ Composite Cathodes: A Combined Three-Dimensional Microstructure and Impedance Spectroscopy Study, *J. Electrochem. Soc.* 159 (2012) B385–B393.
- [45] J. Nielsen, J. Hjelm, Impedance of SOFC electrodes: A review and a comprehensive case study on the impedance of LSM:YSZ cathodes, *Electrochim. Acta.* 115 (2014) 31–45.
- [46] Q. Fu, J. Dailly, A. Brisse, M. Zahid, High-Temperature CO, in: *ECS Trans.*, 2011: pp. 2949–2956.
- [47] L. Blum, H.-P. Buchkremer, S. Gross, A. Gubner, L.G.J. Haart, H. Nabielek, W.J. Quadackers, U. Reisinger, M.J. Smith, R. Steinberger-Wilckens, R.W. Steinbrech, F. Tietz, I.C. Vinke, Solid Oxide Fuel Cell Development at Forschungszentrum Juelich, *Fuel Cells.* 7 (2007) 204–210.
- [48] H. Zhu, R.J. Kee, Modeling Electrochemical Impedance Spectra in SOFC Button Cells with Internal Methane Reforming, *J. Electrochem. Soc.* 153 (2006) A1765.
- [49] A. Banerjee, O. Deutschmann, Elementary kinetics of the oxygen reduction reaction on LSM-YSZ composite cathodes, *J. Catal.* 346 (2017) 30–49.
- [50] H. Zhu, R.J. Kee, V.M. Janardhanan, O. Deutschmann, D.G. Goodwin, Modeling Elementary Heterogeneous Chemistry and Electrochemistry in Solid-Oxide Fuel Cells, *J. Electrochem. Soc.* 152 (2005) A2427.
- [51] V.M. Janardhanan, O. Deutschmann, Numerical study of mass and heat transport in solid-oxide fuel cells running on humidified methane, *Chem. Eng. Sci.* 62 (2007) 5473–5486.
- [52] V. Menon, V.M. Janardhanan, S. Tischer, O. Deutschmann, A novel approach to model the transient behavior of solid-oxide fuel cell stacks, *J. Power Sources.* 214 (2012) 227–238.
- [53] S. Primdahl, M. Mogensen, Gas Conversion Impedance, *J. Electrochem. Soc.* 145 (1998) 2431.
- [54] L.L. Raja, R.J. Kee, O. Deutschmann, J. Warnatz, L. D. Schmidt, A critical evaluation of Navier–Stokes, boundary-layer, and plug-flow models of the flow and chemistry in a catalytic-combustion monolith, *Catal. Today.* 59 (2000) 47–60.
- [55] J. Bear, *Dynamics of fluids in porous media*, American Elsevier Publ, New York, 1972.
- [56] N. Epstein, On tortuosity and the tortuosity factor in flow and diffusion through porous media, *Chem. Eng. Sci.* 44 (1989) 777–779.
- [57] R.J. Kee, M. E. Coltrin and P. Glarborg, *Chemically Reacting Flow: Theory and Practice*, John Wiley, New York, 2003.

- [58] R. Suwanwarangkul, E. Croiset, M.W. Fowler, P.L. Douglas, E. Entchev, M.A. Douglas, Performance comparison of Fick's, dusty-gas and Stefan–Maxwell models to predict the concentration overpotential of a SOFC anode, *J. Power Sources*. 122 (2003) 9–18.
- [59] P.-Y. Lanfrey, Z. V Kuzeljevic, M.P. Dudukovic, Tortuosity model for fixed beds randomly packed with identical particles, *Chem. Eng. Sci.* 65 (2010) 1891–1896.
- [60] J.R. Wilson, W. Kobsiriphat, R. Mendoza, H.-Y. Chen, J.M. Hiller, D.J. Miller, K. Thornton, P.W. Voorhees, S.B. Adler, S.A. Barnett, Three-dimensional reconstruction of a solid-oxide fuel-cell anode, *Nat. Mater.* 5 (2006) 541–544.
- [61] H. Iwai, N. Shikazono, T. Matsui, H. Teshima, M. Kishimoto, R. Kishida, D. Hayashi, K. Matsuzaki, D. Kanno, M. Saito, H. Muroyama, K. Eguchi, N. Kasagi, H. Yoshida, Quantification of SOFC anode microstructure based on dual beam FIB-SEM technique, *J. Power Sources*. 195 (2010) 955–961.
- [62] J. Laurencin, R. Quey, G. Delette, H. Suhonen, P. Cloetens, P. Bleuët, Characterisation of Solid Oxide Fuel Cell Ni–8YSZ substrate by synchrotron X-ray nano-tomography, *J. Power Sources*. 198 (2012) 182–189.
- [63] H. Zhu, R.J. Kee, Modeling Distributed Charge-Transfer Processes in SOFC Membrane Electrode Assemblies, *J. Electrochem. Soc.* 155 (2008) B715.
- [64] J. Fleig, On the current-voltage characteristics of charge transfer reactions at mixed conducting electrodes on solid electrolytes, *Phys. Chem. Chem. Phys.* 7 (2005) 2027.
- [65] M.G.H.M. Hendriks, J.E. Elshof, H.J.M. Bouwmeester, H. Verweij, The electrochemical double-layer capacitance of yttria-stabilised zirconia, *Solid State Ionics*. 146 (2002) 211–217.
- [66] S.B. Adler, Reference Electrode Placement in Thin Solid Electrolytes, *J. Electrochem. Soc.* 149 (2002) E166.
- [67] W.G. Bessler, S. Gewies, M. Vogler, A new framework for physically based modeling of solid oxide fuel cells, *Electrochim. Acta*. 53 (2007) 1782–1800.
- [68] J.-W. Kim, A. V Virkar, K.-Z. Fung, K. Mehta, S.C. Singhal, Polarization Effects in Intermediate Temperature, Anode-Supported Solid Oxide Fuel Cells, *J. Electrochem. Soc.* 146 (1999) 69.
- [69] R.E. Williford, L.A. Chick, G.D. Maupin, S.P. Simner, J.W. Stevenson, Diffusion Limitations in the Porous Anodes of SOFCs, *J. Electrochem. Soc.* 150 (2003) A1067.
- [70] L.G.J. Haart, J. Mougín, O. Posdziech, J. Kiviaho, N.H. Menzler, Stack Degradation in Dependence of Operation Parameters; the Real-SOFC Sensitivity Analysis, *Fuel Cells*. 9 (2009) 794–804.
- [71] H. Zhu, R. Kee, Modeling Distributed Charge-Transfer Processes in Membrane Electrode Assemblies with Mixed-Conducting Composite Electrodes, *ECS Trans.* (2007) 1869–1878.

- [72] Z. Lin, J.W. Stevenson, M.A. Khaleel, The effect of interconnect rib size on the fuel cell concentration polarization in planar SOFCs, *J. Power Sources*. 117 (2003) 92–97.
- [73] S. Liu, C. Song, Z. Lin, The effects of the interconnect rib contact resistance on the performance of planar solid oxide fuel cell stack and the rib design optimization, *J. Power Sources*. 183 (2008) 214–225.
- [74] W. Kong, J. Li, S. Liu, Z. Lin, The influence of interconnect ribs on the performance of planar solid oxide fuel cell and formulae for optimal rib sizes, *J. Power Sources*. 204 (2012) 106–115.
- [75] R. Parsons, General equations for the kinetics of electrode processes, *Trans Faraday Soc.* 47 (1951) 1332.
- [76] T. Erdey-Gruz, *Kinetics of electrode processes*, Wiley-Interscience, New York, 1972.
- [77] P. Aguiar, C.S. Adjiman, N.P. Brandon, Anode-supported intermediate temperature direct internal reforming solid oxide fuel cell. I, *J. Power Sources*. 138 (2004) 120–136.
- [78] R.E. Hayes, S.T. Kolaczkowski, *Introduction to catalytic combustion*, Gordon & Breach, Amsterdam, 1997.
- [79] D.L. Damm, A.G. Fedorov, Spectral Radiative Heat Transfer Analysis of the Planar SOFC, *J. Fuel Cell Sci. Technol.* 2 (2005) 258.
- [80] P. Costamagna, H. Kaspar, Modeling of Solid Oxide Heat Exchanger Integrated Stacks and Simulation at High Fuel Utilization, *J. Electrochem. Soc.* 145 (1998) 3995.
- [81] J.H. Nam, D.H. Jeon, A comprehensive micro-scale model for transport and reaction in intermediate temperature solid oxide fuel cells, *Electrochim. Acta.* 51 (2006) 3446–3460.
- [82] A. Bertei, C. Nicolella, A comparative study and an extended theory of percolation for random packings of rigid spheres, *Powder Technol.* 213 (2011) 100–108.
- [83] J.G. Pharoah, K. Karan, W. Sun, On effective transport coefficients in PEM fuel cell electrodes: Anisotropy of the porous transport layers, *J. Power Sources*. 161 (2006) 214–224.
- [84] A. Bertei, C. Nicolella, Percolation theory in SOFC composite electrodes: Effects of porosity and particle size distribution on effective properties, *J. Power Sources*. 196 (2011) 9429–9436.
- [85] Y. Dong, J.S. McCartney, N. Lu, Critical Review of Thermal Conductivity Models for Unsaturated Soils, *Geotech. Geol. Eng.* 33 (2015) 207–221.
- [86] J.R. Rostrup-Nielsen, New aspects of syngas production and use, *Catal. Today*. 63 (2000) 159–164.
- [87] M. Beller, B. Cornils, C.D. Frohning, C.W. Kohlpaintner, Progress in hydroformylation and carbonylation, *J. Mol. Catal. A Chem.* 104 (1995) 17–85.

- [88] G. Narasimhaiah, V.M. Janardhanan, Modeling CO₂ electrolysis in solid oxide electrolysis cell, *J. Solid State Electrochem.* 17 (2013) 2361–2370.
- [89] S.D. Ebbesen, R. Knibbe, M. Mogensen, Co-Electrolysis of Steam and Carbon Dioxide in Solid Oxide Cells, *J. Electrochem. Soc.* 159 (2012) F482–F489.
- [90] Y. Tao, S.D. Ebbesen, M.B. Mogensen, Carbon Deposition in Solid Oxide Cells during Co-Electrolysis of H₂O and CO₂, *J. Electrochem. Soc.* 161 (2013) F337–F343.
- [91] L. Maier, B. Schädel, K. Herrera Delgado, S. Tischer, O. Deutschmann, Steam Reforming of Methane Over Nickel, *Top. Catal.* 54 (2011) 845–858.
- [92] P. Deuflhard, E. Hairer, J. Zugck, One-step and extrapolation methods for differential-algebraic systems, *Numer. Math.* 51 (1987) 501–516.
- [93] O. Deutschmann, S. Tischer, S. Kleditzsch, V.M. Janardhanan, C. Correa, D. Chatterjee, N. Mladenov, H.D. Minh, H. Karadeniz, A. Banerjee, DETCHEM™, www.detchem.com, Karlsruhe (2017).
- [94] V.M. Janardhanan, O. Deutschmann, Modeling diffusion limitation in solid-oxide fuel cells, *Electrochim. Acta.* 56 (2011) 9775–9782.
- [95] L. Jordan, W.H. Swanger, The properties of pure nickel, *Bur. Stand. J. Res.* (1930).
- [96] K.R. Reddy, K. Karan, Sinterability, Mechanical, Microstructural, and Electrical Properties of Gadolinium-Doped Ceria Electrolyte for Low-Temperature Solid Oxide Fuel Cells, *J. Electroceramics.* 15 (2005) 45–56.
- [97] M.W. Chase Jr., NIST-JANAF Thermochemical Tables, Fourth Edition, *J. Phys. Chem. Ref. Data.* (1998) 1–1951.
- [98] C. Wang, R.I. Tomov, R. Vasant Kumar, B.A. Glowacki, Inkjet printing of gadolinium-doped ceria electrolyte on NiO-YSZ substrates for solid oxide fuel cell applications, *J. Mater. Sci.* 46 (2011) 6889–6896.
- [99] C.Y. Ho, R.W. Powell, P.E. Liley, Thermal conductivity of selected materials, part 2, *Natl. Bur. Stand.* (1968).
- [100] K. Muthukkumaran, P. Kuppasami, R. Srinivasan, K. Ramachandran, E. Mohandas, S. Selladurai, Thermal properties of 15-mol% gadolinia doped ceria thin films prepared by pulsed laser ablation, *Ionics (Kiel).* 13 (2007) 47–50.
- [101] J.R. Ferguson, J.M. Fiard, R. Herbin, Three-dimensional numerical simulation for various geometries of solid oxide fuel cells, *J. Power Sources.* 58 (1996) 109–122.
- [102] K.W. Schlichting, N.P. Padture, P.G. Klemens, Thermal conductivity of dense and porous yttria-stabilized zirconia, *J. Mater. Sci.* 36 (2001) 3003–3010.
- [103] M. Radovic, E. Lara-Curzio, R.M. Trejo, H. Wang, W.D. Porter, Properties of YSZ and Ni-YSZ as a Function of Temperature and Porosity, in: N.P. Bansal, A. Wereszczak, E. Lara-Curzio (Eds.), *Adv. Solid Oxide Fuel Cells II. Ceramic Eng. Sci. Proceedings*, Vol. 27, Issue 4, John Wiley & Sons Inc, Hoboken, NJ, USA, 2006.

- [104] W. Kiatkittipong, T. Tagawa, S. Goto, S. Assabumrungrat, P. Praserttham, Oxygen transport through LSM/YSZ/LaAlO system for use of fuel cell type reactor, *Chem. Eng. J.* 106 (2005) 35–42.
- [105] I.M. Torres da Silva, M.B. Mogensen, J. Hjelm, Investigation of the degradation of LSM-YSZ SOFC cathode by electrochemical impedance spectroscopy, *Kgs. Lyngby Department Energy Convers. Storage. Technical* (2012).
- [106] K.T. Jacob, M. Attaluri, Refinement of thermodynamic data for LaMnO₃, *J. Mater. Chem.* 13 (2003) 934–942.
- [107] N. Mahato, S. Sharma, A.K. Keshri, A. Simpson, A. Agarwal, K. Balani, Nanomechanical Properties and Thermal Conductivity Estimation of Plasma-Sprayed, Solid-Oxide Fuel Cell Components, *JOM.* 65 (2013) 749–762.
- [108] P.S. 2 ThyssenKrupp VDM GmbH D-58791 Werdohl, Crofer® 22 APU, (n.d.).
- [109] C. Stoots, J. O'Brien, J. Hartvigsen, Results of recent high temperature coelectrolysis studies at the Idaho National Laboratory, *Int. J. Hydrogen Energy.* 34 (2009) 4208–4215.
- [110] M.A. Laguna-Bercero, Recent advances in high temperature electrolysis using solid oxide fuel cells: A review, *J. Power Sources.* 203 (2012) 4–16.
- [111] H.J. Grabke, Metal dusting, *Mater. Corros.* 54 (2003) 736–746.
- [112] S.D. Ebbesen, J. Høgh, K.A. Nielsen, J.U. Nielsen, M. Mogensen, Durable SOC stacks for production of hydrogen and synthesis gas by high temperature electrolysis, *Int. J. Hydrogen Energy.* 36 (2011) 7363–7373.
- [113] S.B. Adler, J.A. Lane, B.C.H. Steele, Electrode Kinetics of Porous Mixed-Conducting Oxygen Electrodes, *J. Electrochem. Soc.* 143 (1996) 3554–3564.
- [114] F.H. van Heuveln, H.J.M. Bouwmeester, Electrode Properties of Sr-Doped LaMnO₃ on Yttria-Stabilized Zirconia, *J. Electrochem. Soc.* 144 (1997).
- [115] C.K. Yang, Y. Yamazaki, A. Aydin, S.M. Haile, Thermodynamic and kinetic assessments of strontium-doped lanthanum manganite perovskites for two-step thermochemical water splitting, *J. Mater. Chem. A.* 2 (2014) 13612.
- [116] J. Kim, G. Kim, J. Moon, Y. Park, W. Lee, K. Kobayashi, M. Nagai, C. Kim, Characterization of LSM-YSZ composite electrode by ac impedance spectroscopy, *Solid State Ionics.* 143 (2001) 379–389.
- [117] X.J. Chen, S.H. Chan, K.A. Khor, Simulation of a composite cathode in solid oxide fuel cells, *Electrochim. Acta.* 49 (2004) 1851–1861.
- [118] M. Gong, R.S. Gemmen, X. Liu, Modeling of oxygen reduction mechanism for 3PB and 2PB pathways at solid oxide fuel cell cathode from multi-step charge transfer, *J. Power Sources.* 201 (2012) 204–218.
- [119] S. Pakalapati, K. Gerdes, H. Finklea, M. Gong, X. Liu, I. Celik, Micro scale dynamic modeling of LSM/YSZ composite cathodes, *Solid State Ionics.* 258 (2014) 45–60.

- [120] A. Mitterdorfer, L.J. Gauckler, $\text{La}_2\text{Zr}_2\text{O}_7$ formation and oxygen reduction kinetics of the $\text{La}_{0.85}\text{Sr}_{0.15}\text{Mn}_y\text{O}_3$, $\text{O}_2(\text{g})|\text{YSZ}$ system, *Solid State Ionics*. 111 (1998) 185–218.
- [121] T. Horita, K. Yamaji, N. Sakai, H. Yokokawa, T. Kawada, T. Kato, Oxygen reduction sites and diffusion paths at $\text{La}_{0.9}\text{Sr}_{0.1}\text{MnO}_{3-x}/\text{yttria-stabilized zirconia}$ interface for different cathodic overvoltages by secondary-ion mass spectrometry, *Solid State Ionics*. 127 (2000) 55–65.
- [122] V. Brichzin, J. Fleig, H.-U. Habermeier, G. Cristiani, J. Maier, The geometry dependence of the polarization resistance of Sr-doped LaMnO_3 microelectrodes on yttria-stabilized zirconia, *Solid State Ionics*. 152–153 (2002) 499–507.
- [123] S. McIntosh, S.B. Adler, J.M. Vohs, R.J. Gorte, Effect of Polarization on and Implications for Characterization of LSM-YSZ Composite Cathodes, *Electrochem. Solid-State Lett.* 7 (2004) A111.
- [124] P. Delahay, *Double layer and electrode kinetics*, Interscience, New York, 1965.
- [125] J.O.M. Bockris, A.K.N. Reddy, M. Gamboa-Aldeco, *Modern electrochemistry 2A: fundamentals of electrodicts*, Kluwer/Plenum, New York, 1998.
- [126] D.S. Mebane, M. Liu, Classical, phenomenological analysis of the kinetics of reactions at the gas-exposed surface of mixed ionic electronic conductors, *J. Solid State Electrochem.* 10 (2006) 575–580.
- [127] S.C. DeCaluwe, H. Zhu, R.J. Kee, G.S. Jackson, Importance of Anode Microstructure in Modeling Solid Oxide Fuel Cells, *J. Electrochem. Soc.* 155 (2008) B538.
- [128] G.J. la O', B. Yildiz, S. McEuen, Y. Shao-Horn, Probing Oxygen Reduction Reaction Kinetics of Sr-Doped LaMnO_3 Supported on Y_2O_3 -Stabilized ZrO_2 , *J. Electrochem. Soc.* 154 (2007) B427.
- [129] R.A. Souza, J.A. Kilner, Oxygen transport in $\text{La}_{1-x}\text{Sr}_x\text{Mn}_{1-y}\text{Co}_y\text{O}_{3\pm\delta}$ perovskites Part I. Oxygen tracer diffusion, *Solid State Ionics*. 106 (1998) 175–187.
- [130] Y. Jiang, S. Wang, Y. Zhang, J. Yan, W. Li, Electrochemical reduction of oxygen on a strontium doped lanthanum manganite electrode, *Solid State Ionics*. 110 (1998) 111–119.
- [131] J. Fleig, H.-R. Kim, J. Jamnik, J. Maier, Oxygen Reduction Kinetics of Lanthanum Manganite (LSM) Model Cathodes: Partial Pressure Dependence and Rate-Limiting Steps, *Fuel Cells*. 8 (2008) 330–337.
- [132] R.A. Souza, J.A. Kilner, J.F. Walker, A SIMS study of oxygen tracer diffusion and surface exchange in $\text{La}_{0.8}\text{Sr}_{0.2}\text{MnO}_{3+\delta}$, *Mater. Lett.* 43 (2000) 43–52.
- [133] J. Mizusaki, Oxygen nonstoichiometry and defect equilibrium in the perovskite-type oxides $\text{La}_{1-x}\text{Sr}_x\text{MnO}_{3+d}$, *Solid State Ionics*. 129 (2000) 163–177.
- [134] W.G. Bessler, J. Warnatz, D.G. Goodwin, The influence of equilibrium potential on the hydrogen oxidation kinetics of SOFC anodes, *Solid State Ionics*. 177 (2007) 3371–3383.

- [135] W.G. Bessler, Rapid Impedance Modeling via Potential Step and Current Relaxation Simulations, *J. Electrochem. Soc.* 154 (2007) B1186.
- [136] A. Bertei, A. Barbucci, M.P. Carpanese, M. Viviani, C. Nicolella, Morphological and electrochemical modeling of SOFC composite cathodes with distributed porosity, *Chem. Eng. J.* 207–208 (2012) 167–174.
- [137] S.B. Adler, X.Y. Chen, J.R. Wilson, Mechanisms and rate laws for oxygen exchange on mixed-conducting oxide surfaces, *J. Catal.* 245 (2007) 91–109.
- [138] R. De Levie, Electrochemical response of porous and rough electrodes, *Adv. Electrochem. Electrochem. Eng.* 6 (1967) 329–397.